FORSCHUNGSZENTRUM ROSSENDORF FZR



# Institute of Safety Research

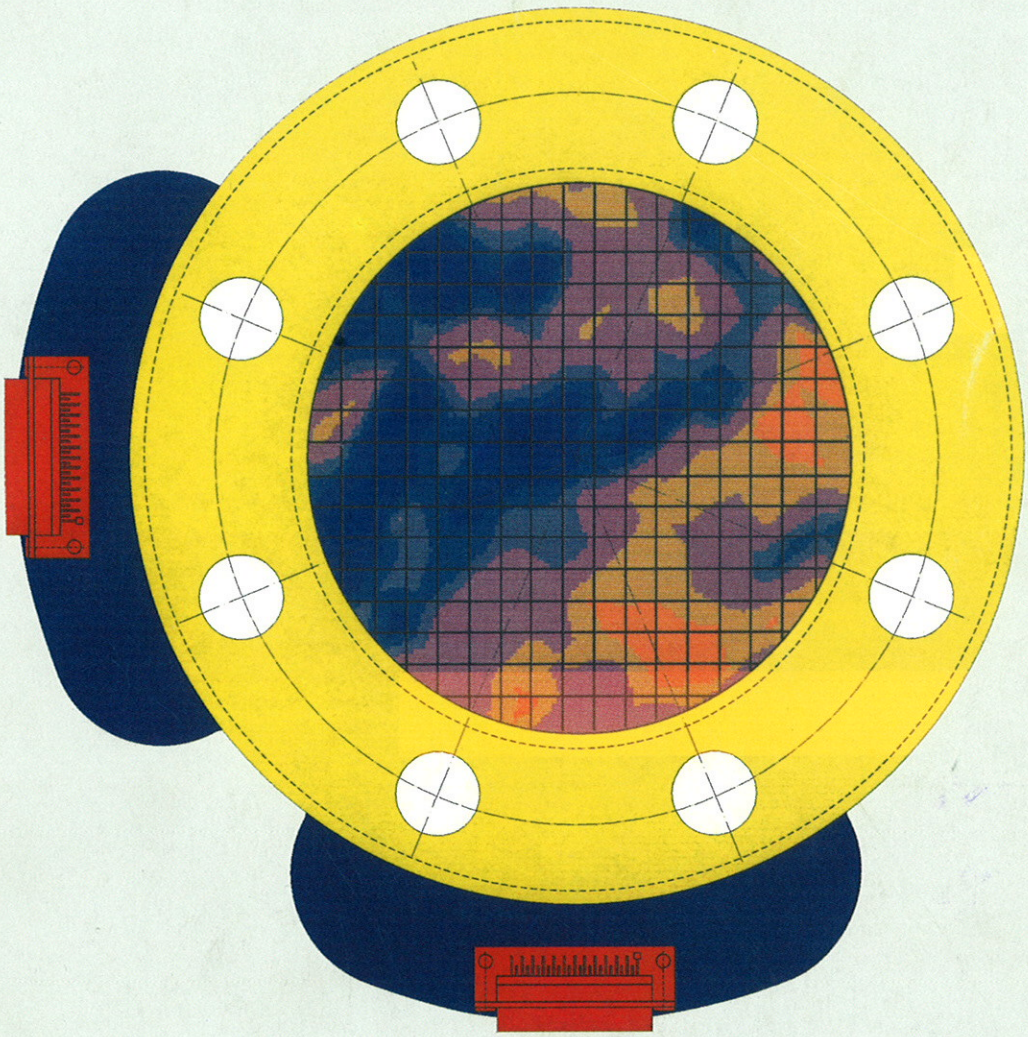

## Annual Report 1996

FZR-190
August 1997

# Annual Report 1996

## Institute of Safety Research

**Editors:** Prof. Dr. F.-P. Weiß
PD Dr. U. Rindelhardt

CONTENTS

# Preface

## Generals

The Institute of Safety Research is one of the five scientific institutes of Forschungszentrum Rossendorf e. V.. The Forschungszentrum Rossendorf is a research centre of the "Wissenschaftsgemeinschaft Blaue Liste" and as such funded by the Federal Ministry of Education and Research and by the Saxon Ministry of Science and Arts with 50 % each.

The research of the institute aims at the safety assessment of the design of nuclear and chemical facilities, the development of accident management procedures, and the increase of operational safety by improved plant surveillance.

Physical models and computer codes are developed for multiphase/multicomponent flows and for the space and time dependent power release in nuclear and chemical reactors to be able to analyse the thermo-fluiddynamic phenomena during assumed accident scenarios. Emphasis is particulary focussed on spatial flow phenomena and the time dependent change of flow patterns. Sustainable void fraction probes and tomographic systems are developed to measure those parameters of two phase flows that characterize the exchange of pulse, energy and mass between the phases and components.
The research related to materials safety is directed to the behaviour of components exposed to neutron and gamma radiation. The susceptibility to irradiation induced embrittlement and the behaviour of annealed material during reirradiation are investigated by fracture mechanical methods in dependence on the materials composition.
The microstructural mechanisms of irradiation embrittlement are studied by means of high-resolution structural analytic like neutron and X-ray small angle scattering. Highly accurate calculation methods are needed to assess the irradiation fluences and the fluence spectra that provoke the degradation of the materials properties. For that purpose, mainly Monte Carlo methods are applied.
The evaluation of the integrity of mechanical components and barriers under accident loads is one of the key issues of safety research. For that goal, structural dynamic calculations are employed which consider the mechanical and thermal interactions between the fluids and the structural components.
The work on process and plant diagnostics makes available basic methods for early failure detection and operational monitoring which are important means of accident prevention.
Recent initiatives of the institute are concerned with the transport of pollutants in the geosphere. Particularly, codes are developed for the simulation of physical and chemical processes during the transport of pollutants in unsaturated zones of the soil.

The following graphs give an overview about the sources and the deployment of funding amongst the different research tasks. In 1996 36 % of the total budget came from external sources with 28 % from research grants and 8 % from research orders.

The scientific profile of the institute has been concentrated. At the end of 1996 the investigations about the application of renewable energies were finished. Further, the department Magnetohydrodynamics was established as a consequence of the

reinforced activities in that field, which is mainly due to the participation in the Innovationskolleg "Magneto-Fluiddynamics of Electrically Conducting Liquids" of Deutsche Forschungsgemeinschaft to which the institute contributes 5 research projects. There are 17 research fellows and technicians working at that department.

The institute increased the efforts related to the safety of existing and future western light water reactors, particularly to boiling water reactors. In that context, the institute took part in the NOKO (Notkondensator) experiments of Forschungszentrum Jülich. The NOKO facility serves to test the capability of the passive emergency core cooling system for the SWR-1000 boiling water reactor of KWU/Siemens. Rossendorf contributed two-phase measuring equipment and performed fluiddynamic calculations on the convection inside the secondary side water pool.
In 1997 the Institute of Safety Research will participate in the EU concerted action on modern boiling water reactors.

## Important Results

Thermo-fluiddynamics/neutron kinetics

A one-dimensional computation model has been developed to simulate depressurization processes in chemical batch reactors during runaway. The model considers the phenomena occuring in the vessel, the venting pipe, and the safety valve. By simulation and experiment it could be shown that under unfavourable conditions strong fluctuations of the discharged mass flow can occur which lead to retarded depressurization and possibly high mechanical loads.

The neutron kinetics code DYN3D/R for western light water reactors is available in the meanwhile and can after further validation be used for safety analyses. Benchmark calculations have been performed for control rod ejection scenarios in pressurized water reactors and for subcooling transients in boiling water reactors.

Thermo-fluiddynamic single effects

Based on simple chemical model reactions it could be proven that the mass flow discharged from a chemical reactor sensitively depends even on very small amounts of tensides and surfactants added to the reaction mixture. This is due to the formation of foams in the vessel and in the venting line.

The institute provided advanced void fraction measuring equipment for the emergency condenser experiments (NOKO experiments in Jülich, dedicated to the passive decay heat removal system for future boiling water reactors) and took part in selected experiments. Moreover, the convection at the secondary side water pool was simulated using the CfD code CFX4. In agreement with the experiment it was found that a significant stratification establishes as long as the void fraction is small.

Materials safety

The construction of the radio-nuclide laboratory for the mechanical testing of irradiated reactor material could widely be finished till the end of 1996, so that the permission can be expected in the middle of 1997.

The irradiation induced microstructural changes in the material were investigated by means of neutron and X-ray small angle scattering. In some of the materials, the irradiation above all increases the number of small precipitates with a diameter between 2-4 nm, while the number density of another type of precipitates with bigger diameter almost keeps unchanged.

Applied decision analysis

A decision analytical model for the selection of the most appropriate remediation technique has been tested for decision making in case of a prototypical conventional waste deposit. The deficiencies of the decision analysis recognized during the application we removed by new methodical developments. Particularly recursive action networks were introduced which allow consideration of iterative decision procedures.

## Distribution of funding sources 1996

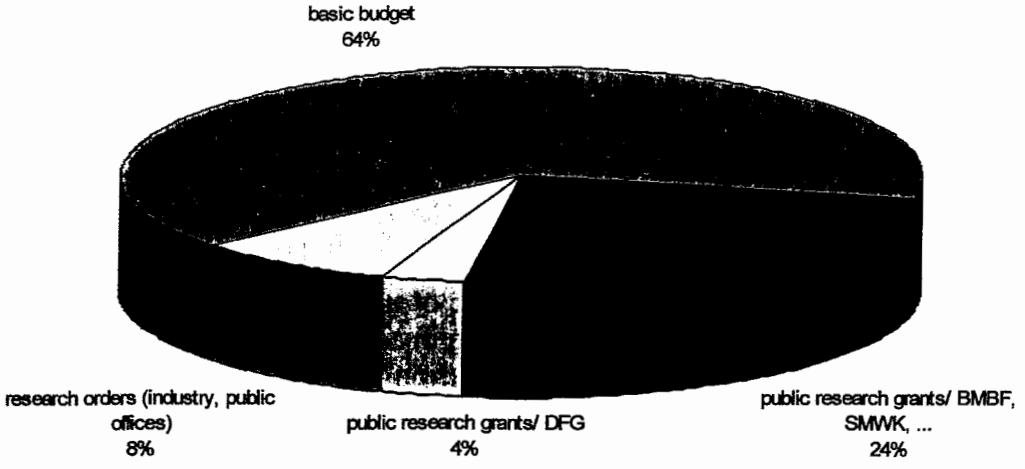


## Deployment of funding on the various tasks/projects 1996

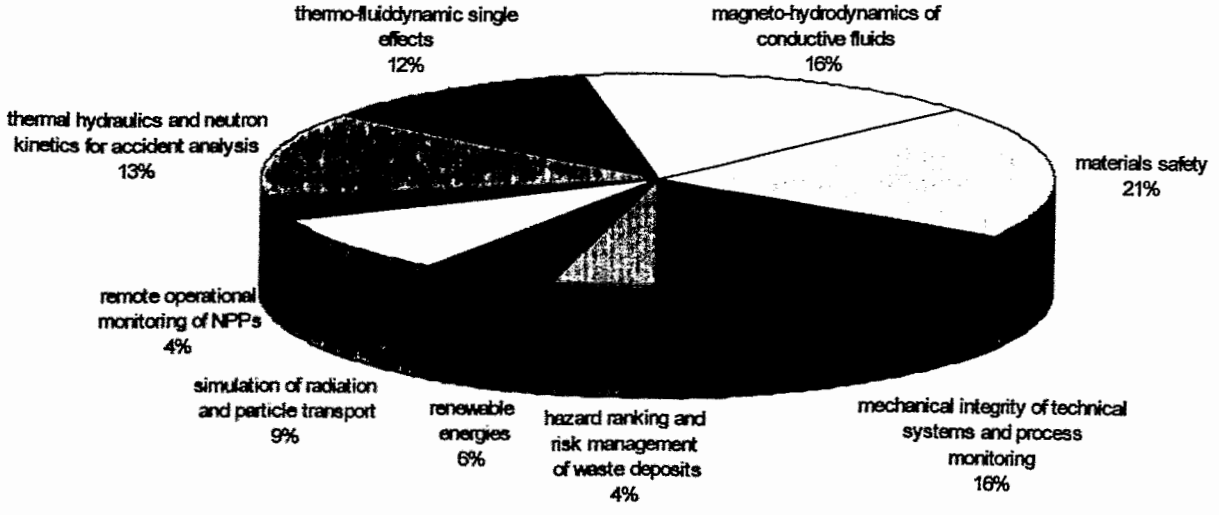

Selected Reports

# A REALISTIC MAIN STEAM LINE BREAK ANALYSIS FOR NUCLEAR POWER PLANTS WITH VVER-440 USING THE COUPLED CODE DYN3D/ATHLET

**S. Kliem**

## 1. Introduction

In the past, safety analyses were made by using thermalhydraulic system codes containing a simplified neutron kinetic model, mostly point kinetics. Increased safety requirements demand best estimate analyses. However, on the one hand, processes with remarkable 3D-effects cannot be adequately modeled by those simplified models. On the other hand, the existing 3-dimensional neutron kinetic models of the reactor core cannot satisfyingly consider the thermalhydraulic effects, caused by influences from the other components of the reactor system. The coupling of both types of codes allows to combine the advantages of these codes and to satisfy the higher safety demands. The existence of extremely powerful computers allows the routine use of such type of coupled codes.

In the Research Center Rossendorf, both the hexagonal and the Cartesian version of the 3-dimensional neutron kinetic code DYN3D were coupled with the advanced thermalhydraulic system code ATHLET. The different ways of coupling and several plausibility test calculations for the hexagonal version including comparisons with the ATHLET point kinetic model are described in [1]. After performing this coupling an advanced instrument for investigation of accident scenarios with 3-dimensional dynamic effects is available.

The shut down of the nuclear chain reaction during transients and accidents with fuel or coolant temperature increase is one of the basic safety features of nuclear reactors. The influence of fuel temperature on reactivity is described by the fuel temperature reactivity coefficient (FTC) and the influence of the coolant temperature and density by the moderator temperature reactivity coefficient (MTC).

According to the physical properties of the reactor the value of the MTC changes during the reactor fuel cycle. At the end of the fuel cycle (EOC) the MTC is most negative. This is especially due to the boron concentration in the coolant. It means, that a power increase will be stopped by coolant temperature increase very effectively. But, on the other hand, an overcooling will cause a positive reactivity insertion and this can lead to a reactor power excursion.

When the reactor is at hot stand-by conditions, the heat generation in the core is very small and the fuel is approximately at the same temperature like the coolant. In this case only a small amount of heat is deposited in the fuel and can be transferred to the coolant to mitigate the consequences of overcooling.

A break of the main steam line (MSL) of one of the six steamgenerators (SG) of a VVER-440 reactor will cause a large asymmetric overcooling of the core, because five SG will continue work at normal conditions, and only one will overcool the correspond-

ing part of the primary circuit. This asymmetric core behaviour cannot be adequately represented by point kinetics. Then a 3D-analysis is necessary.

Considering all these facts a main steam line break (MSLB) at EOC and hot zero power (HZP) conditions is the most serious overcooling transient. Therefore the safety analysis was performed for this transient.

The most important question to be answered by the analysis is: Can the reactor return to power after scram as a result of this overcooling? In other words: can the positive reactivity insertion caused by overcooling compensate the negative reactivity of the scram rods?

Several MSLB analyses are known for western type reactors from literature [e.g. 2]. In the past these analyses were based on the point kinetics included in the themalhydraulic system codes. In these calculations a required shutdown margin (mostly 1.3% reactivity) was used to assess the safety during the MSLB. Now, coupled codes enable realistic simulations of the whole transient and the use of more detailed safety criteria like local power peaks and temperatures.

In the following a detailed MSLB analysis is presented which is based on the hexagonal version of the code system DYN3D/ATHLET.

## 2. Calculation

Assumptions

The background of the calculation is as follows: The reactor is in hot stand-by subcritical conditions. According to the start up instruction all control rod groups are withdrawn one by one. After withdrawing the 3rd control rod group the reactor is critical, when it is assumed that most of the xenon in the fuel elements has already decayed. The corresponding burn-up distribution was determined by a DYN3D burn-up calculation.

When the MSLB occurs the critical reactor is characterized by:

1. The calculated boron acid concentration is 0.2g/kg.
2. The HZP conditions were assumed at 10MW.
3. The temperature and the pressure at the reactor outlet are 260.0°C and 12.05MPa, respectively.
4. The pressure in the secondary circuit is 4.67MPa, the temperature corresponds to the saturation temperature. No steam is produced.
5. The first three control rod groups are in fully withdrawn position. The others are completely inserted.
6. All main coolant pumps (MCP) are in operation.

The MSLB is postulated as a double ended break (DEB) of the MSL downstream the SG in front of the steam isolation valve (SIV). This break will cause an asymmetric cooling of the core, because the affected SG cannot be isolated from the leak. The diameter of the MSL is 0.425m.

Scenario

t=0s Sudden and complete DEB of one MSL.
The pressure decreases rapidly in all SG, because they are connected through the main steam collector (MSCOL).

t=1.3s The velocity of pressure decrease in the MSCOL reaches the critical value of 0.05MPa/s.

t=6.3s With a delay time of 5s the SIV in all MSL begin to close. The closing of the SIV causes the shutdown of the MCP in the corresponding loop. In the considered case, all MCP are switched off. The closing of more then 3 SIV triggers the reactor scram. All withdrawn control rod groups are immediately inserted into the core, expect the most effective control rod, which is assumed to be the stuck rod. It keeps fully withdrawn.

During the transient the primary pressure reaches the actuation point of the High Pressure Injection System, but for the calculation it is supposed to fail.

Accident progression

In the secondary circuit the MSCOL and the intact SG are isolated from the leak by closing all SIV. So the pressure decrease can be stopped at the SG secondary side, the one SG expected at which the leak occurred. In this SG the water level rapidly decreases after leak opening (1m in 30s). The feedwater mass flow rate is going up to its maximum, because it is controlled by the water level. Later the water level is stabilized at 50cm below the starting value. The heat flux to the secondary side of the failed SG reaches the maximum at t=35s. Then the heat flux slowly decreases until the end of the investigated time. The temperature decreases together with the pressure along the saturation curve.

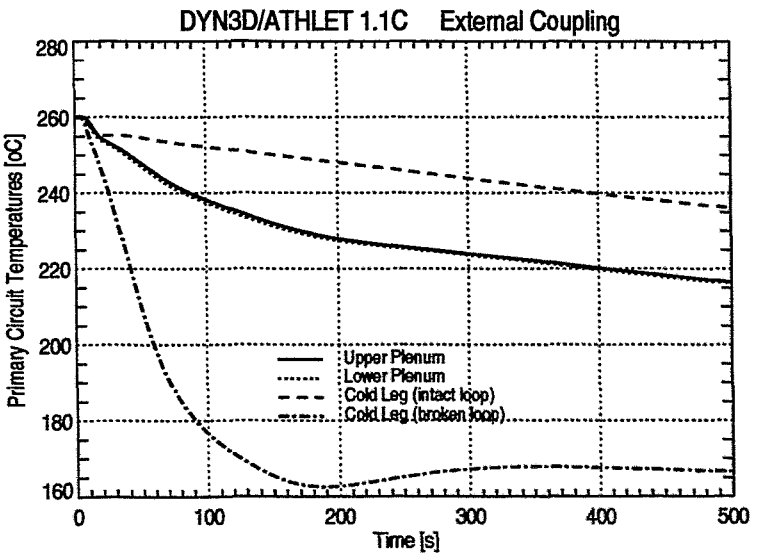


Fig. 1: Primary circuit temperatures in the case of ideal coolant mixing in the lower plenum

The temperature reaches a minimum (161°C) at t=130s. Later on, the temperature increases again up to 168°C according to the pressure rise. Pressure and temperature decrease in the failed SG lead to an increasing heat flux from the primary to secondary side. In the corresponding loop the coolant temperature falls by 65K over the first 60 seconds after break and further by 30K in the following 100 seconds (Fig. 1). Then the temperature slightly increases caused by the rise of temperature of the

secondary side. After scram, the power generation in the core is stopped and the coolant temperature in the core and in the intact loops also decreases. At t=30s the coolant temperature in the intact loops drops below the temperature of the secondary side. For this reason the heat flux direction is inverted, from secondary to primary side. This backward heat flux partially compensates the overcooling effect from the broken loop and the core inlet temperature drops at a slower rate, from 260°C to 216°C at the end of the investigated time interval (500s after break). This temperature drop leads to a positive reactivity insertion. Within 500s this reactivity effect does not completely compensate the scram reactivity. At the end of the investigated time the reactor is still subcritical. After MCP coastdown, natural convection establishes in the primary circuit. Due to the different temperature in the loops the mass flow rates are also different. After 500s the mass flow rate in the broken loop is about 200kg/s. This is about twice the value of one intact loop (93kg/s). The mass flow rate through the core is about 700 kg/s (8% of the starting level).

## 3. Variation of mixing conditions in the lower plenum

The calculation presented above was made with the assumption of homogenous coolant mixing in the lower plenum. It is expected that the distribution of coolant temperature at the core inlet has an important effect on the core behaviour.

To investigate this effect the calculation is compared with two other calculations. In the second calculation the coolant mixing in the lower plenum is treated by means of the mixing model for VVER-440 reactors which is included in the code DYN3D. This model is based on the analytical solution of the Navier-Stokes equations in the potential flow approximation in 3-dimensional cylindrical geometry and the diffusion equation for heat transport or soluble boron. Turbulent Peclet numbers for the downcomer and the lower plenum region are the governing parameters of the model which have been used for a best fit to experimental results [3]. In the third calculation coolant mixing in the lower plenum was excluded. Each loop was connected to a particular 1/6 sector of the core.

In order to take mixing into account the core must be described as full core. That means that all 349 fuel elements have to be included into the calculation. A reduction to a symmetry sector (30 or 60 degrees) is not possible. Further, as explained in [1], the mixing model can be used only in the case of external coupling. For this reason all three calculations were made with this type of coupling of DYN3D with ATHLET.

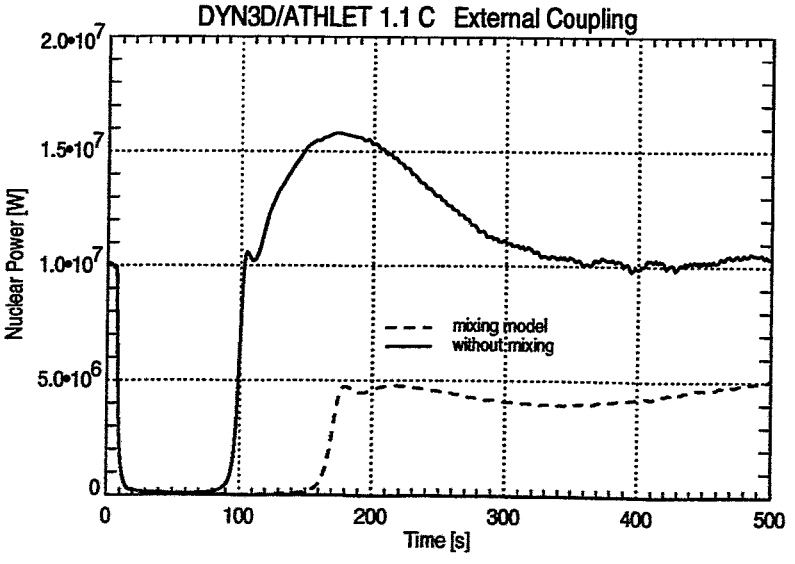


Fig. 2: Nuclear power after MSLB in the case of different coolant mixing in the lower plenum

In the calculation without any mixing the positive reactivity insertion caused by the coolant temperature decrease is going to compensate the scram reactivity faster. At t=92s the scram reactivity is compensated. Recriticality is reached. Due to the continuous fall of the coolant temperature the reactivity continues to increase and as a consequence the power rises, too (Fig. 2). At t=170s the power increase is stopped due to the feedback effects. Then the total reactivity is dominated by the FTC. The power is stabilized at about the initial level.

The mixing model provides a realistic distribution of the coolant temperature in the lower plenum which is between the extreme cases ideal mixing and no mixing. Since the temperature distribution reduces the MTC effect, the scram reactivity is compensated later (t=156s). Around this time the coolant temperature reaches the minimum value and the maximum power value is smaller (Fig. 2).

As expected the change of coolant mixing conditions has negligible effects on the secondary circuit. The coolant temperature of the broken loop in the primary side is almost the same in all three calculations.

## 4. Conclusions

As a first application of the coupled code DYN3D/ATHLET to accident scenarios with asymmetric effects a MSLB analysis at HZP for VVER-440 was performed. Different coolant mixing conditions in the lower plenum were simulated. The results show the importance of these conditions. In the calculations with a realistic mixing model and without mixing a recriticality after reactor scram was predicted. Due to the fact, that the MSLB analysis was performed for HZP conditions a dangerous fuel temperature increase was not reached. Nevertheless, the fact of return-to-power not only for the conservative assumption of no mixing but also for the mixing model is an important result of this analysis. In the future the investigated accident will become more important, especially in connection with the burn-up increase. In this case the delayed neutron fraction is smaller and during the recriticality the prompt critical margin potentially could be reached.

## References


[1] U. Grundmann, D. Lucas, S. Mittag und U. Rohde: Weiterentwicklung und Verifikation eines dreidimensionalen Kernmodells für Reaktoren vom Typ WWER und seine Ankopplung an den Störfallcode ATHLET, Report FZR-84, Rossendorf, April 1995

[2] H.-J. Paik and P. Raymond: PWR SLB Analysis by means of Coupled 3-D Neutronic, 3-D Core Thermohydraulic, and Fast Running System Codes, Nuclear Technology, v.107, July 1994, p.103

[3] P. Dräger: Makroskopische Kühlmittelvermischung in Druckwasserreaktoren, Dissertation, Ingenieurhochschule Zittau, 1987



*The project this paper is based on is funded by the BMBF (Bundesministerium für Bildung, Wissenschaft, Forschung und Technologie) and is registered with No. 150 0925A.*

# THEORETICAL AND EXPERIMENTAL INVESTIGATIONS OF NATURAL CIRCULATION PHENOMENA IN VVER-TYPE REACTORS AT LOSS OF COOLANT ACCIDENT CONDITIONS

**F. Schäfer**

## 1. Introduction

An important component of nuclear safety research is the analysis of abnormal transients and accident scenarios in nuclear power plants. Such analyses are usually carried out with complex thermohydraulic computer codes, which must be validated through the comparison of calculated results with experimental data. In the presented work the ATHLET code of GRS was used for calculations of small and intermediate loss of coolant accident experiments, which were performed at the Hungarian test facility PMK-2. ATHLET has originally been developed for modelling western-type nuclear power plants and so the validation for reactors like VVER-440 and corresponding test facilities is an important task in nuclear safety research. The Institute of Safety Research has participated in various International Standard Problem Exercises and also in various experimental programs related to VVER-thermohydraulics. The Institute of Safety Research is also involved in the external validation of the ATHLET code. In co-operation with KFKI Atomic Energy Research Institute Budapest a series of LOCA experiments were performed at the PMK-2 test facility (Fig.1).

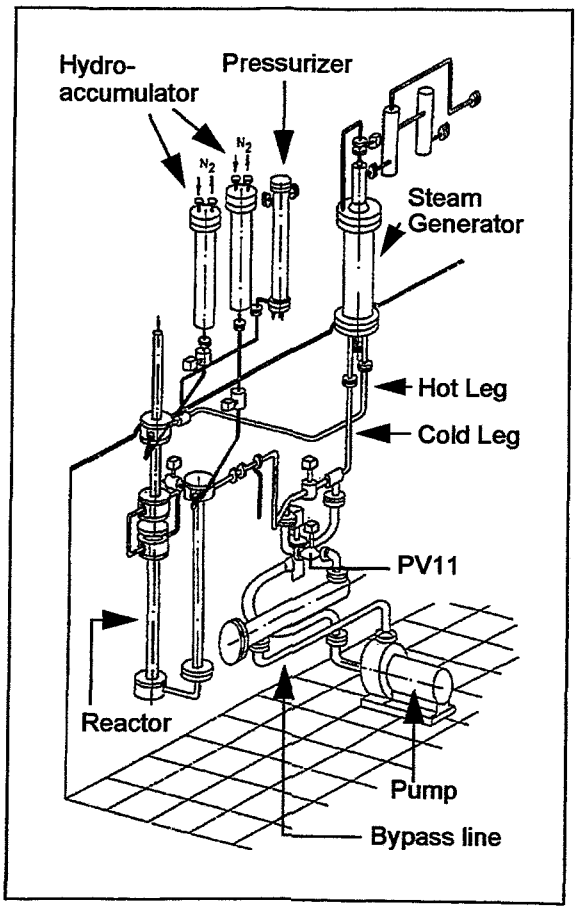


Fig.1: Axonometric view of PMK-2

LOCA experiments are characterized by a more or less rapid primary pressure decrease in the early phase of the transient. After pump coast down natural circulation becomes the dominant decay heat removal mechanism. A few hundred seconds after leak initiation boiling in the reactor core leads to formation of two-phase flow conditions in the primary circuit. At these conditions different types of two-phase flow instabilities can appear. The instabilities play an important role in the behavior of the primary circuit, because the instabilities can disturb the decay heat removal from the reactor core.The appearance of such instabilities strongly depends on the thermohydraulic and geometrical conditions in the loop. At the PMK-2 test facility natural circulation instabilities could be detected in 3 different experiments.

The ATHLET calculations provide detailed information required to clarify the complex processes connected with the different kinds of instabilities.

## 2. The PMK-2 Test Facility

The PMK-2 test facility (see Fig.1) is a full-pressure, volume-scaled model of the Paks Nuclear Power Plant. The facility was constructed by the KFKI Atomic Energy Research Institute Budapest and is mainly designed to investigate processes following small and medium size breaks in the primary circuit and to study the natural circulation behavior of VVER-440 type reactors. The 6 loops of the plant are modelled by a single active loop with a scaling ratio of 1:2070. The core model consists of a 19-rod bundle with axially and radially uniform power distribution. The steam generator consists at the primary side of a hot and cold collector and 82 heat transfer tubes. The main coolant pump is installed in a bypass line. During steady state operation circulation takes place through the bypass line. Pump trip modelling is achieved by controlling the pump flow rate with a valve. After pump coast down the bypass line is seperated from the loop. An overview about PMK-2 characteristics is given in Fig.1 and Table1.

| | |
|---|---|
| **Reference NPP:** | Paks Nuclear Power Plant<br>VVER-440/213 reactor - 6 loops<br>1375 $MW_{th}$ |
| **General scaling factor:** | Power, volumes: 1:2070<br>Elevations: 1:1 |
| **Primary coolant system:** | Pressure: 12.4 MPa<br>Core inlet temperature: 540 K<br>Core power: 664 kW<br>Nominal flow rate: 4.5 kg/s |
| **Secondary coolant system:** | Pressure 4.6 MPa<br>Feed water temperature: 493K<br>Nominal steam mass flow: 0.36 kg/s |
| **Safety injection systems:** | High pressure injection system (HPIS)<br>Low pressure injection system (LPIS)<br>Hydroaccumulators (Safety Injection Tank)<br>Emergency feed water system (EFWS) |

Table1: Main characteristics of PMK-2

## 3. Thermohydraulic Model

The presented results were obtained with the thermohydraulic code ATHLET Mod 1.1 Cycle A. The calculations are carried out at a Sun Workstation SPARC 10/40.

For modelling the thermofluid objects in general the four equation model of ATHLET is used. The complete PMK model consists of 104 control volumes, 109 junctions and 126 heat conduction volumes. The nodalization scheme is presented in Fig.2a. In most of the control volumes the flooding based drift model is applied. The wall friction is considered by using the Martinelli Nelson friction model and the one dimensional steady state critical discharge model is applied for calculating the break flow. Before starting the transient, a steady state calculation at stationary boundary conditions is performed over 1000 s. During this time the stationary mass flow in the primary loop,

the pressure differences and the heat losses are adjusted. The initiation of power scram, pump coast down and the start of the emergency cooling systems is controlled by the primary pressure. The time dependence of the reactor power is assumed according to the decay heat curve.

Fig.2b shows the measurement positions at PMK-2 referred to in the following chapters.

## 4. Experiments

The 3 selected experiments are characterized as follows:

*1% cold leg break (1%CLB):*

- small break in the upper head of the downcomer (diameter 1mm)
- starting at nominal conditions (PW01=658 kW, PR21=12.4 MPa, PR81=4.5 MPa)
- steam generator is isolated after transient initiation
- with injection from the high pressure injection system and without injection from hydroaccumulators

*1% cold leg break with primary bleed:*

- same initial conditions as in the 1% cold leg break case
- additionally an accident management measure is realized by opening the pressurizer safety valve

*Surge line break (SLB):*

- break in the pressurizer surge line (diameter 5 mm)
- starting at nominal conditions (PW01=681 kW, PR21=11.85 MPa, PR81=4.8 MPa)
- steam generator is isolated after transient initiation
- with injection from hydroaccumulators and high pressure injection system

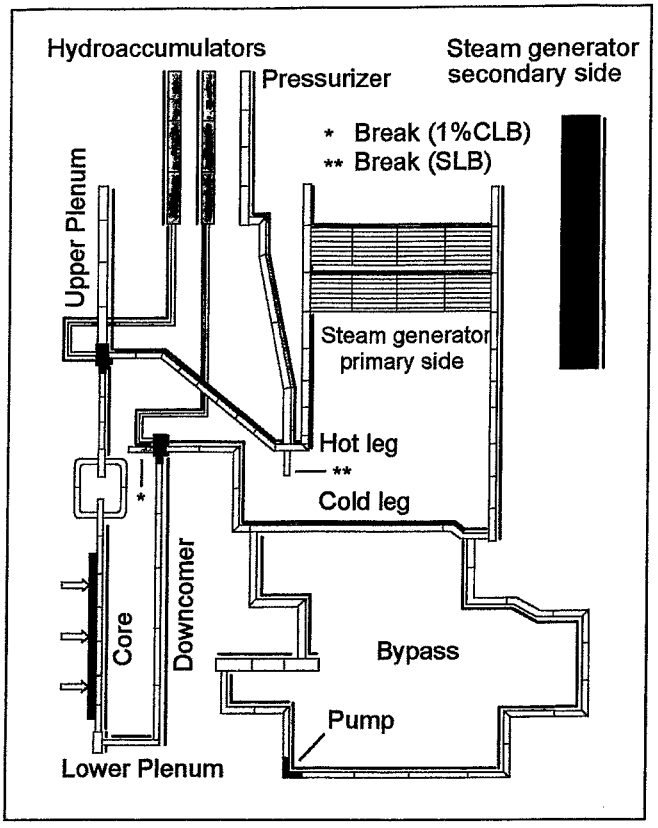


Fig.2a: Nodalization scheme of PMK-2

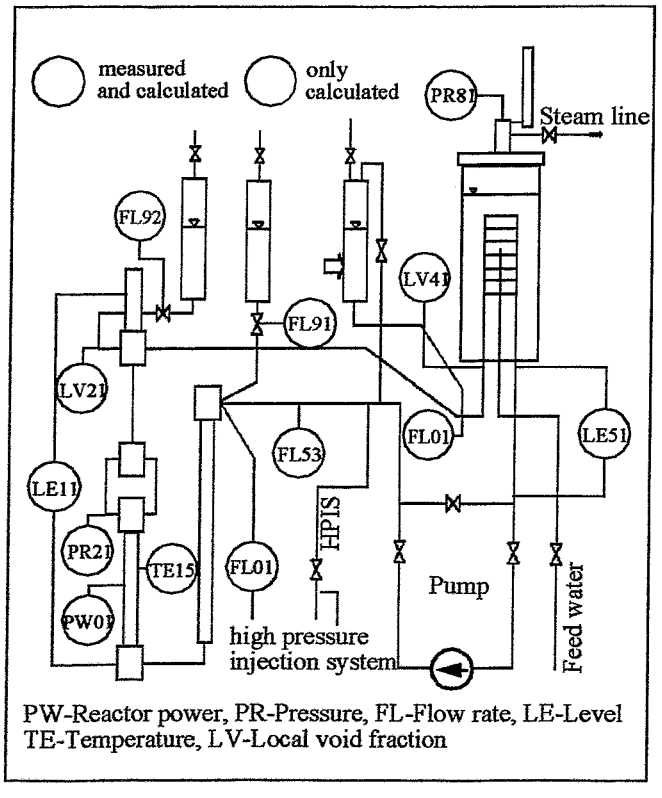


Fig.2b: Measurement positions at PMK-2

## 5. Results

*1% cold leg break:* The experiment starts with initiation of the break valve at t=0s. Simultaneously the steam generator is isolated by closing the feed water line and the steam line. The whole transient lasts about 4000s. The time dependence of the primary and secondary pressure up to1000s is shown in Fig.3. In this part of the transient the following phenomena can be observed:

- Opening the break valve results in a fast decrease of the primary pressure. This pressure decrease is accelerated due to the start of scram and pump coast down. Because of the continuous heat transfer from the primary to the secondary side at first the secondary pressure increases and the steam generator relief valve opens.
- After closing the steam generator relief valve (t=170s) the heat transfer to the secondary side is reduced. At the same time boiling starts in the reactor core and the primary pressure deacrease stagnates. After the pump has stopped the primary pressure decreases only slowly and even starts to rise at appr. 600s (550s in the experiment). In this period the natural circulation is interrupted due to the effect of the hot leg loop seal.
- At t=760s the level in the inclined part of the hot leg reaches a minimum. The steam generated in the core enters the steam generator hot collector and the loop seal clearing takes place. During the time interval from 760s to 1250s both calculation and experiment show oscillations with a time period of appr. 20s (Fig.4). The results of the calculation show that this kind of natural circulation instabilities are caused by vaporization and condensation effects in the reactor model and steam generator inlet:

As a consequence of condensation in the steam generator inlet the primary pressure decreases. The steam flow from the reactor to the steam generator leads to an increase of the mass flow (FL53) and also the reactor level increases. The rise of the reactor level leads to a reduced void fraction at the reactor outlet and as a result there is less condensation in the steam generator. The phase-shift between void fraction at reactor outlet (LV21) and steam generator inlet (LV41) amounts to 180 degrees. When the primary pressure reaches a local minimum, for a short period the mass flow rate is negative. The calculation shows that there is a fluid mass flow directed from the steam generator inlet to the hot leg. This fluid mass flow and the rising water level in the reactor leads to a refilling of the hot leg loop seal from both ends. Once more the primary pressure increases and the described process is repeated periodically.

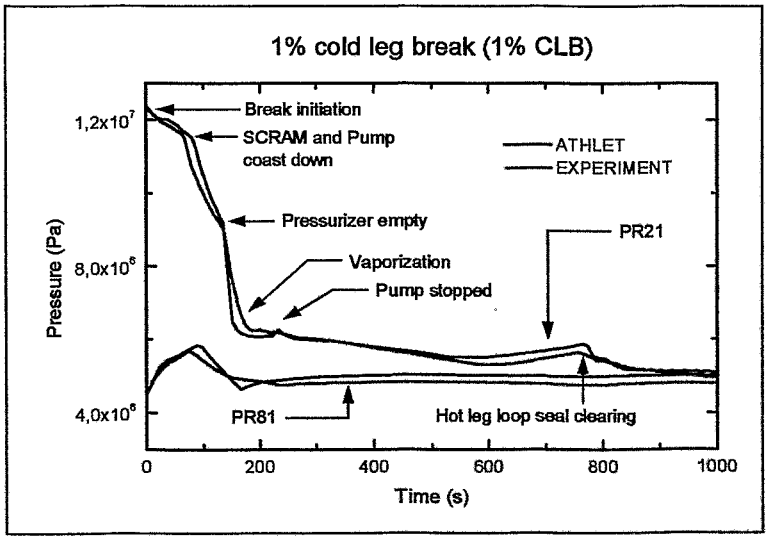


Fig.3: Primary (PR21) and secondary pressure (PR81)

The unstable behavior connected with the hot leg loop seal clearing ends at t=1250s. Afterwards the reactor level decreases, steam from the hot leg enters the steam generator cold collector and the level in the steam generator cold collector starts to drop. The level decrease in both reactor model (LE11) and cold leg (LE51) is accompanied by a different kind of oscillations in the time period from 1500s to 1800s (Fig.5). The instabilities are initiated by the decreasing cold leg mass flow, in the course of which a flow reversal can be observed in the lower plenum and the downcomer. That means there is a mass flow from the reactor towards the break and a mass flow from the steam generator cold collector towards the break. The phase-shift between both mass flows amounts to 180 degrees and the resulting mass flow leads to periodical changes in the break flow. An increasing break flow leads to a faster decrease of the levels (LE11, LE51) and vice versa. In case of the described instabilities the calculation was very useful to clarify the more complex processes.

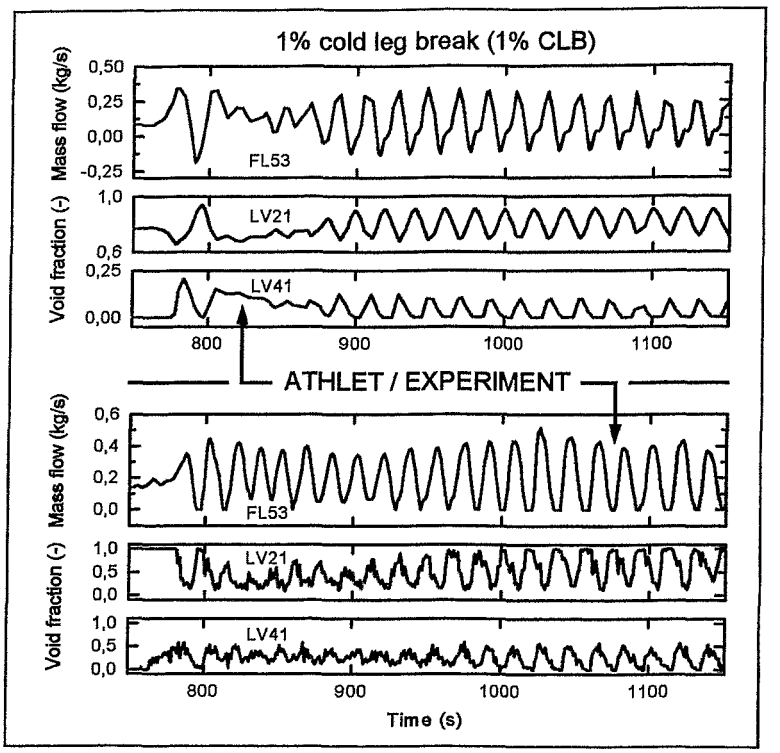


Fig.4: Instabilities in the cold leg mass flow (FL53) and in the void fraction at reactor outlet (LV21) and steam generator inlet (LV41)

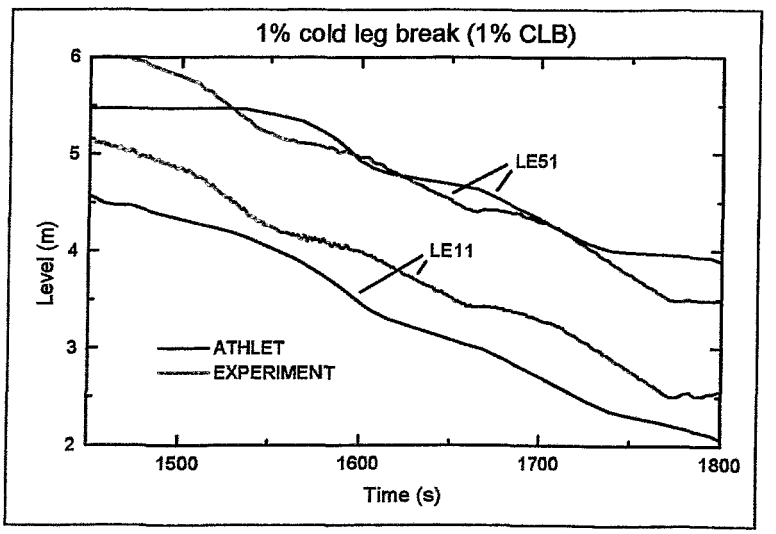


Fig.5: Instabilities in the reactor level (LE11) and in the cold leg level (LE51)

In the second part of the experiment an extended dry out period in the core takes place at t=1810s (1730s in the experiment, Fig.6). In this period the primary pressure falls below the secondary pressure and the heat removal from primary to secondary side is practically zero. Due to the steam flow from the steam generator towards the cold leg, fluid from the cold leg flows to the core and the cold leg loop seal clearing takes place. The reactor level rises again and so the

dry out period is limited. After the cold leg loop seal clearing the break mass flow is nearly equal to the mass flow rate from the high pressure injection system. Thereby at the end of the transient the reactor level stagnates at a constant level and the long term core cooling is ensured up to the end of the transient. The ATHLET code also calculates the effects of dry out and cold leg loop seal clearing in very good agreement with the experiment.

*1% cold leg break with primary bleed:* In general the course of events corresponds to the 1%CLB experiment. Additionally an accident management measure is realized by manual opening of the pressurizer safety valve at t=643s. The aim of this accident management measure is to prevent the dry out period in the core. Due to the additional depressurization the primary pressure decreases faster than in the 1%CLB experiment and the natural circulation instabilities in the hot leg lasts only from t=750s to t=950s (Fig.7). Already at appr. t=900s the primary pressure falls below the secondary pressure and at t=1250s the cold leg loop seal clearing takes place. If the steam flow from the cold leg reaches the break position, the break mass flow is reduced and the reactor level stagnates at 2.5m (4,5m in the experiment) instead at 2m (3m in the experiment) in the CLB experiment (Fig.7). In this way the dry out period could be prevented.

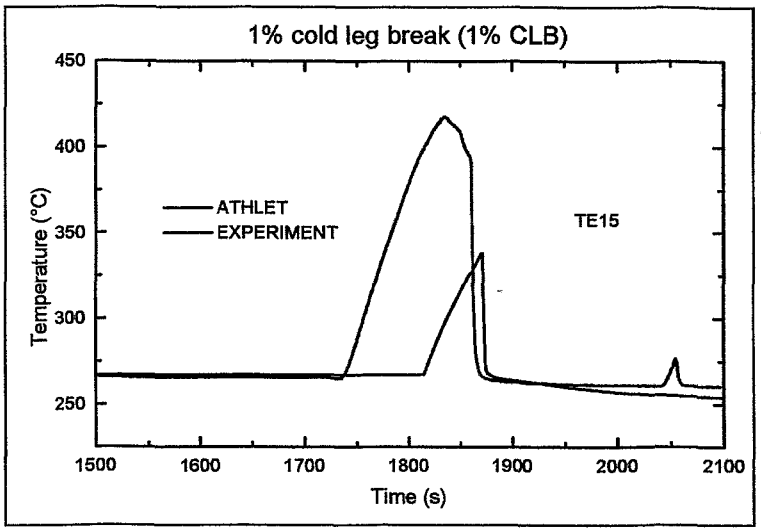


Fig.6: Cladding temperature (TE15) in the reactor core

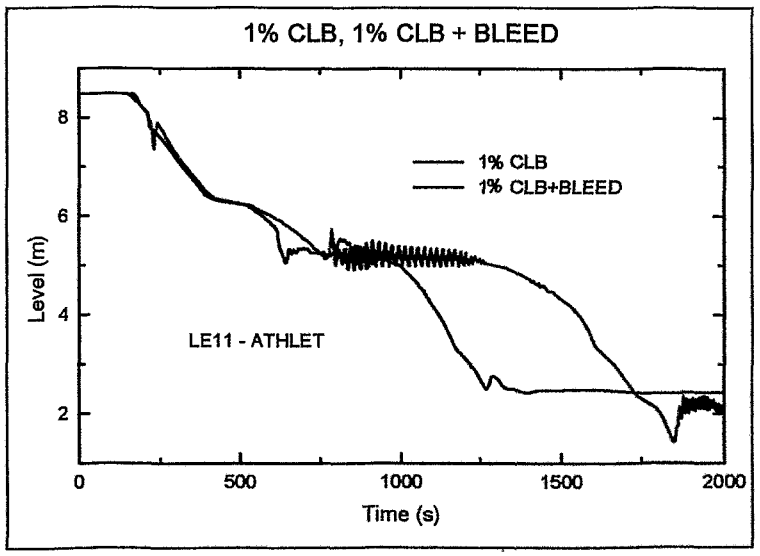


Fig.7: Level in the reactor model (LE11) - calculation

*Surge line break:* The SLB experiment starts with initiation of the break valve at t=0s. Simultaneously the steam generator is isolated by closing the feed water line and the steam line. The break is located in the hot leg at the connection between hot leg and surge line. In the experiment the high pressure injection system and the hydroaccumulators are activated. The whole transient lasts about 1265s. Due to a fault in the experimental scenario, a certain amount of nitrogen was injected from the hydroaccumulator connected with the upper part of downcomer.

Due to the break the pressure decreases very fast in the early phase of the experiment. Already at t=1s the reactor scram and the high pressure injection system are initiated and at t=3s the pump coast down starts. The coolant vaporizes at first in the hot leg loop seal and immediately afterwards in the reactor and steam generator inlet. At t=25s the primary pressure reaches the setpoint of hydroaccumulator injection. Therefore the vaporization in the hot leg is temporarily stopped. Due to boiling in the core the pressure decrease stagnates and the injection from the hydroaccumulators is reduced (FL91/92, Fig.8). In this period the injected water in the upper plenum flows only towards the hot leg and the break mass flow (FL01) increases. The effect of countercurrent flow limitation in the upper plenum lasts up to 160s. The injection from the hydroaccumulators is stopped at t=205s (upper plenum, FL92) and t=235s (downcomer, FL91). At the end of the hydroaccumulator injection (FL91) nitrogen is injected into the upper part of the downcomer. The effect of this nitrogen bubble can be seen in the reactor level. In the experiment LE11 rises again. The used version of ATHLET could not calculate the effects of noncondensable gases and so the calculated reactor level further decreases (Fig.8). If the hydroaccumulator injection has stopped the coolant in the hot leg vaporizes again and the steam generator primary side is filled with steam.

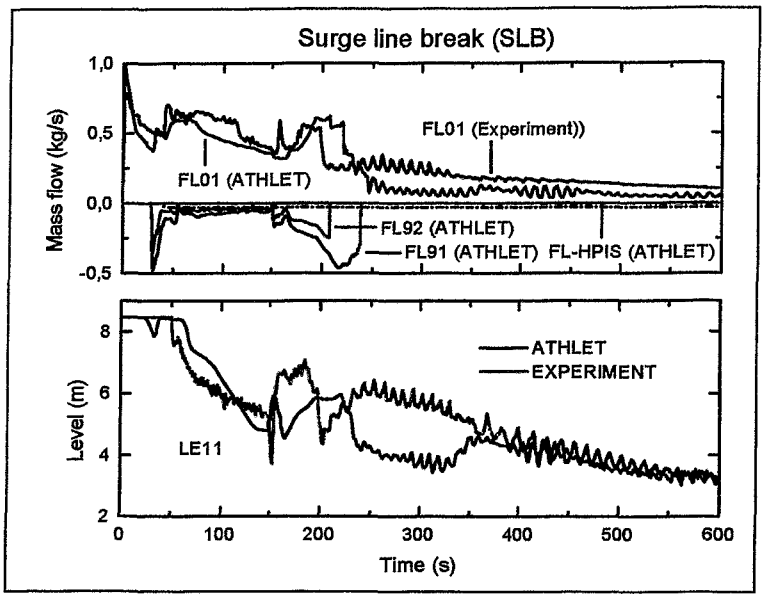


Fig.8: Instabilities in reactor level (LE11) and break flow (FL01) and the injected mass flow from emergency cooling systems (FL-HPIS, FL91, FL92)

Two kinds of natural circulation instabilities can be observed in the further course of the transient. At t=200s instabilities in the hot leg loop seal occur with a period of approximately 10s. These oscillations are caused by periodical changes in the break flow (FL01). At the break position a transition regime between water, two-phase and steam flow can be observed, which is coupled with periodical changes in the reactor level. At t=350s the void fraction at reactor outlet reaches 100% and the instabilities in the hot leg are stopped. The unstable behavior in this period is correctly modelled by ATHLET (Fig.8). At t=350s the primary loop changes again to an unstable state. Due to vaporization in the cold leg two-phase mixture is pushed into the steam generator cold collector. In this period the primary pressure is lower than the secondary pressure. As a result the two phase mixture in the steam generator cold collector will be vaporized and the cold collector level drops down. Due to vaporization in the cold leg the mixture level in the steam generator cold collector rises again and the process is repeated periodically with a time period of 15s. The described process can exactly be illustrated by the measured results. The calculation fails to predict this kind of instabilities. Possibly a reason for these deviations is the influence of the injected nitrogen. Further calculations with the latest version of ATHLET will help to investigate these effects in more detail.

## References


[1] Gy. Ezsöl, A. Guba, L. Perneczky, H.-M. Prasser, F. Schäfer, E. Krepper: 1% Cold leg break experiment on PMK-2 - Test results and computer code analysis
Forschungszentrum Rossendorf e.V., Report FZR-76, March 1995

[2] F. Schäfer, E. Krepper: Rechnungen zum 1%-Leck an der Versuchsanlage PMK-2 mit dem Code ATHLET
Jahrestagung Kerntechnik, Nürnberg 16.-18. Mai 1995, Tagungsbericht, S. 79-82

[3] Gy. Ezsöl, A. Guba, H.-M. Prasser, F. Schäfer: Small Cold Leg Break Experiment on PMK-2
Jahrestagung Kerntechnik, Nürnberg 16.-18. Mai 1995, Tagungsbericht. S.119-122

[4] Description of the PMK-NVH Facility
KFKI Atomic Energy Research Institute Budapest, 1990

[5] L. Perneczky, G. Ézsöl, L. Szabados: 1% Cold Leg SBLOCA Analysis on PMK-NVH Facility
Central Research Institute for Physics, Budapest, 1990



*The project this report is based on is funded by the Saxonian State Ministry of Science and Art and is registered with No. 4-7541.82-FZR/301.*

# OSCILLATIONS OF THE MASS FLOW RATE AT PRESSURE RELIEF SYSTEMS

**D. Lucas, H.-M. Prasser**

## 1. Introduction

During two–phase blowdown from pressure vessels considerable pulsations of the discharged mass flow rate were found. Regions of instability were predicted by a linear stability analysis. The oscillations are caused by the following feedback circuit: boil up – level movement – void fraction of the discharged mixture – critical discharge rate – velocity of pressure decrease – boil up.

The object of investigation is a pressure vessel, which is equipped with a vertical ventline at the top. The relief device (critical diameter) is located at the top of the ventline. After starting the relief the pressure decreases. Evaporation or degasation of the liquid inventory of the vessel is the consequence. This leads to a level swell. If the mixture level reaches the ventline, the previously vented gas flow changes to two–phase discharge. The mixture arrives at the relief device after a certain delay (time of transport). The critical discharge rate strongly depends on the void fraction in the critical discharge area. The decrease of void fraction results in a decrease of volume release, which is connected with a decrease of the velocity of depressurisation. This leads to a reduction of the gas production in the vessel. Under certain circumstances the mixture level then starts to go down and the discharge flow changes again to pure gas. When the gas reaches the relief device, the depressurisation velocity increases again causing a reestablished level swell [1].

At the top of a two–phase mixture a more or less developed foam region can be always found. It prevents a sudden change between one–phase and two–phase discharge. Therefore, continuous change of the void fraction in case of small level fluctuations is more likely. This has to be considered in the stability analysis.

## 2. Analysis of stability

The method of linear stability analysis as described in [1] was applied to an evaporating fluid. The void fraction at the entrance of the ventline was chosen as initial disturbance. The following elements of the transfer function were considered and formulated in the Laplacian space (see Fig. 1):

1. The ventline was approximated by assuming a linear all pass behaviour with a given delay time.
2. The critical mass flow rate depends on the void fraction at the entrance of the relief device. A transfer coefficient was derived from a critical discharge model.
3. The conversion of the mass flow rate to a volume flow rate supplies transfer coefficients describing the disturbance of the drain of volumes in terms of vessel volume due to the discharge.
4. The released volume has to be compensated by expansion and evaporation. The transfer coefficient between the velocity of the pressure decrease and the released volume flow was calculated from the volume balance using a non–equilibrium

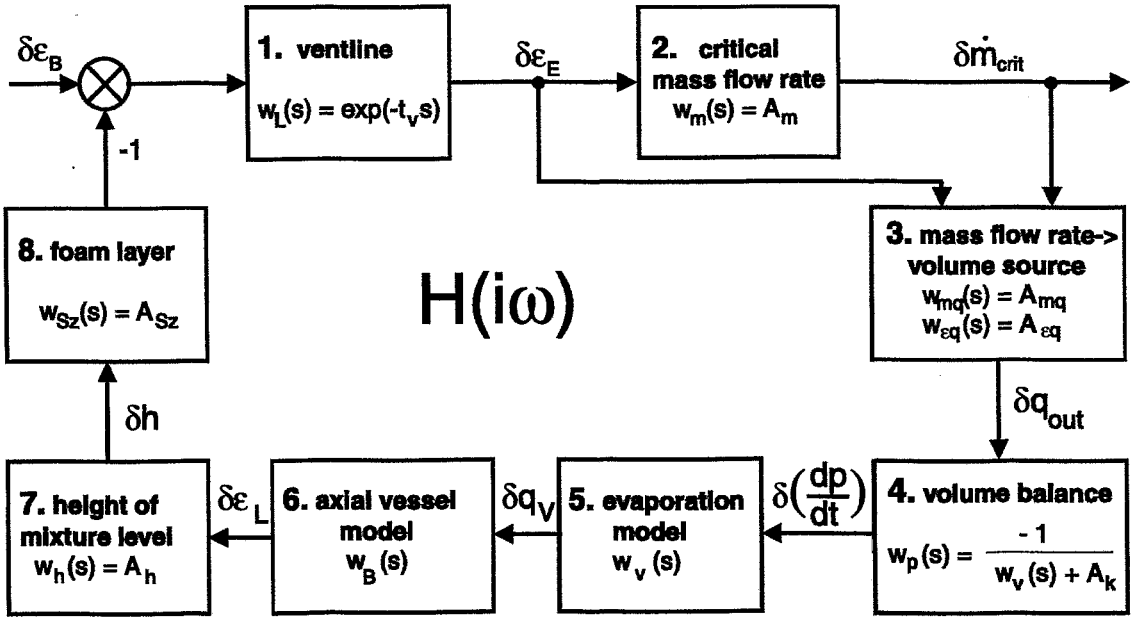


Fig.1: Scheme for the transfer of small disturbances

model for evaporation.

5. The non–equilibrium evaporation model was also used for determining the volume source of the generated steam.
6. The change of the axial void fraction profile inside the vessel is caused by the changing volume source of steam. It was described by an analytical model. The bubble rise velocity was assumed to be constant over the height of the vessel. The local volume source of steam was considered to be proportional to the local volume fraction of the liquid phase.
7. The volume balance for the liquid is used to calculate the displacement of the mixture level.
8. The resulting change of the void fraction at the entrance of the ventline was calculated under the assumption of a linear growth of the void fraction in the foam layer. The height of the foam layer was determined applying a correlation from the literature [2].

The transfer functions 1 to 8 allow to describe the feedback of a small initial disturbance to the void fraction at the inlet of the ventline. The described system will oscillate if the disturbance in phase feeds back on the ventline void fraction with an amplification greater than one. This corresponds to the Nyquist–criteria, which is well known in automation theory.

For the coupled system, Nyquist–plots for different parameter combinations were analysed to find regions of instability. It was found that the tendency to oscillations increases with growing void fraction at the relief device, with increasing delay time in the ventline (large volumes of the ventline) and with decreasing height of the foam layer.

## 3. Transient calculations

Time dependent calculations were performed with the BLDN-code [3-5], which has been developed at the Research Center Rossendorf. The BLDN vessel model was modified by adding a ventline simply modeled as a delay pipe. The BLDN code uses the above mentioned model for the foam layer [2], which assumes a linear growth of the void fraction within the foam layer. That means, if the level goes down, the void fraction at the inlet of the ventline tends to 1. Regions of discharge void fractions close to 1 are always passed through during the blow down process. As mentioned above the ability to oscillate increases with the void fraction at the relief device. That means to get a stable system there has to be stability for a void fraction $\varepsilon \dashrightarrow 1$.

The oscillations were confirmed numerically by these transient calculations. The simulations were started with completely filled vessel. During the depressurization the void fraction increased at the entrance into the ventline. The oscillations occurred when the void fraction reached the critical value predicted by the linear stability analysis. The results of both methods show a good quantitative agreement of the calculated limitis of stability and of the frequencies of the first oscillations at these limits.

## 4. Experiments

Experiments were carried out with water/steam at the Pressurizer Test Facility at Hoch schule für Technik, Wirtschaft und Sozialwesen Zittau/Görlitz (FH). For this purpose the pressure vessel was equipped with a 1.8 m long ventline with an inner diameter of 25 mm. The diameter of the relief device was 6 mm. The pulsations were confirmed qualitatively. They caused periodical changes of the noise generated by the discharging mixture. Oscillations were found in the readings of the pressure drop over the ventline as well as in the signals of the needle shaped conductivity probes that measure the local void fraction (see Fig. 2). The frequencies of the oscillations were about three times smaller than the frequencies predicted by transient calculations. The most important reason for that is assumed to be the neglection of the slip velocity within the ventline.

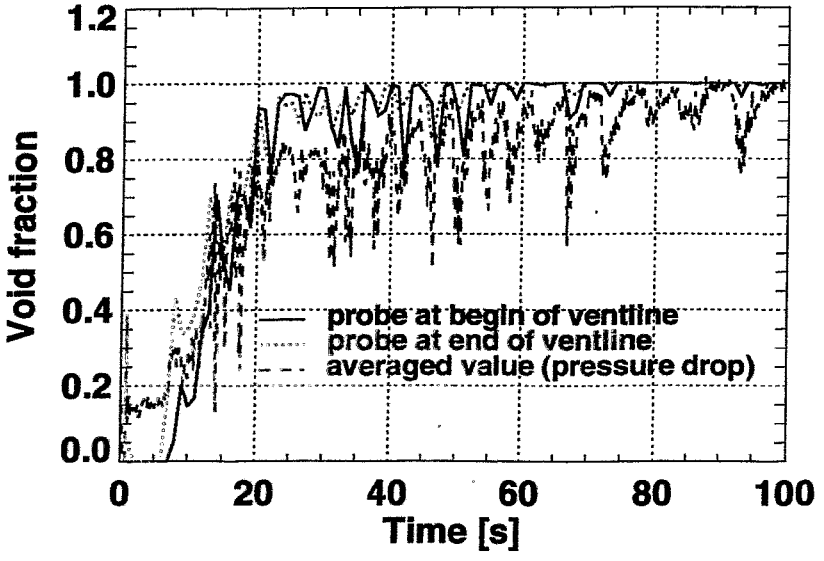


Fig. 2: Measured Oscillations of the void fraction - vessel diameter 0.274 m, vessel height 3 m, initial pressure 2.25 MPa

## 5. Conclusions

Oscillations of the void fraction of the discharged two-phase mixture connected with considerable pulsations of the discharge mass flow rate were predicted by linaear stability analysis and by transient calculations. They were confirmed qualitatively by first experiments. To achieve a better quantitative agreement between calculations and experiments a more detailed modeling of foam layer, fluid entrainment and ventline as well as some modifications of the experimental setup are necessary.

The probability of the pulsations rises with the volume of the ventline between vessel and relief device. It could be possible that these pulsations lead to additional mechanical loads on the blow down system and that they influence the efficiency of seperators or condensers. In addition to the mechanism of the oscillations considered here, also other mechnisms are possible, e.g. a spontaneous transition to a slug flow regime within the ventline.

## Literature


[1] D. Lucas, H.-M. Prasser: "Schwankungen des Massenstroms bei Druckentlastungsvorgängen", 3. Fachtagung Anlagen-, Arbeits- und Umweltsicherheit, Köthen, 7./8. November 1996, Preprints, p. 233-240

[2] A.M, Kutepov, L.S. Sterman, N.G. Stjushin: "Hydrodynamics and Heat Exchange-at Steam Generation (Gidrodynamika i teploobmen pri paroobrazovanii)", published by Vysshaja Shkola, Moscow 1986, p. 92–108

[3] H.-M. Prasser "Ein mathematisches Modell zur Zweiphasenströmung in einem zylindrischen Druckgefäß bei kleinen Lecks", Kernenergie 25(1982)294

[4] H.-M. Prasser, H. Steinkamp, U. Rohde: "Aufwallen und Austragen von zweiphasigen Gemischen", DECHEMA-Jahrestagung 1995, 30.05.- 01.06. 1995, Wiesbaden

[5] B. Gebbeken, H.-M. Prasser, R. Eggers: "Entspannungsverdampfung während der Druckentlastung von $CO_2$ aus dem überkritischen Anfangszustand", GVC-Fachausschuß Mehrphasenstömungen, Lahnstein, 6.3.-8.3. 1996



*This work is supported by the Volkswagenstiftung.*

# SIMULATION OF THE SINGLE PHASE NATURAL CIRCULATION AT THE SECONDARY SIDE OF AN EMERGENCY CONDENSER (NOKO FACILITY) USING THE CFD-CODE CFX-4

**A. Aszódi, E. Krepper**

## 1. Introduction

The NOKO-Test facility is a rig for the test of passive components of nuclear power plants and is operated at the research centre Jülich [1]. The facility is used for the experimental investigation of the emergency condenser of the SWR 600/1000, which is a new boiling water reactor design, developed by Siemens. The main part of the facility consists of a horizontal cylindrical tank with a length of 6.4 m and a diameter of 2 m [2]. In the inner part of the tank a bundle of 8 U-shaped tubes is situated. The length of the U-tubes is 9.8 m and the diameter of each tube amounts to 38.7 mm. Outside of the bundle two vertical baffle plates are arranged for flow control purposes.

At normal conditions of reactor operation, the U-tubes of the emergency condenser are filled with water and almost no heat transfer takes place. In case of an accident with decreasing water level in the reactor core, the water in the U-tubes is replaced by steam. The steam in the tubes is condensed and considerable heat is transferred to the secondary side of the emergency condenser. At the same time at the secondary side of the condenser firstly single phase and later two phase natural circulation is established.

Until now, the heat transfer and the physical processes at the primary side of the condenser were investigated in detail [1-2]. The deeper investigation of the natural circulation processes at the secondary side has not yet been performed.

Former works [3] have shown, that under special circumstances a very stable temperature stratification may occur and vertical temperature differences of some 10 degrees may be established. To verify the possibility of creation of such a stratification at the secondary side of the NOKO test facility, some simulations using the CFD-code CFX-4 were performed.

## 2. Specification of the problem

For simplification the condenser was modelled only in two dimensions. A vertical section through the tank was considered. The cross section plane was placed centred to the bundle. The arrangement of the tube and the baffle plates were modelled in detail ([1, 2], see Fig. 5). The surface of water was modelled by a free slip wall (see Fig. 1). The steam volume above the water was not considered. The whole grid consisted of about 18000 cells.
The heat loss from the walls and the water surface was not considered and the heat transfer of the baffle plates was not taken into consideration. The calculations were performed as time dependent transients. An equal distribution of temperature at 300 K and no motion of the fluid were assumed as initial state. The simulation was

limited to the single phase period. First of all, no turbulence model was applied. In the following simulations the heat transfer power is given as a boundary condition. Assuming a condenser power of 2.5 MW and 8 tubes in operation, a heat transfer of $2.235 \cdot 10^5$ W/m$^2$ was derived.

### 3. The results of the calculations

For the presentation of the time dependencies of temperature, several points in the condenser tank were selected (see Figure 1). The results show clearly, that a vertical temperature stratification is established (see Figures 2a and 2b). Even after 200 seconds the temperature difference between two points each 500 millimetres above and below the tank centre amounts to 15 K. At the surface after 1200 seconds the saturation temperature is reached. At this time, the temperature difference between the two points amounts to about 20 K. At the bottom of the tank, a dead volume is established, which does not take part in the natural circulation. In this volume no substantial temperature increase takes place. In the bundle, temperature oscillations are observed (see Figure 2b).

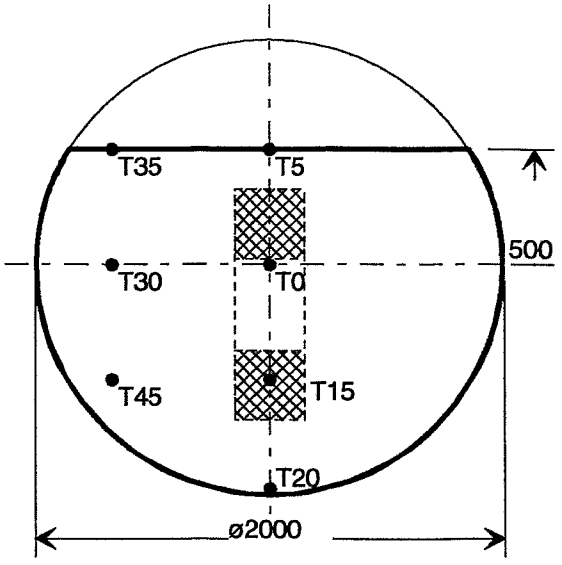


Fig. 1: Selection of points for the representation of temperature courses

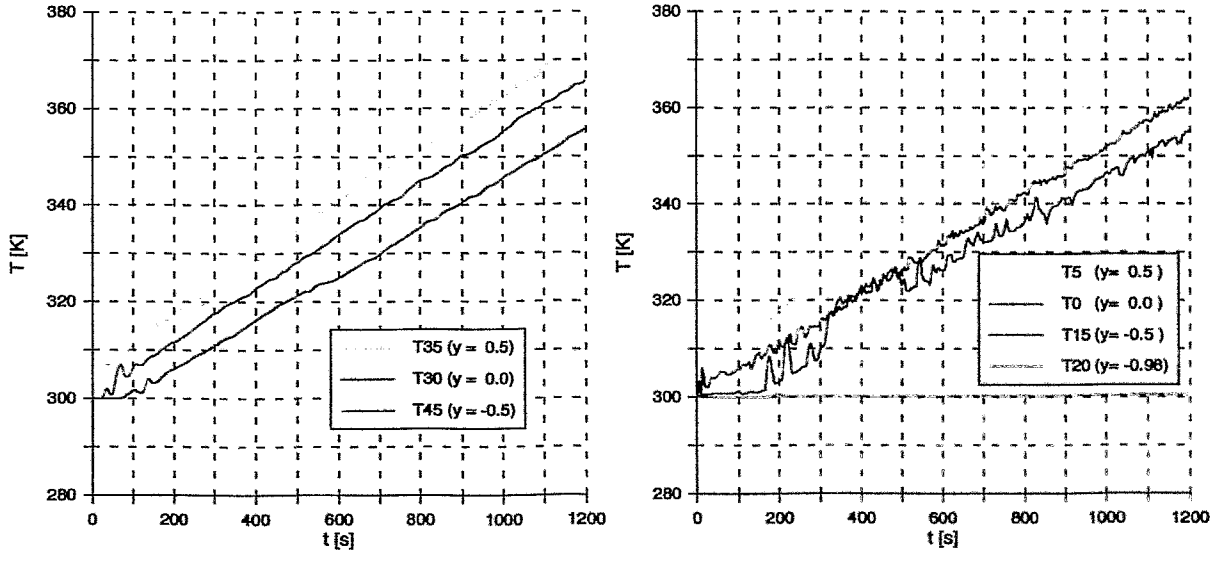


Fig. 2: Fluid temperature courses at x = -0.7 (left side) and x = 0.0 (right side) (see also Fig. 1)

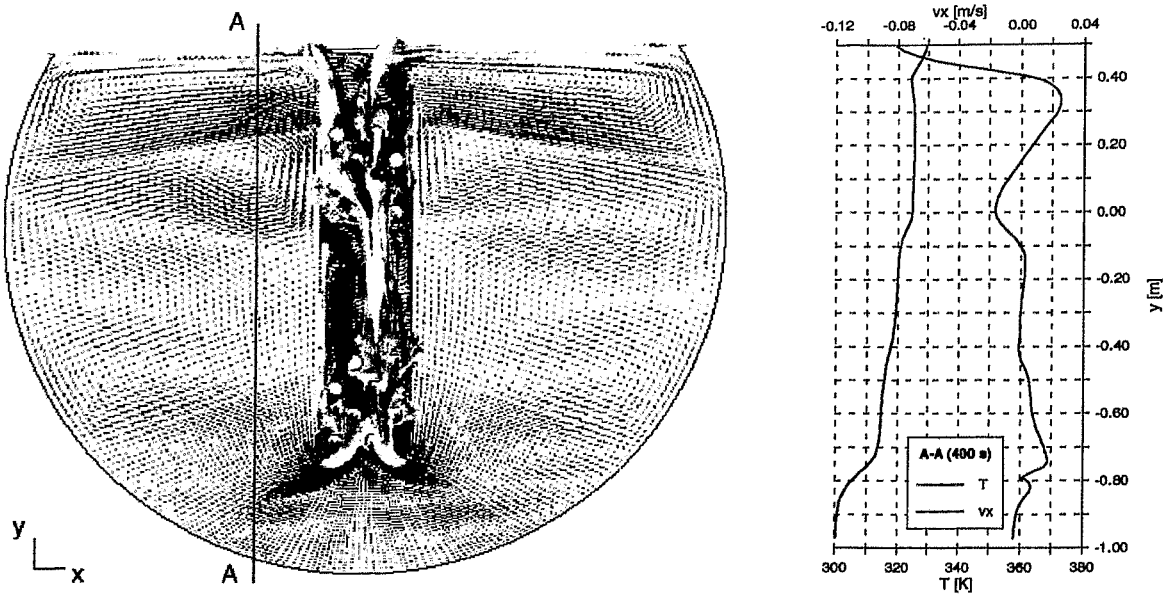


Fig. 3: Velocity field after 400 seconds and axial profiles of temperature and hori - zontal velocity vx along the line A-A (x = -0.20 m)

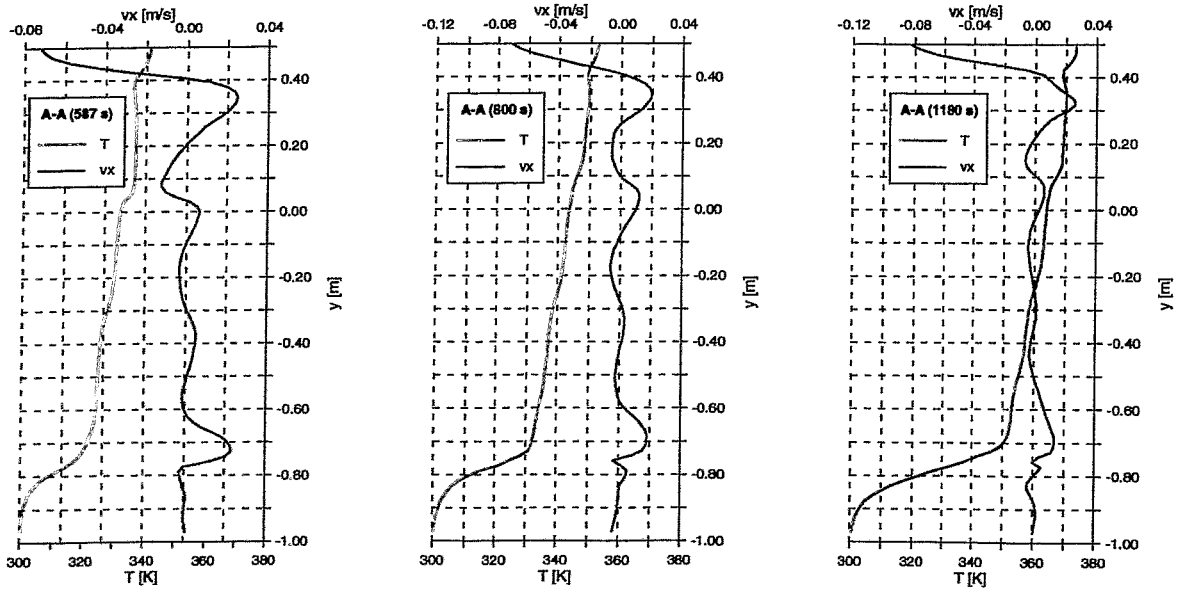


Fig. 4: Temperatures and horizontal velocities vx along the line A-A (x = -0.20 m)

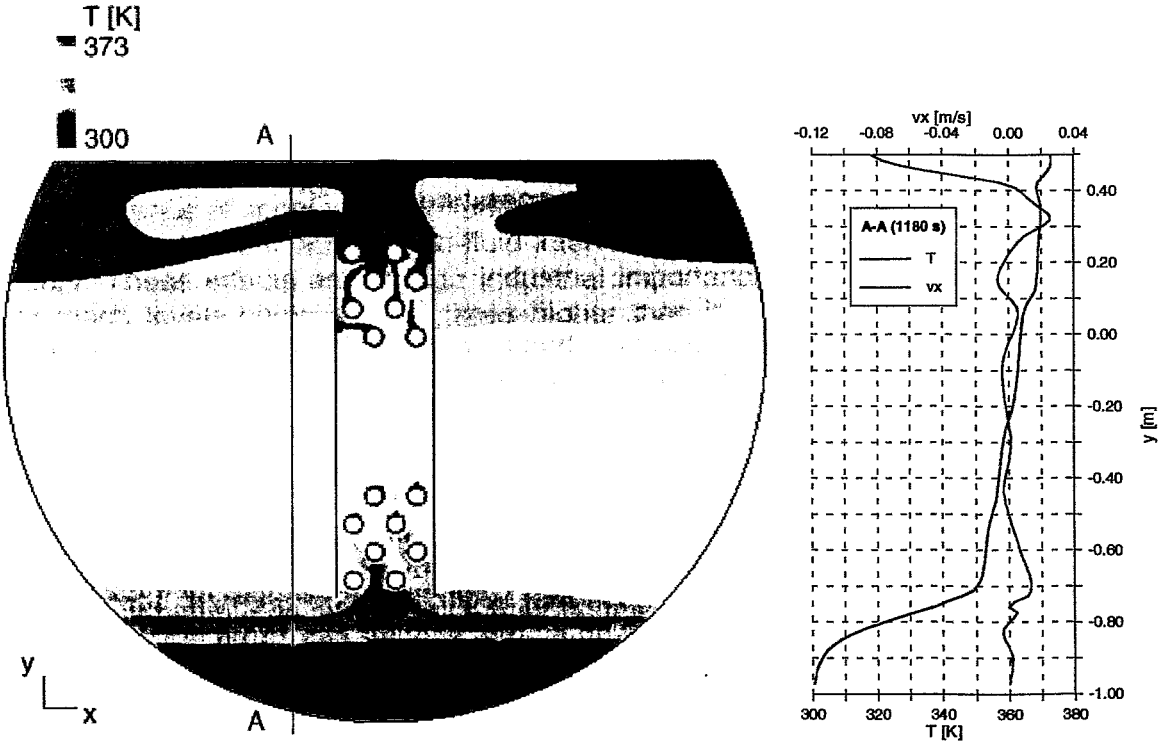


Fig. 5: Temperature field after 1180 seconds and profiles of temperature and hori - zontal velocity vx along the line A-A (x = -0.20 m)

The velocity field after 400 seconds is shown in Figure 3. The fluid heated by the tubes rises quite fast and moves chaotically. In the larger volume outside the bundle and the baffle plates the fluid sinks slowly. The velocity field in Fig. 3 and the velocity profiles in Fig. 3 to Fig. 5 show, that the horizontal velocity component vx alternates its direction with the height y. Therefore the downward fluid velocity in the volume beside the bundle is much slower, than the upward velocity between the tubes.

The water sucked by the boundle glides over the significant colder and therefore more dense water in the dead volume without entraining water from there. Therefore, a considerable temperature gradient is observed near the dead volume (see the temperature profiles in Fig. 3 to Fig. 5). The further development of the temperature distribution is shown in the pictures of Figure 4. The situation in the dead volume stabilizes, because the fluid above is warming up and the density difference grows. These results correspond to experiences from investigations of externally heated tanks [3].

Figure 5 shows the temperature distribution after 1180 seconds. At this time at the surface the water reaches boiling temperature. In the region of natural circulation the temperature decreases by about 20 degrees. The temperature of the dead volume is about 50 degrees lower. The temperature gradient reaches about 500 K/m.

A quantitative comparison of experimental results and calculations is a task for the next investigations. A rough evaluation of the experiments exhibits that a temperature distribution established, which qualitatively corresponds to the calculated situation. At an experiment with a primary pressure of 1 MPa and a subcooled secondary side (heating power about 900 kW) after a heating period of three hours a temperature above the boundle of 97 °C was found. A temperature difference in the region of the predicted circulation was at this time about 15 K. A thermocouple near the position T20 (see Figure 1) showed the initial temperature of 20 °C.

## 4. Conclusions

The basic phenomena during the single phase natural circulation could be clarified. Further investigations are necessary and should be directed to

- consideration of turbulence models
- verification by comparison with measured results
- consideration of two phase flow. The occurrence of steam will enhance the natural circulation and improve the mixing (see [3])
- modelling of the three dimensional case.

It was shown, that a significant temperature stratification has to be expected. This will lead to a faster increase of the temperature in the upper part of the container and therefore of the secondary pressure.

## References


[1] A. Schaffrath, H. Jaegers, E. F. Hicken
NOKO - Versuchsprogramm und erste Ergebnisse
Jahrestagung Kerntechnik 1996, pp. 294-297

[2] A. Schaffrath
Experimentelle und analytische Untersuchungen zur Wirksamkeit des Notkondensators des SWR600/1000,
Dissertation, Bochum 1996

[3] A. Aszódi:
Simulation der transienten Naturkonvektion in einem seitlich beheizten Behälter
Jahrestagung Kerntechnik 1996, pp. 106-109

# INSTABILITIES AT FLUID-FLUID INTERFACES IN THE PRESENCE OF CHEMICAL REACTIONS

**A. Grahn**

## 1. Introduction

The occurrence of spontaneous interfacial convection and turbulence accompanying mass or heat transfer across fluid-fluid interfaces has been known for about half a century. These effects are of high industrial importance since mass transfer rates may reach levels being several times higher than in pure diffusion. Two different mechanisms are supposed to be the cause for the instabilities:

*Convection driven by interfacial tension gradients (Marangoni-Instability).* Interfacial tension in ternary systems depends on the temperature as well as on the interfacial concentration of the solute being transferred between two mutually immiscible phases. Fluctuations of temperature and concentration along the interface lead consequently to interfacial tension gradients. Under critical conditions, i.e. in situations where forces resulting from interfacial tension gradients exceed the viscous forces, macroscopic movement of the fluid arises. The first major theoretical contribution to this type of interfacial instabilities came from Sternling and Scriven [1]. A later important work is that by Reichenbach and Linde [2]. Experimental studies were proceeded by Linde *et al.* [3] and Orell and Westwater [4].

*Convection driven by buoyancy forces (Rayleigh-Taylor Instability).* Density, like interfacial tension, is a function of temperature and solute concentration. The phase change of a solute normally alters the densities of the fluid layers adjacent to the interface and unstable fluid stratifications may occur.

The influence of chemical reactions on hydrodynamic stability of fluid interfaces is twofold since they can either raise or lower the system's stability. In the case of exothermic chemical reactions, the release of heat produces steeper temperature gradients or unstable density stratifications being the cause for Marangoni- or Rayleigh-Taylor-Instability, respectively. On the other hand, the consumption of surface active substances in the course of a chemical reaction at the interface can largely reduce the tendency towards instability. Interfacial turbulence in a gas-liquid system with chemical reaction was experimentally investigated by Thomas and Nicoll [5]. Various papers are devoted to the theoretical approach, such as Sanfeld and Steinchen [6], Dalle Vedove, Bisch, Sanfeld [7], Buyevich, Rabinovich, Vyazmin [8, 9], to name but a few. All the papers investigate solutal effects, thus leaving a gap for experimental and theoretical work accounting for thermal effects on hydrodynamic stability.

## 2. Experimentals

Experiments were carried out in a capillary gap of 2 mm width (Fig.1). It was made of two 100 mm x 80 mm glass plates of 2 mm thickness. Glass stripes kept the distance between the walls.
The transport processes within the fluid were visualized by means of the shadowgraph technique. Pictures were taken with a video camera.

The use of a two-dimensional geometry offers several advantages. First of all, the transport processes are nearly two-dimensional in x/y and hence easy to access by optical experimental procedures. Also, the short extension of the interface in the z-direction suppresses its curvature. In addition, this geometry allows to derive simpler theoretical models, for, under low Reynolds number conditions, the convection terms in the momentum equations become negligible.

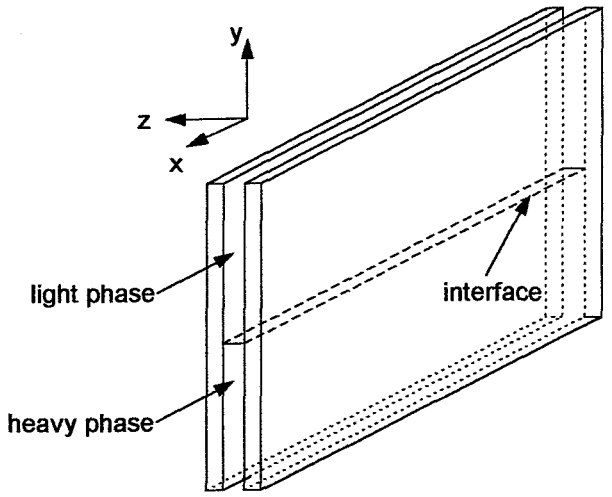


Fig. 1: Capillary gap geometry

Various systems were observed for interfacial activity, systems with transport of surface active substances across the interface as well as systems with subsequent interfacial chemical reaction, the former group being represented here by the system i-pentanol and 2% sodium-laurylsulfate vs. water, the latter by the hydrolysis and esterification of acetylchloride. Prior to the preparation of the different solutions, the two solvents used for the two-phase system were mutually saturated in order to exclude the transport of matter other than the desired one. Table 1 summarizes the observed systems.

## 3. Observations and discussion

Interfacial motion induced by the transfer of a surface active substance is depicted in Fig. 2. The arrow represents the direction of the transfer of sodium-laurylsulfat from the organic to the water phase. The roll cell pattern is established immediately after the two phases have been brought into contact and lasts about 30 s. The intensity of motion decays while single roll cells merge into larger ones. The fluid interface responds to the difference in the interfacial tension, which is due to local adsorption of the surface active agent, by interfacial convection from areas of lower tension to areas of higher tension, inducing motion of the fluid on both sides of the interface through the related shear stress. If a single wavelength of perturbation is amplified, regular roll cells arise. The process is terminated by saturation of the interface with the surface active substance.

Table 1: Observed systems

| light phase | heavy phase | reaction |
|---|---|---|
| i-pentanol / Na-laurylsulfate | water | – |
| cyclohexane / acetylchloride | water | hydrolysis[1)] |
| water | bromocyclohexane/ acetylchloride | hydrolysis[1)] |
| cyclohexane / acetylchloride | ethylenglycol | esterification[2)] |
| ethylenglycol | bromocyclohexane/ acetylchloride | esterification[2)] |

1) Hydrolysis of acetylchloride, $\Delta_R H = -92 kJ/mol$

$$CH_3\text{-}COCl + H_2O \longrightarrow CH_3\text{-}COOH + HCl$$

2) Esterification of acetylchloride and ethylenglycol, $\Delta_R H = -68 kJ/mol$

$$CH_3\text{-}COCl + 0{,}5\ HOCH_2\text{-}CH_2OH \longrightarrow 0{,}5\ CH_3\text{-}C(=O)\text{-}O\text{-}CH_2\text{-}CH_2\text{-}O\text{-}C(=O)\text{-}CH_3 + HCl$$

(1,2-ethyldiethanoate)

The system cyclohexane/acetylchloride vs. water (Fig. 3) shows the instability of the Rayleigh-Taylor type. The density of the fluid above the interface diminishes, while acetylchloride is entering the water phase, thus producing an unstable density stratification in the upper organic phase. The hydrolysis of acetylchloride yields acetic acid and hydrochloric acid. Both substances raise the density of the aqueous phase. Again, the density stratification becomes unstable. The situation is clearly supercritical. In both phases, convection plumes are visible.

In the system water vs. bromocyclohexane/acetylchloride, (Fig. 4) the organic and the water phases were turned over by using an organic solvent heavier than water. The density of the solution of acetylchloride in bromocyclohexane is lower than of the pure solvent. Thus, transferring of acetylchloride from the lower organic to the upper aqueous phase yields an unstable density stratification in the organic phase. The upper phase, however, remains stable, because the acetic and hydrochloric acids make the aqueous solution heavier than the pure water above. Convection is visible only in the lower, organic phase.

Another interesting system is the system cyclohexane/acetylchloride vs. ethylenglycol (Fig. 5). The composition and the unstable density stratification of the upper phase is identical to the system cyclohexane/acetylchloride vs. water. The situation in the lower phase, however, is different. The esterification yields an ester (1,2-ethyldiethanoate), whose density is about the same as that of ethylenglycol, and hydrochloric acid, whose solution in ethylenglycol has a higher density than the pure ethylenglycol. The "fingers" descending from the interface into the ethylenglycol phase are probably due to double-diffusive effects. Double diffusion arises when two transport processes, e.g. transport of matter and heat, with different diffusion coefficients take place at the same time.

The last system under consideration here was prepared again by inverting the two involved phases (Fig. 6). The lower phase consists of bromocyclohexane and acetylchloride, the upper phase of ethylenglycol. Only the lower phase exhibits some weak convection, whereas the upper phase remains quiet.

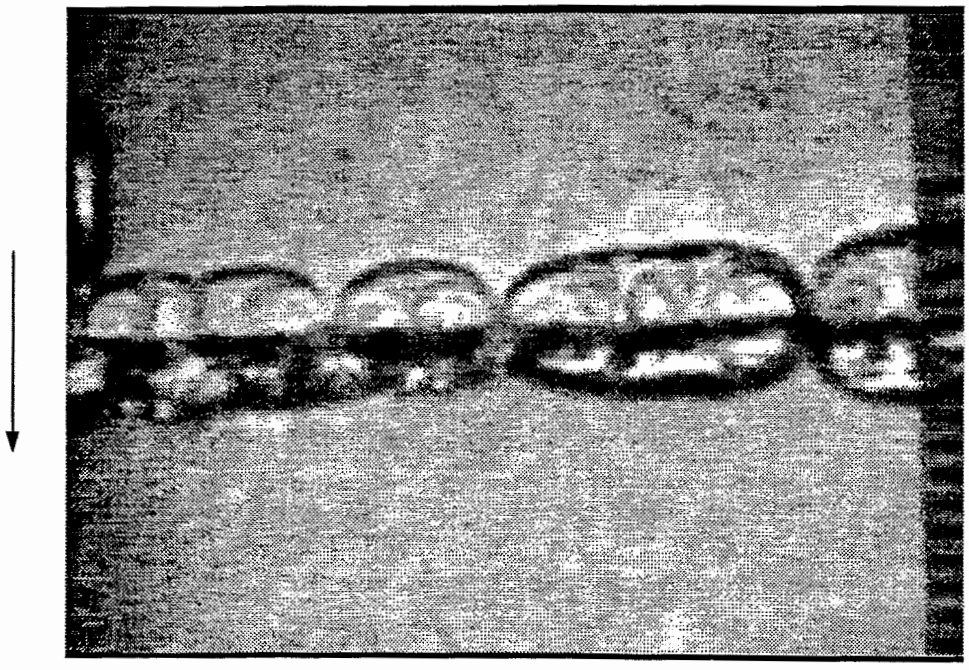

Fig. 2: 2% Na-laurylsulfate/ i-pentanol (upper phase) vs. water (lower phase). Arrow indicates direction of mass transfer.

Fig. 3: 1M acetylchloride/ cyclohexane (upper phase) vs. water (lower phase)

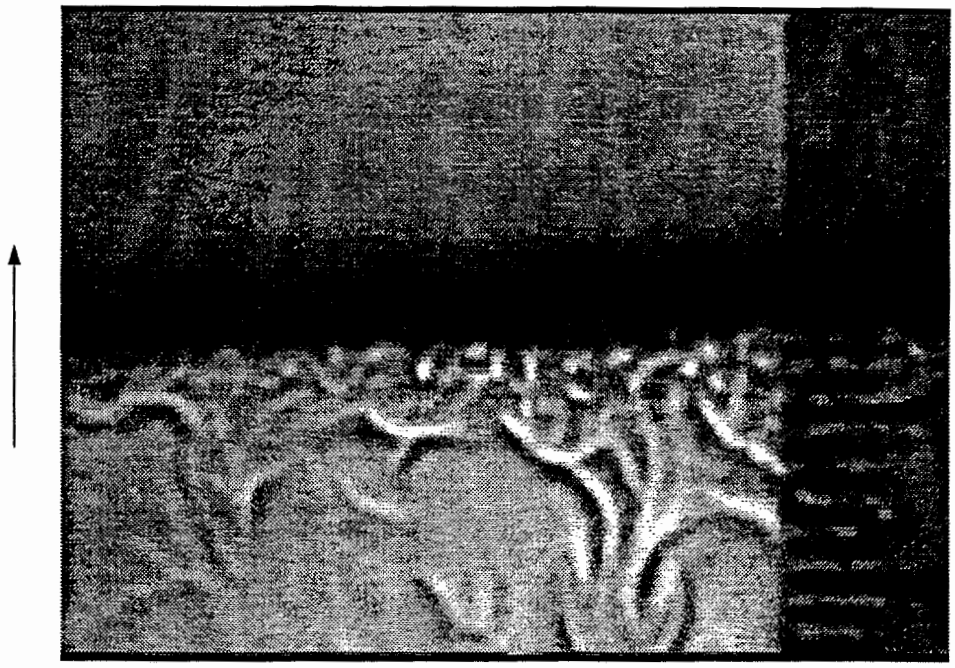

Fig. 4: Water (upper phase) vs. 1M acetylchloride/ bromocyclohexane (lower phase)

Fig. 5: 1M acetylchloride/ cyclohexane (upper phase) vs. ethylenglycol (lower phase)

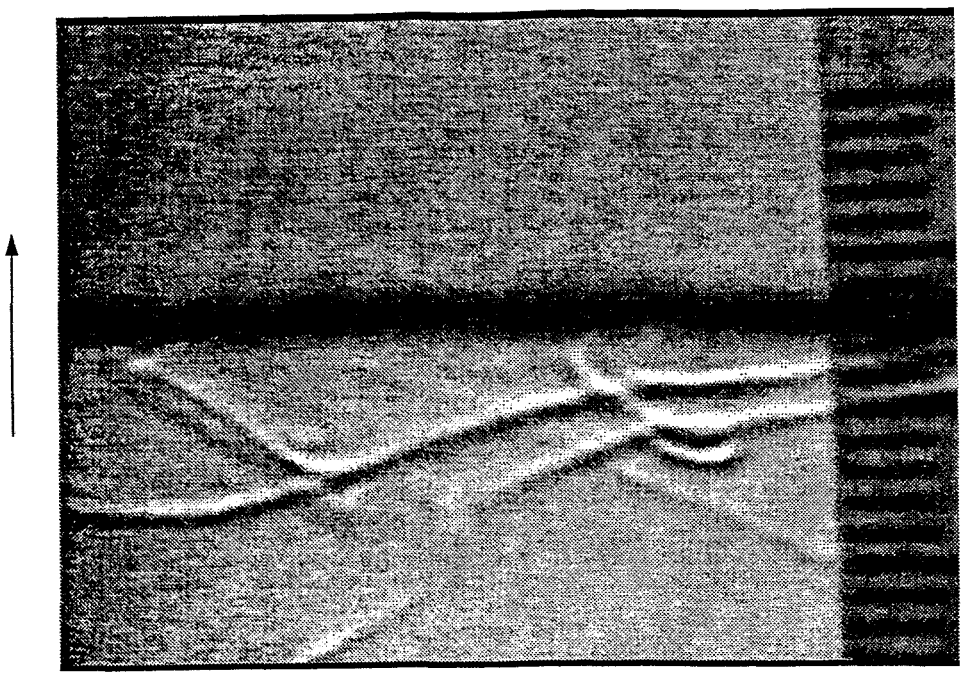

Fig. 6: Ethylenglycol (upper phase) vs. 1M acetylchloride/ bromocyclohexane (lower phase)

## 4. Conclusions

Interfacial instabilities in non-equilibrium two-phase fluid systems show a great variety of convective structures. Those structures can assume ordered stationary or travelling patterns as well as spatial chaos. The driving forces for the two mechanisms involved, Marangoni- and Rayleigh-Taylor instability, are heat- and /or mass-transfer and /or chemical reactions at the fluid interface. Theoretical models that claim for universality should account for these influences.

On the experimental stage further investigation will concentrate on the influence of chemical kinetics on the formation of convective structures as well as the separation of surface tension driven and buoyancy driven instabilities.

## References


[1] Sternling, C.V., Scriven, L.E. (1959). Interfacial Turbulence: Hydrodynamic Instability and the Marangoni Effect. *AIChE Journal*, Vol. 5, p. 514.

[2] Reichenbach, J., Linde, H. (1981). Linear Perturbation Analysis of Surface-Tension-Driven Convection at a Plane Interface (Marangoni Instability). *Journal of Colloid and Interface Science*, Vol. 84, No. 2, p. 433.

[3] Linde, H. (1958). Untersuchungen über den Stoffübergang. *Fette Seifen, Anstrichmittel*, Vol. 60, No.11, p.1053.

[4] Orell, A., Westwater, J.W. (1962). Spontaneous Interfacial Cellular Convection Accompanying Mass Transfer: Ethylene Glycol-Acetic Acid-Ethyl Acetate. *AIChE Journal*, Vol. 8, No. 3, p. 350.

[5] Thomas, W.J., Nicholl E. McK. (1969). Interfacial Turbulence Accompanying Absorption with Reaction. *Trans. Instn Chem. Engrs*, Vol. 47, p. T325.

[6] Sanfeld, A., Steinchen, A. (1984). Motion Induced by Surface-chemical and Electrochemical Kinetics. *Faraday Discuss. Chem.* Soc., 77, p. 169.

[7] Dalle Vedove, W., Bisch, P.M., Sanfeld, A.(1979). Interfacial Hydrodynamic Instability Induced by Surface Chemical Reactions. *J. Non-Equilib Thermodyn.*, Vol. 5, p.35.

[8] Buyevich, Yu.A., Rabinovich, L.M., Vyazmin, A.V. (1993). Chemo-Marangoni Convection I & II. *Journal of Colloid and Interface Science*, Vol. 157, p. 202., p. 211.

[9] Rabinovich, L.M., Vyazmin, A.V., Buyevich, Yu.A. (1995). Chemo-Marangoni Convection I. Linear Analysis and Criteria of Instability. *Journal of Colloid and Interface Science*, Vol. 173, p. 1.

# A NEW ELECTRODE-MESH TOMOGRAPH FOR GAS-LIQUID FLOWS

H.-M. Prasser, A. Böttger, J. Zschau

## 1. Introduction

The electrode-mesh tomograph was developed for the high-speed visualisation of transient gas fraction distributions in two-phase flows in pipes. It is based on the measurement of the local instantaneous conductivity of the two-phase mixture. The time resolution of the device is 1024 frames per second. The sensor consists of two electrode grids with 16 electrodes each. This results in 16 x 16 sensitive points, which are equally distributed over the cross section. The sensor is available in two designs: (1) wire-mesh sensor for lab applications and (2) sensor with enforced electrode rods for high mechanical loads. The device was recently applied to visualise cavitation in a pipeline behind a fast acting valve.

## 2. Working principle of electrode-mesh device

The sensor consists of two planes of electrode grids, which are placed into the flow in a short distance from each other (Fig. 1). The angle between the electrodes of both grids is 90 deg. The electrodes of the first plane (transmitter plane) are supplied with pulses of a driving voltage. If the pulse, given to one of the transmitter electrodes, arrives at a certain wire of the second plane (receiver plane), it is assumed that the crossing point between the two selected wires is occupied by the conducting phase (water). During the measuring cycle, the transmitter electrodes are activated by a multiplex circuit in a successive order. In the simplified four-electrode system of Fig. 1, this is done by closing one of the switches S1 - S4. The data acquisition for the imaging is performed by the evaluation of the analogue current signals from the receiver electrodes. The currents are transformed into voltages by operational amplifiers and sampled by individual sample/hold circuits. After an analogue/digital conversion the signals are recorded by a data acquisition computer and stored for each receiver electrode separately. This procedure is repeated for all transmitter electrodes. In this way the distribution of the electrical conductivity over the cross section occupied by the sensor is obtained row by row. After the last transmitter electrode has been activated, a two-dimensional matrix of values of current is completed that reflects the conductivities between all crossing points of the electrodes of the two perpendicular planes.

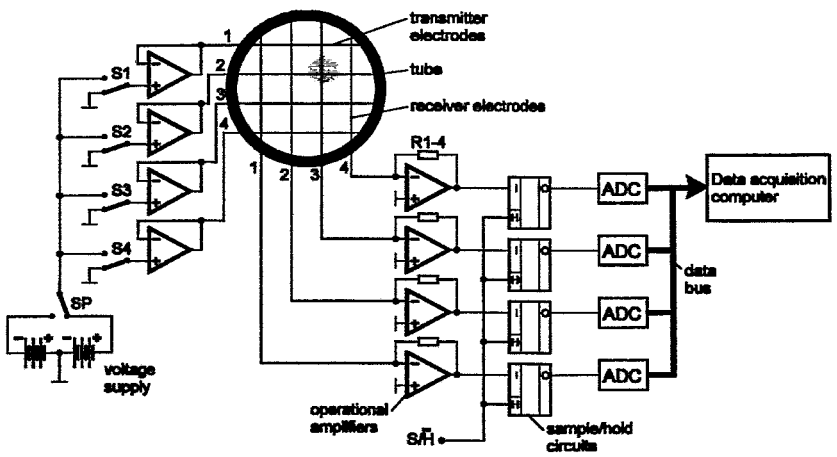


Fig. 1 Simplified scheme of the electrode-mesh device

During a calibration procedure, measurements for the situations "tube completely filled with liquid" and "tube completely filled with gas" are performed and the resulting matrices of conductivity distributions are stored. The matrices acquired during the measuring of the two-phase flow are transformed into distributions of the void fraction by relating the individual measured components to the calibration values.

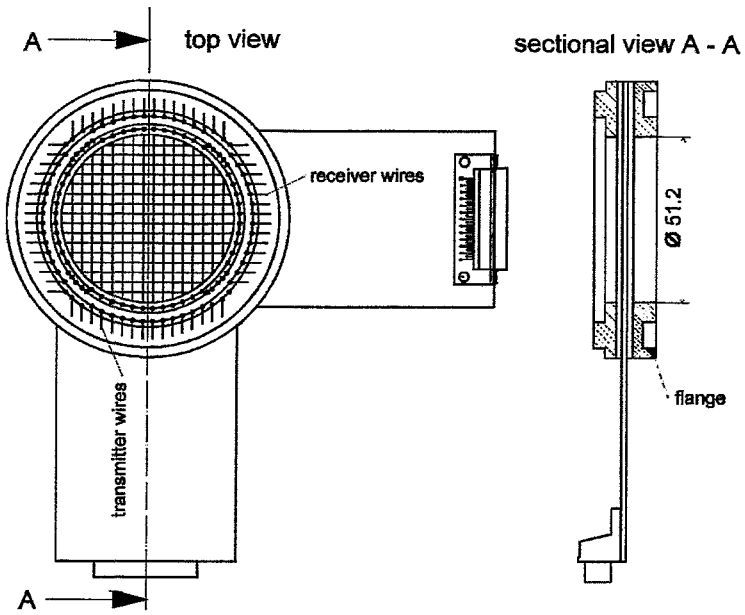


Fig. 2 Wire-mesh sensor for lab applications

The data acquisition unit allows operating in direct mode (on-line) and in memory mode (off-line). The mentioned high imaging rate of 1024 Hz is achieved in the memory mode. The capacity of the memory allows to capture a sequence of 30 s. This can be increased to 60 s by compressing the data.

In the on-line mode several samples of images (taken at 1024 Hz) are averaged and displayed immediately after capturing. The number of frames per second is limited to 20 by the capacity of the interface between the data acquisition unit and the PC.

## 3. Sensor design

Two types of sensors have been developed: the first sensor consists of two planes of wire grids with 16 wires of a diameter of 0.12 mm each (Fig. 2). The wires are equally distributed over the diameter. The distance between the two planes is 1.5 mm. In total the sensor disposes of 16 x 16 = 256 cross points.

Due to the limited mechanical stability of the thin wires a second type of sensor was developed. It is built of metallic rods of stainless steel instead of the wires. The rods have lentil shaped cross sections to avoid high hydraulic resistance (Fig. 3, see also cover sheet).

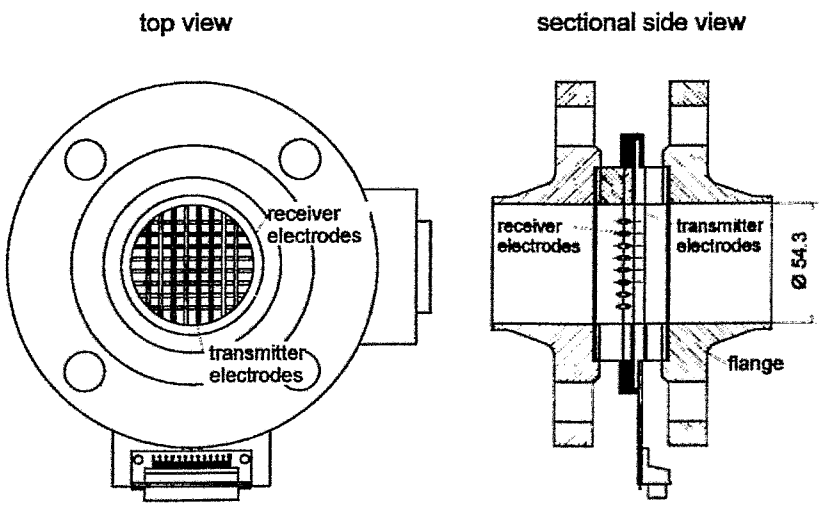


Fig. 3 Heavy electrode-mesh sensor for experiments with high mechanical loads

This sensor can be applied in situations where large mechanical loads have to be expected. It was manufactured in two versions: with 8 (8 x 8 = 64 cross points, nominal diameter 50 mm) and with 16 (256 cross points, nominal diameter 100 mm) electrodes in each plane. The maximum fluid pressure is 7 MPa at a temperature up to 80 °C. A sensor for high pressure and temperature (nuclear reactor conditions, 16 MPa / 350 °C) is under development.

## 4. Visualisation of cavitation in horizontal pipelines

The first application of the sensor was the visualisation of cavitation behind a fast acting valve in a pipeline at a test facility of the Institut für Umwelt- und Sicherheitstechnik (UMSICHT) in Oberhausen, Germany. The pipeline is 100 m long and the experiments were carried out at room temperature and at water velocities of 1 - 4 m/s. The valve was closed in the period from 0 to 200 ms after the start of the experiment. A heavy sensor with 16 x 16 sensitive points (see cover sheet) was placed 0.2 m behind the valve. In another experiment, the same sensor was moved to the position 1.5 m behind the valve. Several tests have proved a very good reproducibility of the results, so that the void fraction distributions of both sensor positions can be directly compared to each other. The captured data can be visualised as a slow motion picture at the computer screen. The axial void fraction distribution over the diameter of the pipeline was extracted from the measured data (see Fig. 4).

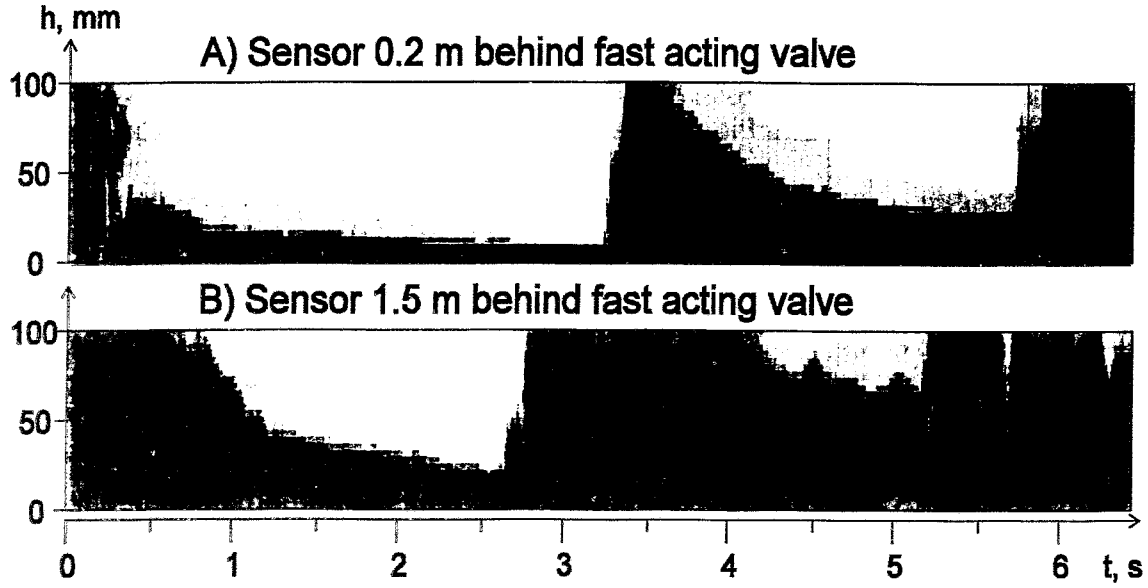


Fig. 4 Axial void fraction distribution as a function of time during the cavitation experiment at UMSICHT Oberhausen, water velocity: 4 m/s

At t=100 ms, i.e. already when the closing of the valve is completed only by approximately 50 %, the cavitation bubble appears at the first sensor position. Later, it reaches the second position, too. It is clearly visible that stratification occurs. The final water level is different at the two measuring positions, it increases with growing distance from the valve. Bubbles are only observed during the process of evaporation when cavitation starts. The void collapse happens in the reverse order. The slug of water

reaches the second sensor position first. Behind the front of water, there are several void plugs. When the bubble has been condensed completely, i.e. at approximately t=3.3 s, a water hammer with pressure peaks of about 4 - 5 MPa takes place. The reflection of the pressure wave causes the generation of a second cavitation bubble. This process is repeated several times. Selected instantaneous gas fraction distributions are plotted in Fig. 5. The evaporation process always starts at the left side of the cross section, an effect caused by the eccentricity of the applied valve.

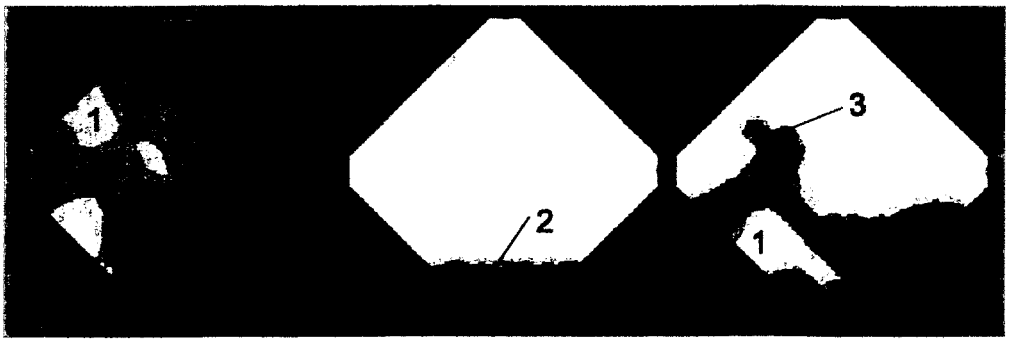


A) t=107 ms B) t=1000 ms C) t=3165 ms

Fig. 5 Plots of the instantaneous gas fraction distribution within the pipeline 0.2 m behind the valve, view towards the valve

A) start of cavitation, B) fully developed stratification, C) start of void collapse

1 - steam bubble, 2 - water level, 3 - droplet

It is worth remarking that similar experiments were carried out with and without the sensor. It was found that the presence of the sensor does not influence neither the amplitude nor the period of the pressure peaks. This indicates that the measures taken to reduce the hydraulic resistance of the device sufficiently prevent an influence on the flow.

## 5. Conclusion

The developed device provides gas fraction distributions with a high resolution in space and time. It is suitable for studies of transient two-phase flows, as well as for the instrumentation of industrial plants. The so-called heavy sensor has proved to withstand the mechanical loads during water hammer experiments. It has delivered a high-speed visualisation of the cavitation bubbles behind a fast acting valve in a pipeline.

Further work aims at the calibration of the device for the case of disperse flow, i.e. when the diameter of the bubbles is less than the electrode pitch. It is also planned to increase then time resolution by improving the electronic circuitry and the spatial resolution by increasing the number of electrodes. Further, the installation of a third electrode grid will be tested for the measurement of the velocity of the individual gas particles. The main field of application of the sensor will be the investigation of transient flow maps. For this purpose, the sensor will be installed in a two-phase test rig in Rossendorf in the near future.

# NANOSCALE PRECIPITATES IN RUSSIAN REACTOR PRESSURE VESSEL STEEL AFTER IRRADIATION AND ANNEALING

**J.Böhmert, M.Grosse, P.Nitsche**

## 1. Introduction

The microstructural evolution of the reactor pressure vessel (RPV) steel effected by neutron irradiation is not yet completely understood. This particularly concerns the Russian RPV steel where considerably fewer results are available.

A working group at the Institute for Safety Research has undertaken a comprehensive investigation of the irradiation-induced microstructural evolution in this type of steel. In a preceding paper [1] recent results obtained by anomalous small angle X-ray scattering were already presented. The following study presents the results of small angle neutron scattering (SANS) experiments.

## 2. SANS - method

Since the beginning of the eighties SANS has been used to investigate irradiation defects. Cold, hence long wavelength neutrons are diffracted by fluctuations in the scattering density of the matrix as a result of the presence of particles, precipitates, voids etc. in the size range from less than 1 nanometre to approximately 50 nanometres. This is just the same range like the irradiation defects.

Experimental data in the form of differential scattering cross section $d\Sigma/d\Omega$ depend on volume fraction f, structure, composition, size and shape of the scattering particles according to

$$\frac{d\Sigma(Q,\alpha)}{d\Omega} = f(1-f)\left[(\Delta\eta_{nuc})^2+(\Delta\eta_{mag})^2\cdot\sin^2(\alpha)\right]F(Q,h(R),s(Q,R)) \qquad (1)$$

where $\alpha$ is the angle between the scattering vector Q and the magnetization of the sample, $Q=(4\pi/\lambda)\sin\Theta/2$ with the scattering angle $\Theta$ and the neutron wavelength $\lambda$. $\Delta\eta = n_P b_P - n_M b_M$ is the difference of the scattering length density between the particles and the matrix related to the magnetic and the nuclear scattering contribution, respectively. The structure factor function F[Q,h(R),s(Q·R)] describes the form of the SANS curve versus Q and can be interpreted as convolution of a shape-dependent single particle scattering function s(Q·R) of particles with the radius R and a size distribution function h(R) [2].

As known, it is impossible to determine the three-dimensional scattering structure from the measured scattering intensity curve without a-priori information or assumption. However, SANS has some advantages in comparison to SAXS experiments. For instance, if inhomogeneities and matrix differ in the magnetization, SANS permits to calculate the volume fraction by separating magnetic and nuclear scattering. For this

purpose the experiments are performed in a strong homogeneous magnetic field and the scattering intensity is measured perpendicular and parallel to the magnetization. The magnetic scattering contribution disappears in the parallel direction. Additionally, these two independently measured SANS curves provide information about the chemical composition of the scattering centres.

Nevertheless, extracting microstructural data from the measured scattering curves remains a difficult issue. There are some useful approximations to determine the defect size in simple homogeneous systems from the slope of a suitable plot of the scattering cross section versus the scattering vector.

Polydisperse systems need more a sophisticated approach. Often a frequency distribution, e.g. the logarithmic normal distribution in [2], is assumed and so fitted with free-fitting parameters that the calculated and the measured scattering curves correspond. A method which does not depend on a-priori assumptions about the type of the size distribution (only of the shape of them) was given by Glatter [3]. The Glatter method solved numerically the 'inversal scattering problem' for a presupposed partical shape, beginning with an estimate of the maximum particle dimension by trial and error and taking into consideration different impacts of the instrumental conditions.

A qualified analysis of SANS experiments needs

- determination of the scattering cross section in real units by absolute calibration of the scattering data, measurement of both the incident intensity and the attenuation of the sample
- consideration of the background intensity due to diffuse scattering, in particular the monotonic Laue scattering
- measurement of the scattering intensity over a sufficiently extended range.

Instrumental noise and background effects are difficult to eliminate. Therefore, the scattering intensity is mostly related to a reference sample. In the case of irradiation effects it is obvious to take a sample of the unirradiated material. Thus, the difference of the scattering intensity between irradiated and unirradiated state immediately provides the microstructural information on the irradiation-induced defects. Unfortunately, the procedure is very sensitive to possible systematic errors.

The scattering cross section of the neutrons is very low. Therefore, SANS requires a large sample volume and is an integral method. But for such complicated, hierarchically structurized and heterogeneous systems like RPV steels this is a real advantage.

## 3. Experimental

The materials selected represent two typical VVER 440-type reactor pressure vessel (RPV) steels. The first material (code: KAB) is typical for the first reactor generation VVER 440/230, for instance being used at units 1 - 4 of the Greifswald NPP. It has a quite high content of impurities (copper, phosphorus). The second material (code: PAKS) are surveillance specimens manufactured by Skoda Pilsen for the VVER 440/213 NPP in Paks (Hungary). It is a highly qualified product with low impurity concentration and low susceptibility against neutron embrittlement. In every case both

Table 1: Irradiation conditions ($E_n$ > 1MeV)

| Material | Irradiation temperature [°C] | Neutron flux [$10^{16}$ $m^{-2}s^{-1}$] | Neutron fluence [$10^{23}$ $m^{-2}$] | Reactor |
|---|---|---|---|---|
| KAB-W | 265 | 3.3 | 7.9 | Rheinsberg |
| PAKS-W | 270 | 1.1 | 8.0 | Paks |
| KAB-B | 265 | 3.0 | 7.0 | Rheinsberg |
| PAKS-B | 270 | 1.1 | 14.0 | Paks |

Table 2: Chemical composition of the materials in wt.% (Fe balance)

| Material | C | Mn | Ni | Cr | Mo | V | S | P | Cu |
|---|---|---|---|---|---|---|---|---|---|
| KAB-W | 0.047 | 1.32 | 0.19 | 1.29 | 0.24 | 0.17 | 0.014 | 0.050 | 0.19 |
| PAKS-W | 0.040 | 1.25 | 0.06 | 1.34 | 0.50 | 0.21 | 0.013 | 0.014 | 0.08 |
| KAB-B | 0.138 | 0.52 | 0.23 | 2.62 | 0.60 | 0.28 | 0.013 | 0.011 | 0.23 |
| PAKS-B | 0.160 | 0.54 | 0.07 | 2.70 | 0.68 | 0.28 | 0.018 | 0.014 | 0.09 |

base and weld material (code: B or W, respectively) were investigated. The materials were irradiated under service conditions. Whereas the PAKS material was in the surveillance positions of the VVER 440-type reactors, KAB material was irradiated within a high flux channel of the VVER prototype reactor VVER-2 in Rheinsberg (Germany). Here, the temperature was slightly lower. Unfortunately, the fluence is clearly higher for the PAKS material. Table 1 characterizes the irradiation conditions, Table 2 gives the chemical composition of the materials.

Disks with a thickness of 2 to 3 mm were cut from the specimens. Disks from each material were annealed 1h at 400, 475 and 550°C in an argon atmosphere.

SANS experiments were performed at the KWS2 facility at KFA Jülich (Germany) by using the following experimental condition:

Neutron wavelength: 0.79 nm
sample-detector-distance: 1.19 m
measurement range of scattering vector: 0.2 to 0.8 $nm^{-1}$
magnetic field: 1.5 T, parallel and perpendicular to the scattering plane
detector: 2 crosswise-arranged linear position-sensitive detector.

The size distribution analysis was carried out by the Glatter method.

## 4. Results

Figs. 1 and 2 show the volume distribution (volume of the particles in the corresponding size range) of base and weld metal in the unirradiated state. In every case the distribution function pos- sesses a first maxi- mum near a particle radius of 2 nm. Although thermodynamically quite incomprehensible it is known but hardly investigated as far there are defects of such a low size in complex metallic alloys. A second maximum is at approximately 6 to 8 nm corresponding to a population of fine carbide precipitations, preferentially vanadium carbides, which can be observed by TEM. The size distribution is clearly different for base and weld metal and for both investigated steel types as well. The heats (base and weld) with lower content of impurities (PAKS) show a lower content of fine-dispersed defects in the size range of about 2 nm.

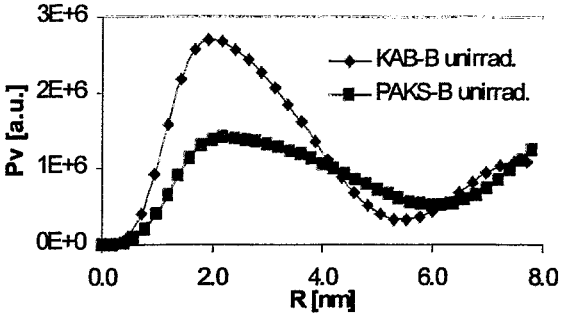


Fig.1: Volume distribution of the investigated base metal in the unirradiated state

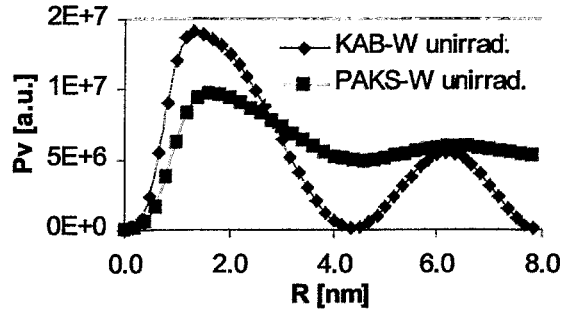


Fig.2: Volume distribution of the investigated weld metal in the unirradiated state

Irradiation influences the magnitude of the distribution curve but not the shape (Figs. 3 and 4). This can clearer be recognized in Figs. 5 and 6. Here, the volume distribution of the irradiation-effected defects or precipitates is depicted and its change by annealing is shown. These distribution curves are characterized by a bimodal course with a high first peak at a radius of 1 to 2 nm. A second maximum is located at 6 to 7 nm, but does not appear in all cases. The first maximum is especially striking for the heats with higher copper content. By annealing, however, the maximum is quickly reduced and almost disappears after 2 h-annealing at 475°C. In addition to the cooper content, the metal- lurgical treatment or the content of other alloy elements seem to be also important as the comparison of base and weld metal of the PAKS material shows where the distribution curve of the weld metal exhibits a high first maximum. In contrast to the annealing response of KAB material the irradiation-

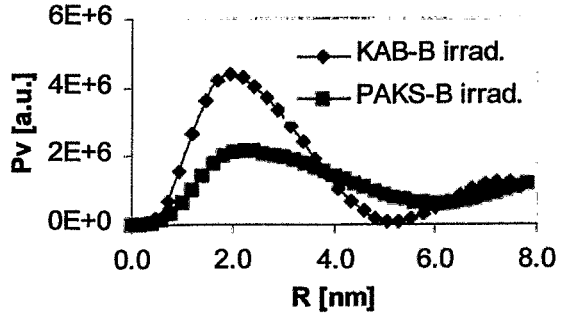


Fig.3: Volume distribution of the investigated base metal in the irradiated state

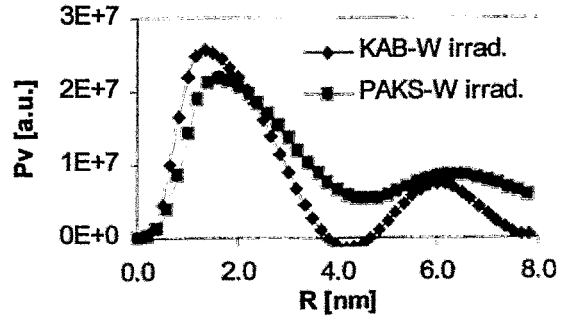


Fig.4: Volume distribution of the investigated weld metal in the irradiated state

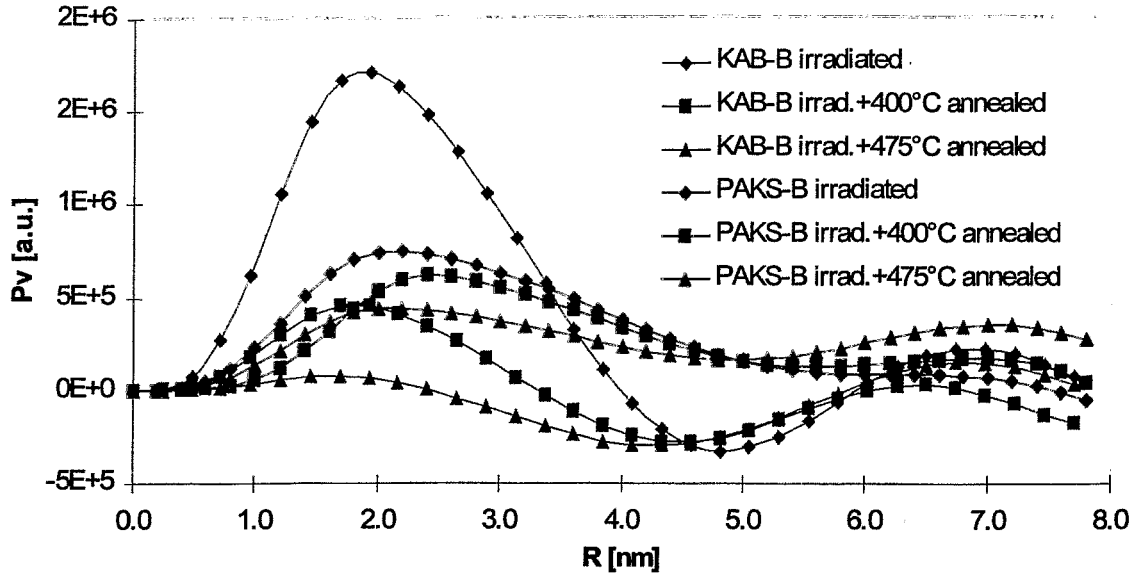


Fig.5: Comparison of the irradiation-induced volume distribution function of irradiation-induced defects for different states of base metal

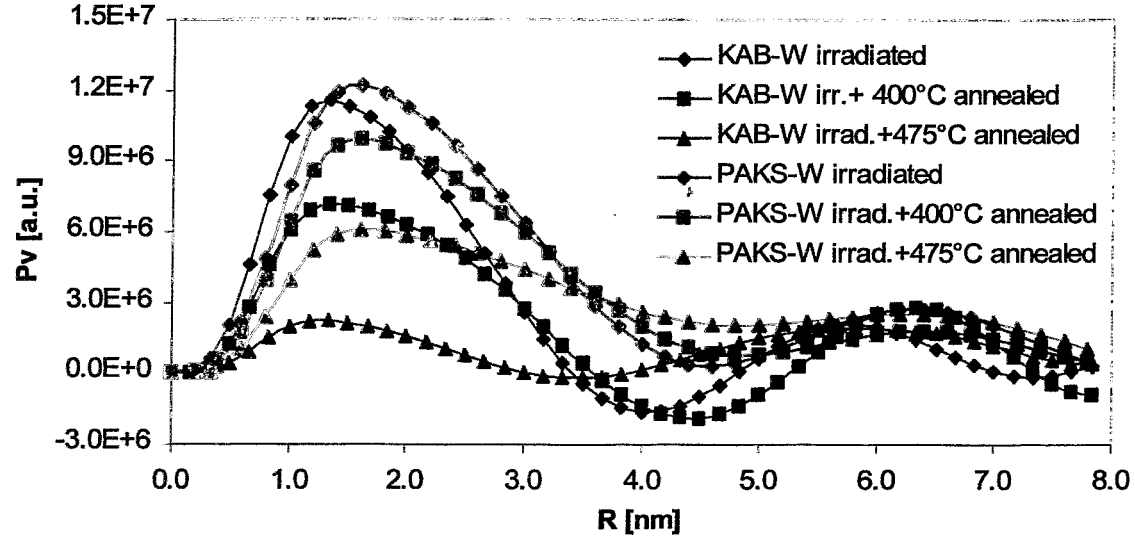


Fig.6: Comparison of the volume distribution of irradiation-induced defects for different states of weld metal

induced fine-dispersed defects only slowly and partly vanish by annealing up to 475°C.

The influence of irradiation and annealing on the distribution curve for bigger radii is considerably less. The PAKS material shows a weak influence of the irradiation, only by annealing at 475°C a volume fraction of the particles from 6 to 7 nm for weld and 6 to 8 nm for base metal increase with the KAB material. The number of particles is reduced within the range from 4 to 5 nm and is enhanced for particle sizes near 7 nm

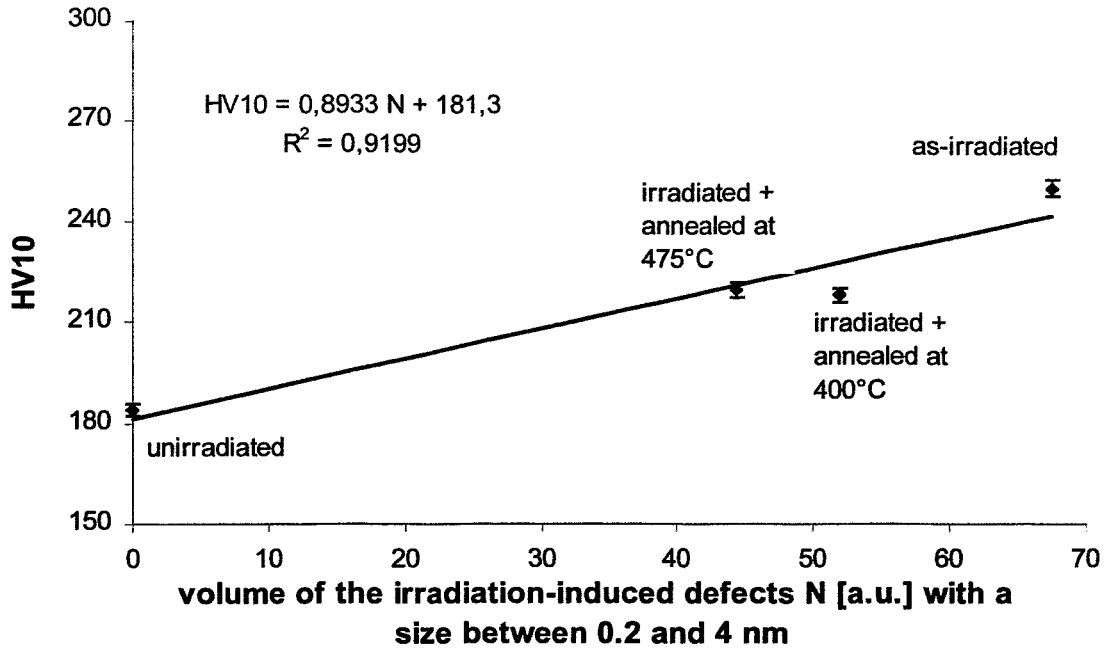


Fig.7: Correlation between hardness HV10 and integral volume of defects for the PAKS-B material

in the KAB material.

The reason of the irradiation hardening seems to be the fine-dispersed defects within the range of the first maximum. Fig. 7 demonstrates the correlation between the hardness HV10 and the integral of the size distribution for sizes from 0.2 to 4 nm at the material PAKS-B as an example. Independent on the treatment there is a reasonable relation.

## 5. Conclusions

As known from TEM investigations Russian RPV steels contain precipitates of different type, form and size. Typically, there are both large Cr-rich mixed carbides of the $M_{23}C_6$ or $M_7C_3$ type and of 0.2 µm diameter, and smaller vanadium carbides of 10 - 20 nm diameter. The latter might correspond to the particles which cause the second maximum of the bimodal size distribution curve obtained by SANS. Besides these known particles another type of structure defect must be supposed. Their amount depends on the steel composition and the metallurgical treatment. High content of copper promotes the occurence of theses defects. Basically, irradiation does not produce a new kind of irradiation defect but enhances the number of the defects that already exist. This is specially valid for the fine-dispersed defects of 1-2 nm in radius. However, the different annealing response of the material KAB and PAKS points to different thermodynamical stability and, hence, to various structure and/or composition of the defects. The structural defects formed in the copper-rich material are not as stable as the slightly larger defects of the copper-poor material.

Conclusions about the defects characterized by the second peak of the distribution curve are rather questionable. For the material PAKS a growth process with the annealing temperature is evident what can be interpreted as consequence of a selective dissolution of the fine-dispersed defects in the range of the first maximum. The results for the material KAB are confusing. Apart from the fact that negative values of the size distribution appear in the range from approximately 4 to 5 nm (this is not basically absurd from the physical point of view) there is no obvious effect of annealing. It cannot be excluded that both the limited measuring range, which is available for the analysis of the scattering curve, and the high first maximum in the case of the irradiated state affect the Glatter method and produce disturbances in the distribution curves which are caused by Fourier analysis. On the other hand, the scattering function measured could be the result of several competitive processes such like dissolution, phase transformation, precipitation from supersaturated solutions or Ostwald ripening.

Nevertheless, these processes are not very relevant regarding the neutron embrittlement. The unambiguous correlation between hardness and the amount of the fine-dispersed defects proves that above all these defects with a size of few nanometers act as dislocation barriers. As the embrittlement of these materials was not connected with a particular embrittlement mechanism, like intergranular brittle fracture for instance, the neutron embrittlement is primarily caused by the irradiation hardening. Consequently, these fine-dispersed defects are just responsible for the neutron embrittlement. From this point of view the microstructural analysis confirms the empirical results well known from the mechanical testing about the influences of copper and the metallurgical treatment as well as about the effect of post-irradiation annealing.

**References**


[1] J.Böhmert and M.Grosse
"Characterization of Irradiation-induced Defect Structures in VVER-type Pressure Vessel Steel 15Cr2MoV by Small Angle X-ray Scattering"
Forschungszentrum Rossendorf, Institute for Safety Research, Annual Report 1993, pp. 21

[2] P.A.Beaven, F.Frisius et. al.
"SANS Investigation of Irradiated A 533-B Steels Doped with Phosporus"
Radiation Embrittlement of Nuclear Reactor Pressure Vessel Steels: An International Review (Third Volume) ASTM STP 1011, L.E.Stehle,Ed., American Society for Testing and Materials, Philadelphia, 1989, pp. 243

[3] O.Glatter
J.Appl.Cryst. 13 (1980), pp. 13

# MEASUREMENT OF CRACK GROWTH BY ULTRASOUND DURING FRACTURE MECHANICS BEND TESTING

**U. Bergmann, F. Bergner[1], J. Böhmert**

## 1. Introduction

Fracture mechanics can describe the behaviour of tough materials by means of crack resistance curves. Their experimental determination requires the measurement of crack growth in dependence on the loading parameters (force, displacement). For the in-situ measurement of the crack growth during the test the electrical potential drop method and, as a more indirect method, the compliance method are applied. In principle, ultrasound (US) should be appropriate for crack growth measurement as well. However, US methods soon do reach their application limits if used for small specimens with cross sections of a few square centimeters. In [1], the appropriateness of a US technique was shown which is based on the measurement of the time of flight of a transverse wave diffracted at the crack tip during a three-point bending test. The measuring arrangement does not only provide the measuring echo pulse, but also a sequence of further echo trains, which cannot simply be identified and which can superimpose the measuring signal with continued bending. Thus, the application of the technique turns out to be difficult.To quality the technique signal processing and evaluation have to be improved.

## 2. US field analysis

The way of the US pulse through the specimen was simulated by the elastodynamic finite integration technique (EFIT) [2]. EFIT numerically calculates the displacement of the nodal points of a two-(or three-)dimensional network due to an incidenting US wave field. In this way the wave propagation and the interaction with defects and surfaces can be simulated including the con-siderati on of mode conversion. A part of the waves reaches the receiving probe and generates the receiver response. The sequence of received pulse amplitudes can also be calculated (A-scan).

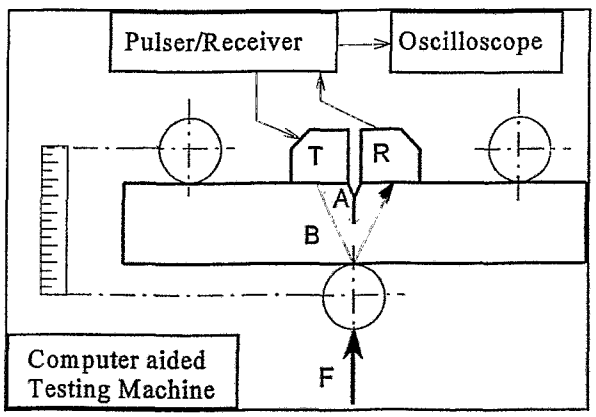


Fig. 1: Experimental situation, A,B - travel paths of tip-diffracted and back-wall reflected echo

Fig. 1 shows the experimental setup. Two 45°-angle beam probes are symmetrically placed on the notched side of the three-point bending specimen. The transmitting probe generates a transverse wave front which is directed to the crack tip. The simulated wave propagation of such an incidenting pulse is represented for 5 successive moments in Fig. 2. The A-scan corresponding to Fig. 2 is shown in Fig. 3 and compared with the measured result. Except the time

[1] Technische Universität Dresden, Institut für Werkstoffwissenschaften

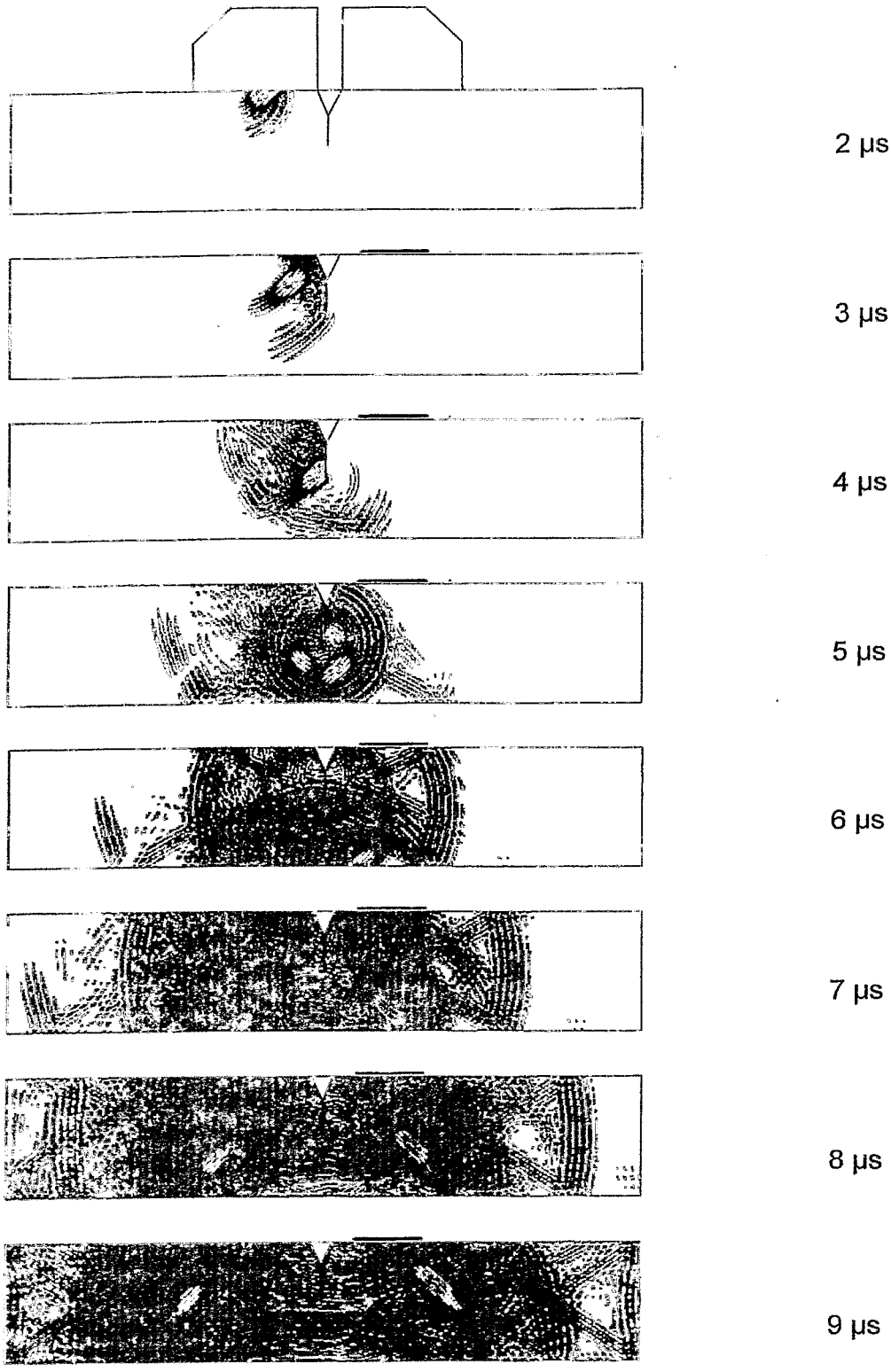


Fig. 2: EFIT simulated wave propagation of a transverse wave through a 3-point bend specimen
Fig. shows snap-shots in intervals of 1 µs

calibration, both A-scans agree. That allows to identify origin and propagation path of the different echos. The first high signal (number 2 in Fig. 3) is the tip-diffracted non-mode converted transverse wave echo, which has already been used as reference signal in [1]. The signals 4 and 5 in Fig. 3 are back-wall reflected. An enlargement of the crack length increases the time of flight (and the amplitude) of echo 2 whereas the arrival time of echo 4 or 5 keeps unchanged (Fig. 4). Thus, the tip-diffracted transverse wave is well appropriate for crack growth measurement. In addition to the crack length, bending of the specimen also changes the A-scan, above all concerning the US waveform. This is because bending changes relative position of the crack tip inside the probe. As the effect of bending reduces the distance between the crack tip-diffracted echo and the following echos the application of US crack growth measurement is limited with regard to the deformation. Basically, the low echo 1 in Fig.3 which results from the mode conversion at the crack tip could be used too. The low level of this echo complicates the measurement. Using further EFIT simulations the best test parameter like specimen geometry, wave mode, angle of incidence, probe positions, and probe characteristic can be selected [3]. The set-up presented here is already the result of such a optimization.

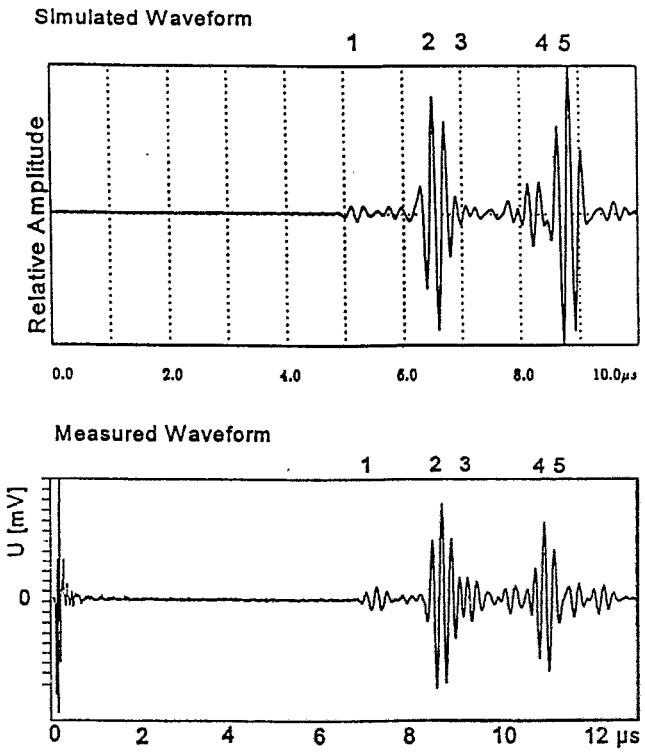


Fig. 3:
Comparison of simulated and measured echo trains for the case of an incidenting transverse wave

1 - transverse wave, tip-diffracted to a longitudinal wave
2 - tip-diffracted transverse wave
3 - backwall-reflected longitudinal wave created by a tip-diffracted transverse wave, mode converted to a longitudinal wave
4 - backwall-reflected longitudinal wave, created by the incidenting and tip-diffracted transverse wave
5 - backwall-reflected transverse wave

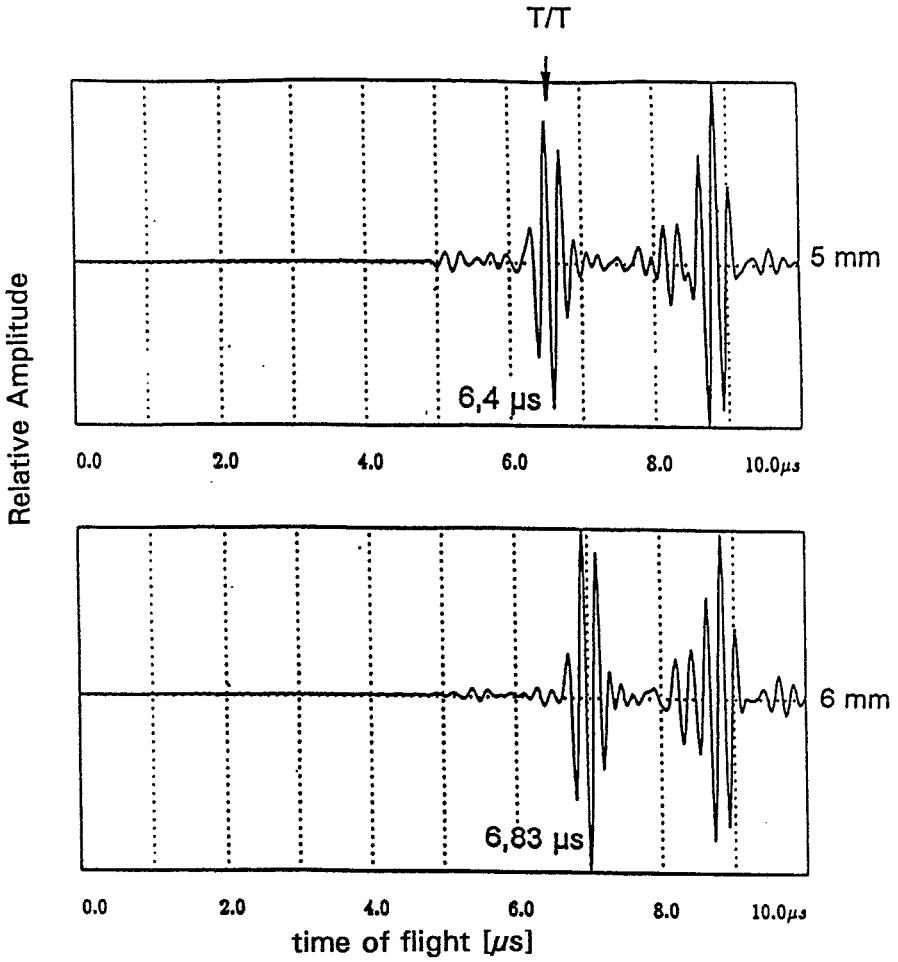


Fig. 4: Comparison of simulated echo trains for 2 different crack lengths of 5 and 6 mm

## 3. Evaluation of time-of-flight measurements

During the bending test the US pulses are transmitted and recorded in regular intervals, for example as each 0.01 mm displacement progress. Thus, a test generates 100 and more echo trains which must be evaluated with regard to the amplitude-time response. Therefore, a new evaluation technique was developed [4]. The height of amplitudes from each A-scan is transformed in a grey level scale so that the highest value is black and the lowest one is white. The one-dimensional sequence of this grey level distribution is plotted versus the specimen displacement (Fig. 5). The result is a clear presentation of the changes of the time of flight in dependence on the increasing displacement. The tangent at the curve represents the instantaneous crack growth rate. The procedure reveals characteristic features like crack opening or crack initiation and helps to follow the course of the reference echo and to discriminate disturbances which do not allow to detect the reference signal in the singular A-scan (Fig. 6). Such disturbances seem to be dependent on the microstructure of the material.

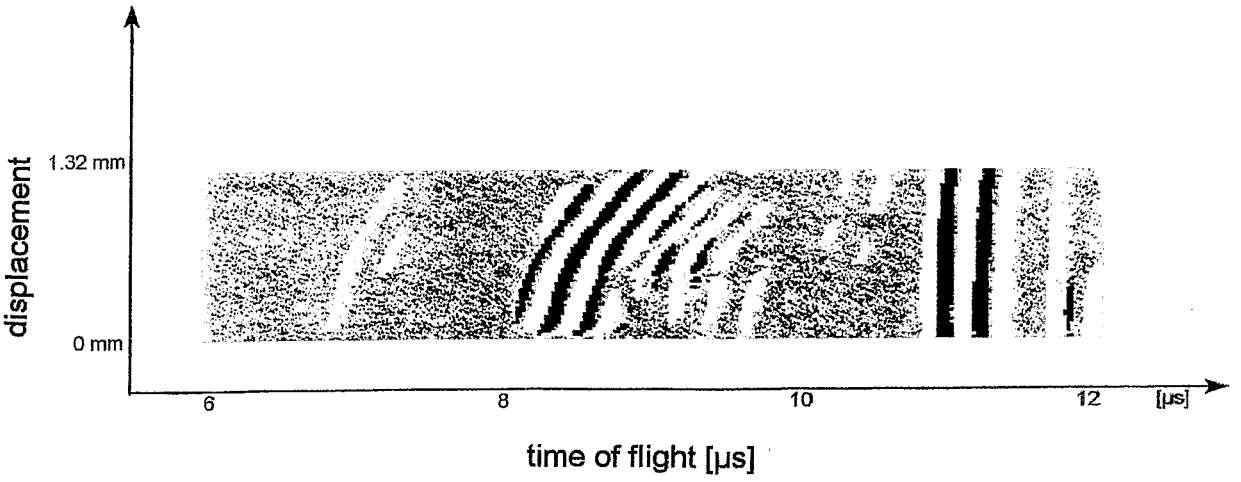


Fig. 5: Visualization of crack propagation during bending test
Measurement with 45° angle beam probe at 10CrMo9.10 steel

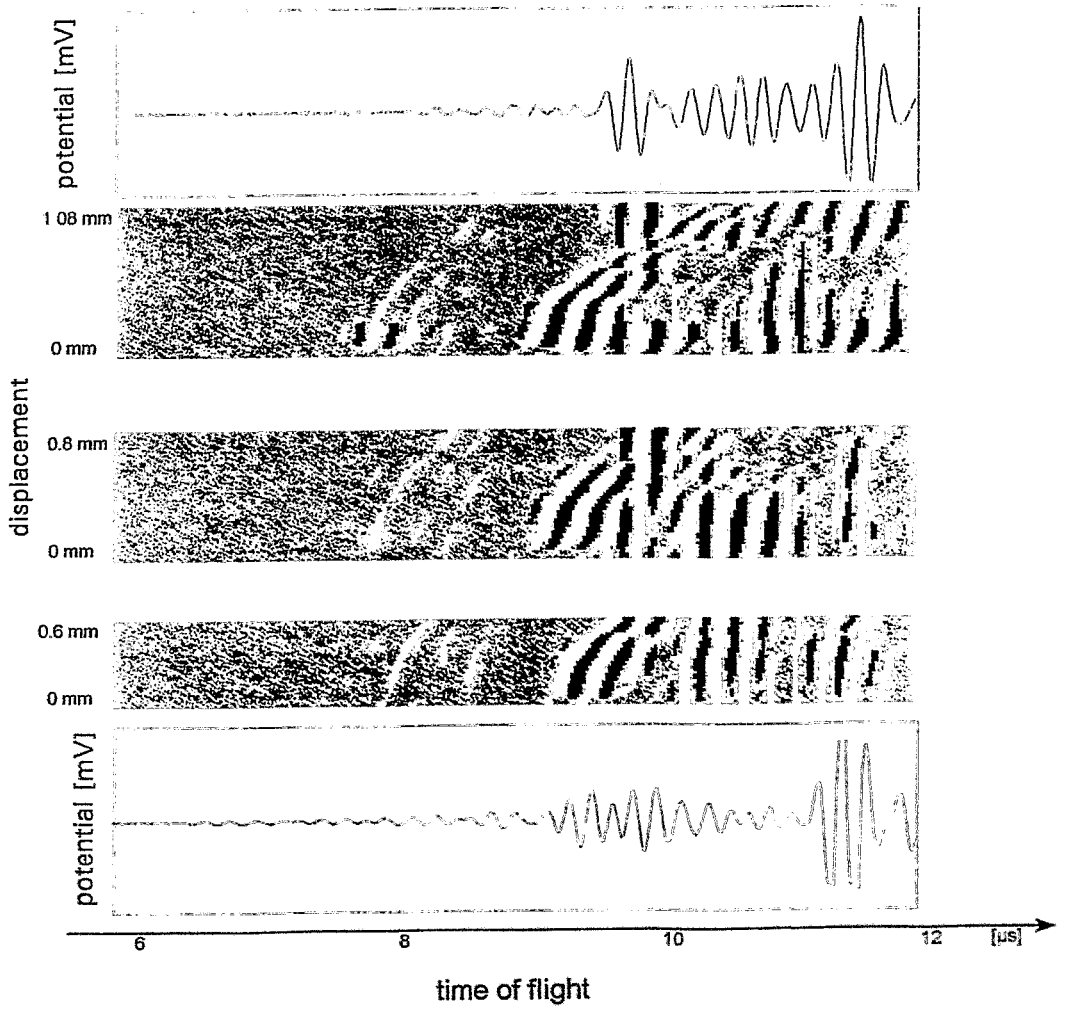


Fig. 6: Visualization of crack propagation during bending test with different displacement
Measurement with 45° angle beam probe at GGG-40

## 4. Verification tests

The technique was tested at specimens from several Fe-based alloys with different strength and toughness properties (Tab. 1). All specimens were machined in Charpy-V geometry (dimension in mm: 10x10x55) and fatigue cracked to an initial crack length of about 5 mm. The bending tests were performed at a computer controlled testing machine TIRAtest2300 with a 3 point bending device in a displacement-controlled mode, which also provides the trigger pulse for the US pulser/receiver 5052PRX. The tests were finished at a preset displacement. Then the specimens were broken and the crack length optically measured.

Table 1: Material for verification tests, mechanical properties

| Material | Heat Treatment | $R_{p0.2}$/MPa | $R_m$/MPa | USE/J |
|---|---|---|---|---|
| 10CrMo9.10 forged | 950 °C/oil 720 °C/2 h air | 450 | 570 | 260 |
| | 600 °C/2 h air | 604 | 740 | 190 |
| St E 460 | as-received | 450 | 643 | 85 |
| 20MnMoNi55 | as-received | 501 | 640 | 200 |
| GGG 40 | as-reiceived | 274 | 395 | 18 |

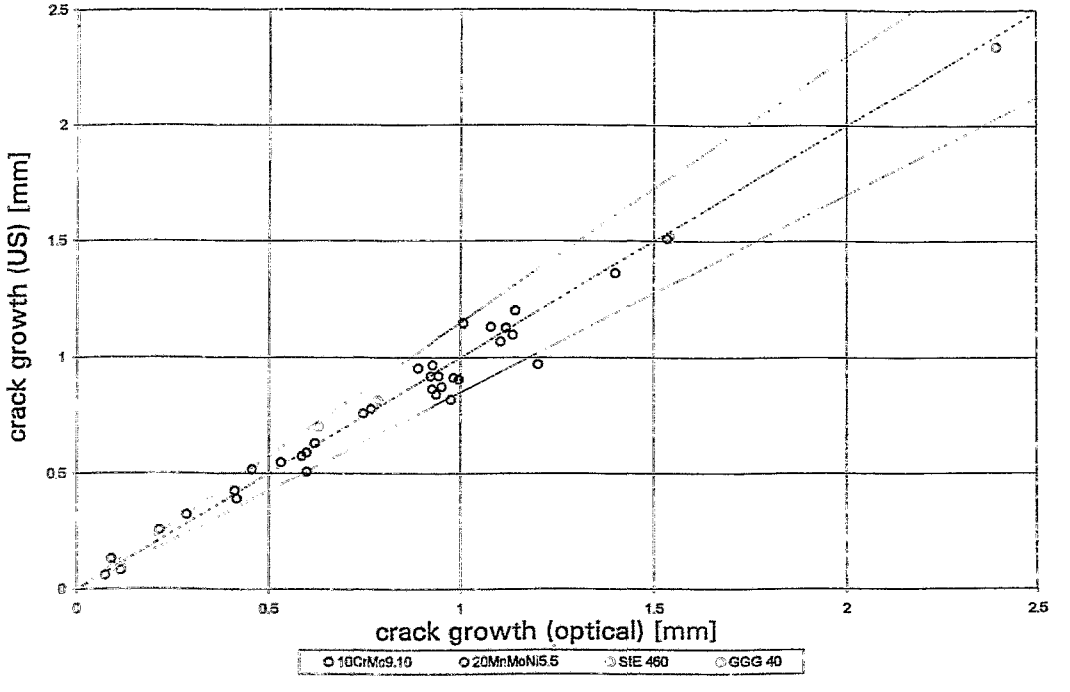


Fig. 7: Comparison of crack growth measured by US and optical method

Fig. 7 shows the comparison of the optically measured crack propagation with the results of the US measurements. Independent on the material type, almost all measuring points lie within a scatter band which defines a permissible deviation of ± 15% according to the standard.

## 5. Conclusions

Stable crack growth in three-points bending tests can be determined by measurement the time of flight of a tip diffracted transverse US wave at specimens with Charpy-V geometry. For iron alloys with different toughness a 15% accuracy criterion can be met. Simulation of the wave propagation using the EFIT code confirms that the accessible range of crack length measurement is limited due to superposition effects. A transformation of the amplitudes of the echo train into grey levels visualizes the changes of the US time of flight versus bending of the specimen and allows to trace the crack propagation with increasing load even for materials with complicated microstructure.

The technique can further be refined. Essential aspects could be:
- Application of the longitudinal wave technique
- Extension the working range to lower and higher temperatures
- Application to dynamic test conditions.

## References


[1] U. Bergmann, J. Böhmert and F. Bergner
"Ultraschallverfahren zur Messung duktilen Rißfortschritts bei quasistatischer Belastung"
DVM-Arbeitskreis Bruchvorgänge, Köln, 1995, S. 177-185

[2] K.J. Langenberg et al.
"Evaluation of materials and structures by quantitative ultrasonics"
Inverse methods and imaging, ed. By J.D. Achenbach, Springer Verlag Wien - New-York, 1993

[3] U. Bergmann
"Mathematisch-numerische Modellierung der Ultraschallstreuung an oberflächenverbundenen Rissen mit dem EFIT-Code"
Abschlußbericht, Nova Acta Leopoldina Supplementum Nr. 14, (1996) 361-376

[4] F. Bergner, U. Bergmann, V. Fleischer
"Das Konzept des Ultraschall-Laufzeit-Prozeßablauf-Bildes"
Seminar für zerstörungsfreie Materialcharakterisierung, Jena 14.-15.10.1996


## Acknowledgement


EFIT simulations could be performed by one of the authors (Bergmann) during a stay at the Dept. of Electrical Engineering of the Kassel University and was supported by a sponsoring award of the Deutsche Akademie der Naturforscher LEOPOLDINA. The author would like to thank Professor Langenberg and his coworkers for their assistance.

# MEASUREMENT OF ACOUSTIC EMISSION DURING DYNAMIC BEND TESTING

**H. Richter, J. Böhmert and H.-W. Viehrig**

## 1. Introduction

The J-integral is an appropriate parameter to characterize ductile material behaviour, which can even be determined with small specimens [1]. Its determination as dynamic toughness value by impact testing causes problems because the moment of the crack initiation cannot obviously be recognized on the load-time curve under the condition of stable crack growth.

It was already reported in an earlier paper [2] about attempts to detect the crack initiation by means of the acoustic emission (AE). The measuring configuration used in [2] applies a piezoelectric AE-broadband sensor which was placed within a drilled hole of the impact tup. Though with this configuration characteristic signals for stable crack initiation could be classified a general interpretation of the AE signals obtained was not possible. Therefore, a modified arrangement should be made-up considering the following require-ments:

- avoiding intensive AE due to elastic interactions between tup, specimen and anvil
- localizing the AE source
- increasing the sensitivity against the processes near the crack tip
- being comparable with the loading condition by impact testing.

## 2. Experimental

The above-mentioned requirements could well be met with the arrangement shown in Fig.1. Fatigue-cracked side grooved specimens in Charpy geometry (10 mm * 10 mm * 55 mm) are loaded on a servohydraulic tester (MTS 810/ Teststar) with an initial displacement rate of 0.1 m/s.

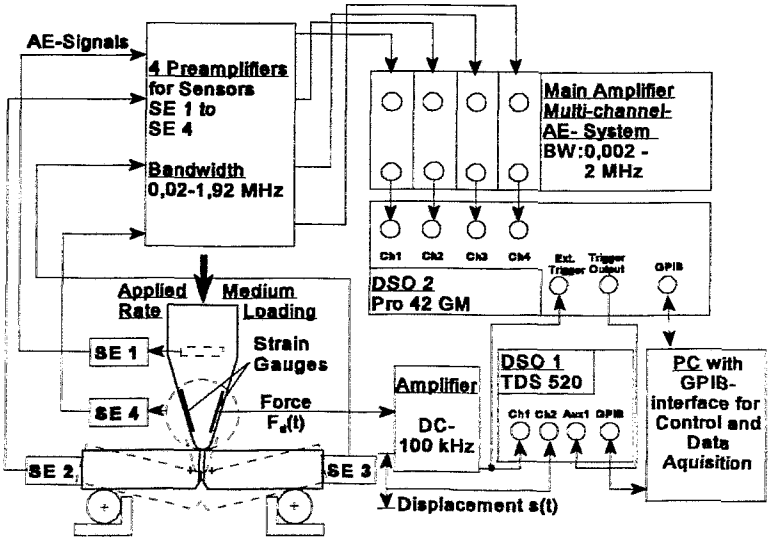


Fig.1: Experimental set-up for dynamic three point bend (TPB) testing.

For the loading punch the same instrumented tup is used as in the impact tests. Additionally to the AE sensor within the tup (SE1 in Fig.1) the specimen is equipped with AE sensors directly mounted at the front sur-

face (SE 2 and 3). A fourth sensor (SE 4) is fixed at the tup and is to reveal frictional noise between tup and specimen.

The force $F_d(t)$ is measured by strain-gauges application at the tup in the same way like in the impact tests. The displacement s(t) is obtained as a machine output signal. All signals are recorded by a digital storage oscilloscope (DSO 2) after appropriate amplification, transfered to a PC through the GPIB interface and evaluated with the software FAMOS.

The specimens were machined from a rolled plate of bainitic-ferritic 10CrMo9.10 steel in transverse orientation. The steel exhibits high toughness (upper shelf energy = 250 J, transition temperature = -45°C related to 68J impact energy).

## 3. Results

Fig. 2 shows the first part of a typical force -time curve and the simultaneously recorded AE signals.

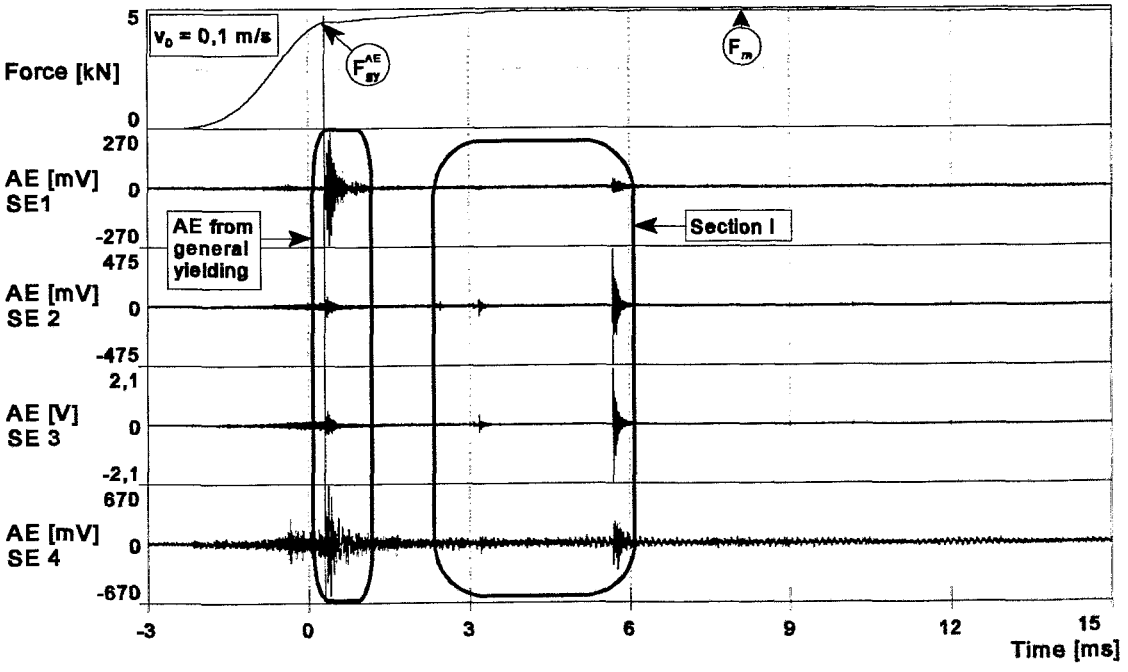


Fig.2: Typical force-time curve and AE signals of the sensors SE 1 to SE 4 from a dynamic TPB test.

Contrary to the results from impact tests there are no oscillations in the load trace and the AE activity is low at the begin of loading. The AE characteristic is not continuous but concentrated in a few bursts of high AE. A first AE burst occurs near the load for general yielding ($F_{gy}$) and can be observed in each of the four sensors. It is unambiguously caused by plastic deformation within the ligament. Further AE bursts appear in the range between general yielding and maximum force ($F_m$) without detecting irregularities in the force-time curve. They cannot be detected in the response of all sensors. Whereas the front face fixed sensors are very sensitive, the tup-integrated sensor (SE 1) records these signals with clearly weaker intensity. This cannot only be explained by the different positions of the sensors and the influence of interfaces but, comparing the

signals of the different sensors, it must be considered that the acoustic properties of the sensors are different as well. Even, the different directional characteristics of the AE source in the different test runs might have influence. Thus, sensor SE 1 does not always show the lowest sensitivity but is, for instance, very sensitive to the yielding-caused AE type.

The analysis according to the 2-channel-coincindence-principle [3] allows to localize the source of the AE using the arrival time at SE 2 and SE3. Both the first and the following AE bursts originate from the crack plane.

The working hypothesis was used that the first coincident signal which can be detected by every sensor characterizes the crack initiation. This signal is represented in Fig. 3 with higher amplification.

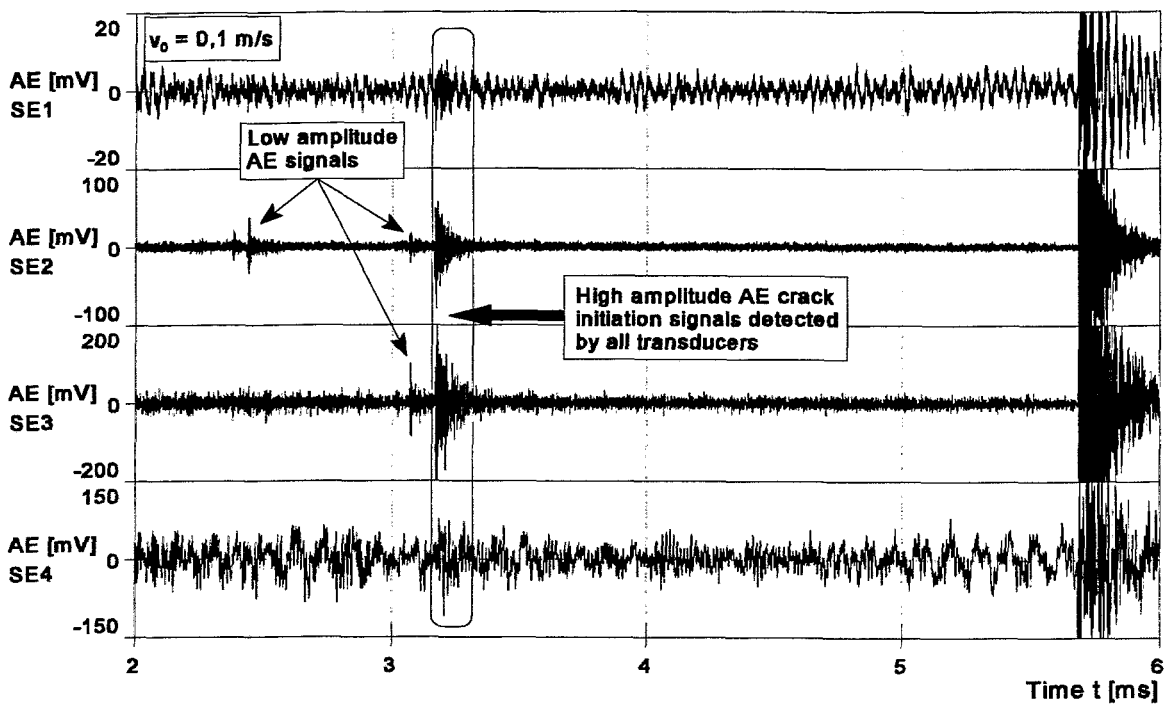


Fig.3: Zoomed signals of section I from Fig. 2.

An indirect prove for the hypothesis provides the multiple specimen technique. Tests were finished after different crack growth, the specimens were broken at liquid nitrogen temperature and the stable crack growth was optically measured. In this way a crack resistance curve was obtained and, measuring additionally the stretch zone width (SZW), the physical crack initiation toughness ($J_{id}^{SZW}$) could be determined. The result is shown in Fig. 4 (curve TPB) which also contains a crack resistance curve from impact tests (curve Low Blow and Cleavage-R). The crack initiation toughness is higher but in acceptable correspondence to the value that is determined by AE. As ductile crack initiation must not be interpreted like a definite event but like a process the difference does not contradict the mentioned hypothesis but only confirm that AE is more sensitive to crack formation than the integrated load-displacement behaviour.

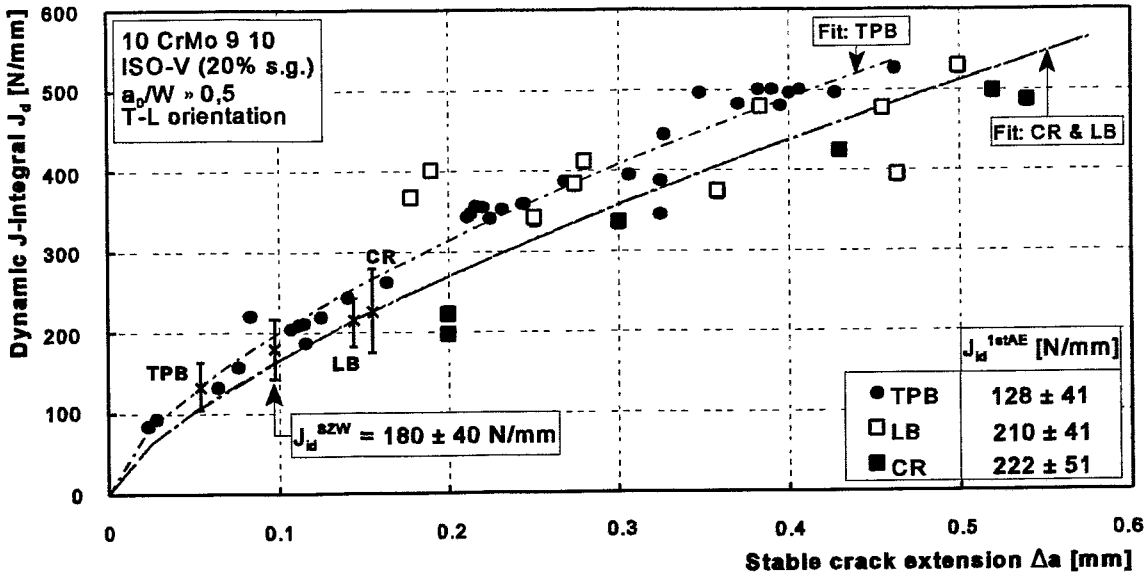


Fig.4: Dynamic TPB and impact (LB & CR) $J_R$ curves with scatter bands for ductile crack initiation obtained with different methods based on AE ($J_{id}^{1stAE}$) and physical crack initiation toughness ($J_{id}^{SZW}$), respectively.

## 4. Conclusions

Measurements of the AE during a dynamic bending deformation show that processes within a highly tough steel are connected with characteristic AE signals. A burst-type signal appears near the crack initiation. This signal is detected with highest sensitivity by sensors directly fixed on the specimen. An AE sensor positioned within the tup, which is employed like a loading punch, recognized such signals as well, however, with lower amplitude. The dynamic bending tests correspond to the results of the impact tests. There is no certainty that the weak measuring signal connected with crack initiation can always be detected under impact test condition because here strong oscillations of the load and, thus, high acoustic activity occur in the initial phase of loading. An early crack initiation might so be covered. Therefore, the spectral and absolute sensitivity of the tup sensor must be improved.

## References

[1] E. Ross: Grundlagen und notwendige Voraussetzungen zur Anwendung der Rißwiderstandskurve in der Sicherheitsanalyse angerissener Bauteile, VDI-Fortschritt Berichte Reihe 18: Mechanik /Bruchmechanik, Nr.:122; VDI-Verlag, 1993.

[2] H. Richter and H.-W. Viehrig: Determination of the Dynamic Crack-Initiation Toughness During Instrumented Impact Tests for Elastic-Plastic Material Behaviour, FZR - Forschungszentrum Rossendorf, Annual Report 1995, Institute of Safety Research 1994, FZR -126, Juni 1995, S. 35-41.

[3] S. Yamaoka, K. Wakita and T. Kishi: Acoustic Emission Signal Analysis of Micro-fracturing Process in C-1/2Mo Steel, Proceedings of the 7th Acoustic Emission Symposium, Zao, Japan, 1984, pp. 16-23.

# INFLUENCE OF THE INPUT NEUTRON SPECTRUM COVARIANCES UPON THE RESULTS OF THE SPECTRUM ADJUSTMENT FOR PRESSURE VESSEL NEUTRON FLUENCES

**B. Boehmer, G. Manturov[1]**

## 1. Introduction

One of the most critical problems in the practical application of spectrum adjustment in pressure vessel dosimetry is the insufficient knowledge of the input fluence spectrum covariance matrix. Usually very crude approximations for this covariance matrix are used in adjustment procedures and, moreover, it is not clear to which extent these approximations influence the final results. Therefore, it appeared useful to calculate this matrix as carefully as possible for a typical system, particularly at positions for which a sufficient amount of activation measurements and precise transport calculations are available. The paper presents and discusses results of covariance calculations for a VVER-1000 type reactor. They build up on the one hand on sensitivity coefficients estimated in transport calculations by means of the ANISN code and on the other hand on cross section covariance data taken from the Obninsk ABBN-93 data library. The results of spectrum adjustments based on the estimated covariance matrix are compared with results based on formerly used matrices. The obtained differences are discussed.

## 2. The Method of Spectrum Covariance Calculations

The covariances of the fluence group spectra values are caused by the uncertainties of all input parameters of the calculation, by the inadequacy of the calculational model and by the approximations in the calculational method. Since it is possible to calculate with the Monte Carlo code TRAMO [1] the reactor in all details and with sufficient energy and angular resolution it can be assumed that the uncertainties in the calculational model and in the calculational method will be negligible. Thus, there remain the uncertainties of the input data only. The following particular sources of uncertainties considered as most important have been taken into account:

*a)Neutron Cross Sections*

- the inelastic, elastic, and capture group cross sections of iron
- the elastic group cross sections of hydrogen and oxygen,

*b)Neutron Source Distributions*

- the uncertainty of the energy distribution of the neutron source
- the uncertainty of the spatial source distribution,

*c)Geometrical Dimensions and Material Densities*

Their uncertainties are difficult to specify. They can vary even from reactor to reactor of the same type and depend on the quality of available information. They were estimated using tolerances prescribed by the constructors, information from consultations with German and Russian VVER experts as well as the corresponding uncertainties found in LEPRICON [2] reports. The following standard deviations were assumed for the main error sources of type c):

[1]Institute of Physics and Power Engineering Obninsk, Russia

- Downcomer water thickness due to out-of-roundness of the vessel ±0.5cm
- Steel cladding thickness ±0.1cm
- Pressure vessel thickness ±0.2cm
- Pressure vessel steel density ±1 %
- Coolant water density ±2 %.

Fortunately, type c) uncertainty source has not shown a decisive influence on the total spectrum covariances although the uncertainties had been assumed larger than the known project tolerances.

For each uncertainty source a partial fluence covariance matrix $V_k$ is calculated:

$$V_k = H_k W_k H_k^T \quad .$$

Here, $H_k$ is the matrix of sensitivity coefficients of the group fluences related to the parameters of type k. $W_k$ is the covariance matrix of the parameters of type k. $V_k$ is the flux covariance matrix obtained if only parameters of type k (e.g. the fission spectrum values) are considered. The total group spectrum covariance matrix V is calculated as the sum of the partial matrices:

$$V = \sum_{k=1}^{n} V_k \quad .$$

The results are presented in form of correlation matrices and vectors of relative (to the mean values) standard deviations (RSD). The sensitivity matrices $H_k$ were calculated by a direct perturbation method with the help of the one-dimensional transport code ANISN. The replacement of the three-dimensional model by a one-dimensional model is an essential approximation, however it is sufficient for the considered uncertainty sources and spectra at given positions. To calculate correlations between different vertical or angular positions would indeed require at least two-dimensional calculations. But that was not the aim of this work.

The $W_k$ matrices are obviously quite simple for the category c) of the considered sources of uncertainties. In the case of uncertainties associated with neutron cross sections and the energy distribution of the fission source the corresponding $W_k$ matrices were taken from the Library of Uncertainties of Nuclear Data (LUND). The LUND data base is included in the INDECS data code system [3]. It presents correlation matrices and RSD for the Russian ABBN-93 group data set in the ABBN 28-energy-group structure [4].

Fluence uncertainty data associated with nuclear data and neutron source uncertainties are given in Table 1. Table 2 shows the analogous data related to the uncertainties of geometrical dimensions and densities, whereas the total fluence covariance data are presented in Table 3. In all cases only the first 12 ABBN energy groups which are essential for embrittlement have been considered.

### 3. Spectrum Adjustment

For these investigations the transport calculations and experiments described in [6] have been used. The spectrum adjustment was performed with the code system

COSA2 [5,6]. Detector cross sections and their covariances were calculated using the latest version of IRDF-90 [7]. The input spectra were calculated with the TRAMO code for 29 groups above 21.875 keV, a subset of the VITAMIN/N175 group structure. The

Table 1: Fluence correlation matrix and RSD, associated with neutron cross setions and neutron source uncertainties (2nd column: ABBN 28-group energy boundaries for the first 12 groups)

| GR | $E_{upper}$ (MeV) | RSD % | correlation coefficients multiplied by 100 | | | | | | | | | | | |
|---|---|---|---|---|---|---|---|---|---|---|---|---|---|---|
| | | | 1 | 2 | 3 | 4 | 5 | 6 | 7 | 8 | 9 | 10 | 11 | 12 |
| 1 | 15.0 | 42.2 | 100 | | | | | | | | | | | |
| 2 | 13.98 | 36.7 | 60 | 100 | | | | | | | | | | |
| 3 | 10.5 | 35.1 | 50 | 71 | 100 | | | | | | | | | |
| 4 | 6.5 | 35.1 | 44 | 61 | 86 | 100 | | | | | | | | |
| 5 | 4.0 | 29.8 | 36 | 43 | 66 | 73 | 100 | | | | | | | |
| 6 | 2.5 | 23.2 | 32 | 39 | 49 | 59 | 74 | 100 | | | | | | |
| 7 | 1.4 | 22.4 | 32 | 43 | 56 | 64 | 73 | 95 | 100 | | | | | |
| 8 | 0.8 | 21.4 | 35 | 45 | 61 | 69 | 81 | 93 | 96 | 100 | | | | |
| 9 | 0.4 | 20.1 | 33 | 46 | 61 | 69 | 81 | 90 | 94 | 98 | 100 | | | |
| 10 | 0.2 | 19.7 | 31 | 45 | 60 | 68 | 80 | 88 | 92 | 96 | 98 | 100 | | |
| 11 | 0.1 | 18.7 | 32 | 45 | 60 | 68 | 80 | 88 | 92 | 96 | 98 | 98 | 100 | |
| 12 | 0.0465 | 17.4 | 30 | 45 | 58 | 66 | 77 | 86 | 89 | 93 | 96 | 97 | 98 | 100 |

$E_{lower}$(12th group) = 0.0215MeV

Table 2: Fluence correlation matrix and RSD associated with geometrical dimensions and densities

| GR | RSD % | correlation coefficients multiplied by 100 | | | | | | | | | | | |
|---|---|---|---|---|---|---|---|---|---|---|---|---|---|
| | | 1 | 2 | 3 | 4 | 5 | 6 | 7 | 8 | 9 | 10 | 11 | 12 |
| 1 | 11.4 | 100 | | | | | | | | | | | |
| 2 | 10.4 | 98 | 100 | | | | | | | | | | |
| 3 | 11.4 | 98 | 98 | 100 | | | | | | | | | |
| 4 | 12.3 | 97 | 98 | 98 | 100 | | | | | | | | |
| 5 | 12.4 | 95 | 97 | 98 | 98 | 100 | | | | | | | |
| 6 | 12.1 | 92 | 95 | 96 | 97 | 98 | 100 | | | | | | |
| 7 | 11.1 | 83 | 88 | 89 | 91 | 94 | 96 | 100 | | | | | |
| 8 | 10.4 | 68 | 76 | 77 | 80 | 84 | 89 | 96 | 100 | | | | |
| 9 | 10.4 | 55 | 64 | 65 | 69 | 74 | 81 | 91 | 97 | 100 | | | |
| 10 | 10.6 | 49 | 58 | 59 | 63 | 69 | 76 | 88 | 96 | 98 | 100 | | |
| 11 | 10.7 | 48 | 58 | 58 | 62 | 69 | 76 | 87 | 95 | 98 | 98 | 100 | |
| 12 | 11.0 | 47 | 56 | 57 | 61 | 67 | 75 | 86 | 95 | 98 | 98 | 98 | 100 |

used reaction rates result from German and Russian activation measurements [8] with detectors irradiated at the Rovno-3 power plant during cycle 7 at 15 positions at the outer boundary of the pressure vessel. Rather large relative standard deviations (6% for $^{54}Fe(n,p)^{54}Mn$, 8% for $^{58}Ni(n,p)^{58}Co$, $^{46}Ti(n,p)^{46}Sc$, $^{63}Cu(n,\alpha)^{60}Co$ and 10% for $^{93}Nb(n,n')^{93m}Nb$, $^{237}Np(n,f)$) have been assumed for these reaction rates based not only on the known sources of uncertainties of the measurements but also on internal inconsistencies of the results. As for each detector an independent calibration source

was available, correlations between detectors caused by measurements were negligible. Additionally, a fully correlated 3% normalization error caused by the reactor power uncertainty was included in the covariances of the reaction rates.

Table 3: Total correlation matrix and RSD for the outer surface of the pressure vessel

| GR | RSD % | correlation coefficients multiplied by 100 | | | | | | | | | | | |
|---|---|---|---|---|---|---|---|---|---|---|---|---|---|
| | | 1 | 2 | 3 | 4 | 5 | 6 | 7 | 8 | 9 | 10 | 11 | 12 |
| 1 | 44.1 | 100 | | | | | | | | | | | |
| 2 | 38.1 | 62 | 100 | | | | | | | | | | |
| 3 | 36.9 | 53 | 73 | 100 | | | | | | | | | |
| 4 | 37.2 | 48 | 64 | 87 | 100 | | | | | | | | |
| 5 | 32.3 | 41 | 48 | 69 | 76 | 100 | | | | | | | |
| 6 | 26.2 | 38 | 45 | 55 | 64 | 77 | 100 | | | | | | |
| 7 | 25.0 | 37 | 47 | 59 | 67 | 76 | 95 | 100 | | | | | |
| 8 | 23.8 | 38 | 47 | 62 | 70 | 81 | 92 | 95 | 100 | | | | |
| 9 | 22.6 | 34 | 47 | 60 | 68 | 79 | 88 | 93 | 97 | 100 | | | |
| 10 | 22.4 | 32 | 45 | 58 | 66 | 77 | 85 | 91 | 95 | 97 | 100 | | |
| 11 | 21.5 | 32 | 45 | 58 | 65 | 77 | 85 | 90 | 95 | 97 | 97 | 100 | |
| 12 | 20.6 | 30 | 44 | 56 | 63 | 73 | 82 | 87 | 92 | 96 | 97 | 97 | 100 |

The spectrum covariances calculated for the first 12 ABBN groups and the different LEPRICON covariance matrices were transformed to a 29 group structure by COSA2 subroutines, based on [9]. The following types of spectrum covariance matrices were used in the adjustments:

1. ABBN/LUND VVER-1000 - this work
2. REAL88/ANO/LEPRICON - ANO covariance data taken from the REAL-88 file [10]
3. ABBN/LUND VVER-1000 - with reduced RSD (15% in all groups, used in [6])
4. REAL88/PS2/LEPRICON correlations combined with own RSD
5. GAUSS1 - Gaussian distributed correlations [5]
6. GAUSS2 - Gaussian distributed plus constant correlations

The REAL88/ANO/LEPRICON correlation matrix is very similar to the calculated one. Only the relative standard deviations are in the ANO case somewhat lower in the higher energy groups. In both cases the relative large standard deviations seem to contradict the usually achieved agreement between activation experiments and three-dimensional calculations and to the not so large differences usually obtained in calculations with different cross section files. Possibly the uncertainty estimations given in the nuclear data files are too pessimistic. On the other hand there may be a compensation of errors in practical pressure vessel dosimetry work, connected with the effect that usually errors are searched for and corrected only so long as the agreement between theory and experiment is not satisfying.

## 4. Results of the Spectrum Adjustments

In Fig.1 adjusted flux spectra obtained with different spectrum covariance matrices are given together with the unadjusted spectrum for a detector position at the middle plane of the reactor near the flux maximum (Experiment h118.5) [8]. The different adjusted

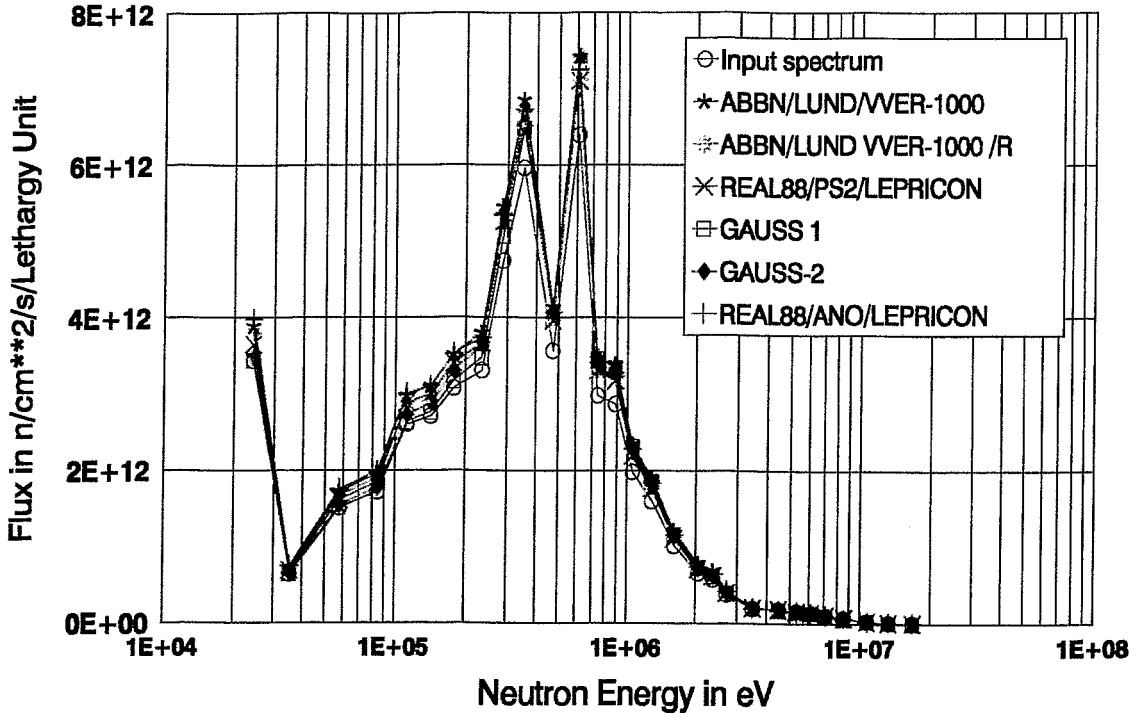


Fig.1: Input spectrum and adjusted spectra obtained with different spectrum covariance matrices for experiment h118.5, Rovno-3, 7th cycle.

Table 6: Fluence integrals $\Phi_{E>1.0MeV}$ in units of $10^{16}$ n/cm$^2$ and their RSD at 3 positions for input spectrum and adjusted spectra using different input spectrum covariance

| Spectrum Covariances Used for Adjustment | Experim. h118.5 | | Experim. h114.7 | | Experim. h92.0 | |
|---|---|---|---|---|---|---|
| | $\Phi_{E>1.0MeV}$ | $\delta\Phi/\Phi$ % | $\Phi_{E>1.0MeV}$ | $\delta\Phi/\Phi$ % | $\Phi_{E>1.0MeV}$ | $\delta\Phi/\Phi$ % |
| not adjusted (input spectrum) | 335 | 21 | 347 | 21 | 203 | 21 |
| ABBN/LUND VVER-1000 | 388 | 7 | 376 | 9 | 203 | 9 |
| REAL88/ANO/LEPRICON | 375 | 7 | 369 | 8 | 204 | 9 |
| ABBN/LUND/VVER-1000/R | 370 | 6 | 365 | 7 | 201 | 7 |
| REAL88/PS2/LEPRICON | 362 | 6 | 363 | 7 | 201 | 7 |
| GAUSS-1 | 377 | 7 | 368 | 8 | 201 | 9 |
| GAUSS-2 | 373 | 7 | 367 | 8 | 200 | 8 |

spectra agree well for higher energies and disagree to some extent at lower energies. The reason is that the relations between calculated and experimental reaction rates (C/E - values) are rather low for the Nb and Np detectors, whereas the high energy detectors have C/E - values near one. With different spectrum covariances, the adjust-

ment procedure considers this situation in different ways. Depending on the uncertainties more or less information is taken from the experiment. Obviously, in cases with better agreement between measured and calculated reaction rates the differences between results from adjustments with different matrices are smaller. This can be observed in Table 6, where similar adjustment results for the fluence integrals $\Phi_{E>1.0MeV}$ at 3 positions are compared with the unadjusted values. In all cases the differences between the results with different covariance matrices were lower than their standard deviations ($\leq$7%). Similar results were obtained for the other positions considered in [8].

## 5. Conclusions

The dominating uncertainty sources for the calculated covariance matrix of the fluence spectrum at the outer surface of the VVER-1000 pressure vessel are the uncertainties of the neutron cross sections and of the fission spectrum. The high uncertainty level obtained for the calculated spectra seems to contradict the achieved agreement between precise calculations and measurements. The influence of different spectrum covariance matrices on the adjustment results proved to be relatively low. This indicates, that older adjustments possibly would not be affected very much by using correct spectrum covariances, provided that the discrepancies between theory and experiment are not too large and the detectors are sensitive in the whole interesting energy region. To get optimal results in all situations realistic spectrum covariances are needed. Spectrum covariance calculations with improved uncertainty input data and a two-dimensional reactor model are recommended.

## 6. References


[1] H.-U. Barz
"TRAMO - a Flexible Multigroup Neutron Transport Code on the Basis of the Monte Carlo Method for Flux Calculations", *ZfK- 705*, Rossendorf 1990

[2] R.E. Maerker, B.L. Broadhead, J.J. Wagschal
Nucl. Sci. Eng. 9 (1985) 369-392

[3] G.N. Manturov
"Influence of Neutron Data Uncertainties on the Accuracy of Prediction of Advanced Reactor Characteristics", Proc. of Intern. Conf. on Nuclear Data for Science and Technology, Gatlinburg, Tennessee, USA, (1994), Vol.2, p.993-999.

[4] G.N. Manturov, M.N. Nikolaev, A.M. Tsiboulia
"ABBN-93 Group Data set", Recommended Reference Data, Report CNIIal,M., (1995) (in Russian).

[5] B.Böhmer
COSA2 - Ein Spektrumsjustierungsprogramm zur Auswertung von Aktivierungsmessungen auf der Basis der verallgemeinerten Methode der kleinsten Quadrate, *ZfK-735*, Rossendorf 1991

[6] H.-U. Barz, B. Böhmer, J. Konheiser, I. Stephan
Ermittlung der Neutronendosis von bestrahlten WWER-Reaktordruckbehältermaterialien, *FZR-87*, 1995

[7] N.P. Kocherov
Neutron Metrology File NMF-90, An integrated database for performing neutron spectrum adjustment calculations,, IAEA-NDS-171, Jan. 1996

[8] H.-U. Barz, G. Borodkin, B. Boehmer, J. Konheiser, I. Stephan
Determination of Pressure Vessel Neutron Fluence Spectra for a Low Leakage Rovno-3 Reactor Core Using Three Dimensional Monte Carlo Neutron Transport Calculations and Ex-vessel Neutron Activation Data, Proceedings of the 9th International Symposium on Reactor Dosimetry, Prag Sept. 1996, to be published

[9] N. Marseguerra, V. Sanguist, M. Petilli
Covariances of Neutron Fluxes and Cross Sections in Group Structure Variation, Nucl. Sci. Engin. 87(1984)28-33

[10] H.J. Nolthenius
Progress Report on the REAL88 Exercise, ECN-89-140, Petten, Sept. 1989

# DETERMINATION OF PRESSURE VESSEL NEUTRON FLUENCE SPECTRA FOR A LOW LEAKAGE ROVNO-3 REACTOR CORE USING THREE-DIMENSIONAL MONTE CARLO NEUTRON TRANSPORT CALCULATIONS AND EX-VESSEL NEUTRON ACTIVATION DATA

**H.-U. Barz, B. Boehmer, J. Konheiser, I. Stephan, G. Borodkin[1]**

## 1. Introduction

With respect to embrittlement problems the knowledge of the accurate distribution of neutron fluences is a very important information especially for VVER-1000 type reactors, where a high Ni-content of the pressure vessel implicates faster embrittlement and unfavourable arrangements of the surveillance probes complicate the embrittlement control. Fluence calculations are as well needed to assess the fluences at neutron detector positions since activation measurements are used to support the calculations.

As the reactor and all surrounding components constitute a complicated geometrical structure and a three-dimensional distribution of fluences is required, also a three-dimensional neutron transport calculation is necessary. For this task Monte Carlo simulation is the favoured method. All geometric details can be considered and the problem of statistical errors can be mastered using modern variance reducing methods. All these methods including codes for the preparation of integral fission sources are available at Forschungszentrum Rossendorf. The application of these methods to similar problems was very successful in the past [1,2,3]. Activation measurements (ex-vessel measurements) can be used to proof and, if necessary, to adjust the calculations.

In the following, investigations related to the VVER-1000 reactor Rovno-3/ Ukraine are described. All needed fuel cycle data were made available by the Russian Nuclear Regulatory Authority (GOSATOMNADZOR). Moreover, activation measurements were performed at the outer surface of the pressure vessel.

The work reported on, is based on a German/Russian collaboration between Forschungszentrum Rossendorf and the Scientific and Engineering Centre of Russian GOSATOMNADZOR. Part of the work is supported by the German Federal Ministry of Education and Research.

## 2. Calculation

### 2.1 Monte Carlo fluence calculation

The calculation results represented in the following were obtained by the Monte Carlo

[1]Scientific Engineering Centre for Nuclear and Radiation Safety of Russian GOSATOMNADZOR, Moscow

code TRAMO [1] that was developed in Rossendorf. The Monte Carlo method has many advantages in comparison to other methods, because the realistic technical system with all geometrical details can be taken into account and the source distribution for the fuel pins can also be treated three-dimensionally.

The main problems of Monte Carlo calculations are connected with the statistical errors. To diminish these errors the " weight window " method has been applied in a general manner [4]. The weights are also determined by Monte Carlo calculations using the own code TRAWEI. This technique decreases the statistical errors even for neutron source locations which are far from the detector region.

To improve the consideration of the core power distribution and even the power distribution over the single fuel elements, a modified technique was applied to determine the neutron source locations. The fuel element and vertical region is randomly selected according to the coarse source distribution. Having found such a region all fuel rods within this element are treated. For each fuel rod one neutron is generated. The special position is selected randomly only for this rod. The different source contribution of the special rods is taken into account by weights. In this connection the possibility of biasing of the space distribution of sources was introduced to get smaller differences in the contribution of the source of a given part of the fuel element.

Further improvements are related to code handling. So the number of inputs is diminished to the really necessary information. Furthermore, all input data are checked before starting and an extended error documentation is given to support the user.

### 2.2 Collection and preparation of reactor data

All the geometrical and material data (including pinwise power and burn up distribution) of the reactor and the fuel cycle history are needed for the given irradiation period. The distribution of the power and burn up over the assemblies has been obtained from a three-dimensional two-group neutron-physical calculation of the reactor core during the 7th cycle. The pinwise burn up and the power distribution for each axial layer of the peripheral assemblies were calculated using a few group two-dimensional diffusion code. The results of these calculations were made available by the Rovno utilities. All these calculations were performed for a number of time points within the fuel cycle. Additionally, also the information about the mean number of fission neutrons and the concentration of important fissionable isotopes could be considered for different starting enrichments as a function of burn up.

It was necessary to develope a number of codes for processing of the obtained input data. To mention only some problems: Codes were needed for the

- extraction of data from Russian text files,
- calculation of time averaged water densities from power dates of each fuel element,
- polynomial representation of fissionable isotop concentrations and of the mean number of fission neutrons depending on burn up,
- calculation of time integrated pinwise fission sources and of "effective" sources (taking into account the decay of detectors) for different fissionable isotopes ($U^{235}$, $Pu^{239}$ and $U^{238}$) for the given irradiation period,
- calculation of the relative (to the center of the assembly) space distribution of fuel

pins taking into account the dummy places.

### 2.3 Neutron cross sections

175-group cross sections (Vitamin-J structure) together with f-factors and P-5 Legendre polynoms for all scattering processes at all relevant isotopes were calculated using ENDF/B-VI data and the NJOY-code. The data finally needed for the Monte Carlo simulation, e.g. macroscopic cross sections and probabilities of different reactions, were prepared with the interface modul MODAJ. As an exception scattering at hydrogen was treated not in group approximation but exactly using the correct scattering laws in the center of mass system. All calculations were performed using the first 123 groups. The spectral results are represented for a broader group structure (29 groups) to diminish the statistical errors and the amount of data.

### 2.4 Calculation results

For each fissionable isotop a Monte Carlo calculation was performed. These single solutions were superimposed to get the total solution. Fig. 1 shows a simplified top view of the Rovno-3 reactor. The fluences were calculated for the detector positions marked in Fig.1 for the height intervall between 139 cm and 159 cm above the core

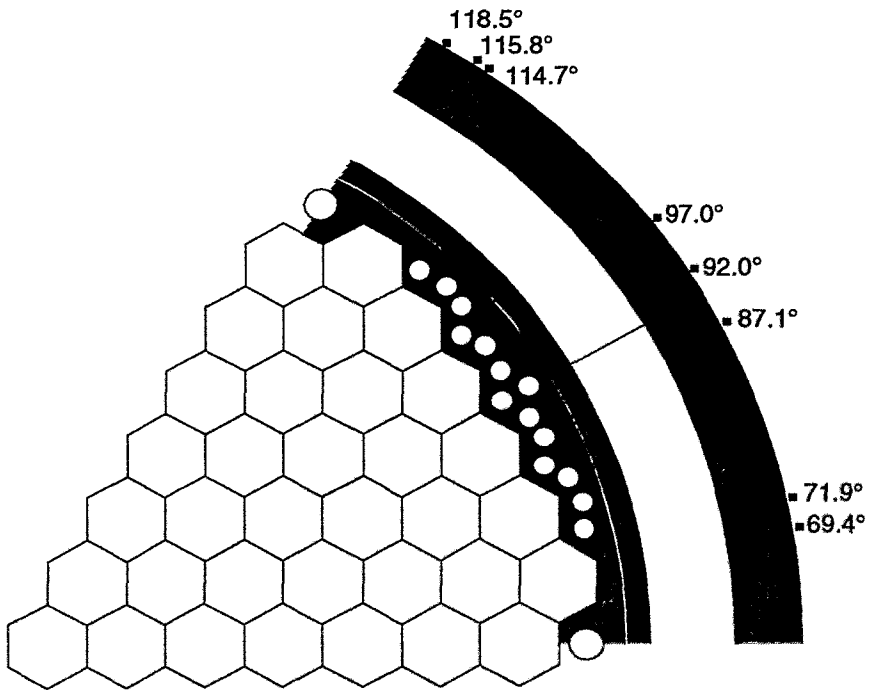


Fig.1: Top view of a simplified symmetry sector and monitor positions of the Rovno-3 reactor

bottom. At the 97° azimuthal position additional detectors were installed at different heights. Table 1 presents the obtained fluences for the different detector regions together with the statistical errors.
The first two groups excepted, also the group spectra not given in this Table have 1-$\sigma$

errors of the magnitude of 1%. However these two groups only little contribute to the total fluence. The spectra are very similiar for the different positions. For some selected examples the normalized spectra are shown in Fig. 2.

Table 1: Fluences and 1-σ statistical errors for the different azimuthal detector positions

| angle | total fluence | fluence>1.0 MeV | fluence>.5 MeV |
|---|---|---|---|
| 69.4° | 3.1937E+17(±0.43%) | 3.5023E+16(±0.42%) | 1.0759E+17(±0.32%) |
| 71.9° | 3.0733E+17(±0.43%) | 3.3548E+16(±0.42%) | 1.0331E+17(±0.30%) |
| 87.1° | 2.2012E+17(±0.42%) | 2.0597E+16(±0.62%) | 6.6694E+16(±0.42%) |
| 92.0° | 2.1760E+17(±0.49%) | 2.0257E+16(±0.61%) | 6.5642E+16(±0.41%) |
| 97.0° | 2.3470E+17(±0.44%) | 2.2821E+16(±0.60%) | 7.2854E+16(±0.40%) |
| 114.7° | 3.1981E+17(±0.51%) | 3.4577E+16(±0.48%) | 1.0693E+17(±0.36%) |
| 115.8° | 3.1936E+17(±0.54%) | 3.4209E+16(±0.48%) | 1.0635E+17(±0.36%) |
| 118.5° | 3.1456E+17(±0.52%) | 3.3439E+16(±0.51%) | 1.0371E+17(±0.37%) |

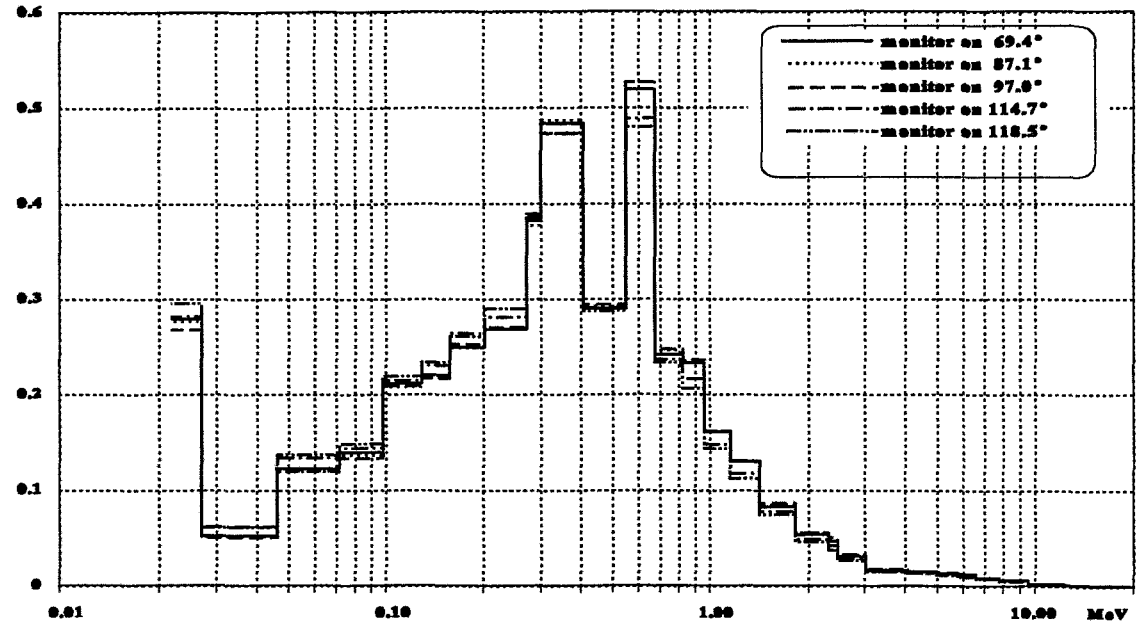


Fig. 2: Normalized group fluences per lethargy intervall

## 3. Activation Measurements

The technical realization of the irradiations was carried out by SEC with the help of the Rovno NPP staff using methods described in [6]. Activation detectors from SEC and FZR have been irradiated during the 7th cycle partly in identical positions. The following detector reactions were used:
$^{63}Cu(n,\alpha)^{60}Co$, $^{54}Fe(n,p)^{54}Mn$, $^{93}Nb(n,n')^{93m}Nb$, $^{58}Ni(n,p)^{58}Co$, $^{46}Ti(n,p)^{46}Sc$, $^{109}Ag(n,\gamma)^{110m}Ag$, $^{59}Co(n,\gamma)^{60}Co$.
Only the five fast neutron detectors have been considered. Niobium activation has

been measured for each detector in two ways. At first directly from the foil, which has a γ-selfabsorption of approximately 11% and secondly by dissolving the foil, determining the concentration of the Niobium by means of ICP-spectroscopy and preparing samples with negligible γ-selfabsorption.

Using the global power history of cycle 7 and the decay characteristics of the detectors "experimental" reaction rates for nominal power were calculated from the measured activities. The effect of changing spatial and spectral distributions during the cycle was taken into account by additional correction coefficients. These coefficients were calculated by special Monte Carlo simulation applying the method of effective sources [3]. The SEC experimental reaction rates were taken from [5].

## 4. Comparison of Calculation and Experiment

Table 2 relates the experimental reaction rates obtained as described above to the reaction rates calculated from group fluences. Column "Comment" indicates the origin of the experimental data. For several positions and reactions two experimental reaction rates measured by SEC and FZR-detectors were available. The corresponding results agree within the experimental and calculational error limits.

Table 2: Relations between calculated (C) and experimental (E) reaction rates (C/E-values)

| No | Name | Comment | NP237F | NB93N | FE54P | NI58P | TI46P | CU63A |
|---|---|---|---|---|---|---|---|---|
| 1 | h118.5 | RCR 149 | ----- | 0.779 | 0.989 | 0.973 | 1.116 | 0.981 |
| 2 | h118.5 | SEC 149 | 0.836 | ----- | 1.029 | 1.012 | ----- | ----- |
| 3 | h115.8 | SEC 149 | ----- | ----- | 1.031 | ----- | ----- | ----- |
| 4 | h114.7 | RCR 149 | ----- | 0.837 | 1.008 | 0.989 | 0.979 | 0.978 |
| 5 | h114.7 | SEC 149 | ----- | ----- | 1.043 | 1.023 | ----- | 0.976 |
| 6 | h69.4 | SEC 149 | ----- | ----- | 1.042 | ----- | ----- | ----- |
| 7 | h71.9 | SEC 149 | ----- | ----- | 1.022 | ----- | ----- | ----- |
| 8 | h97.0 | SEC 149 | ----- | ----- | 1.121 | ----- | ----- | ----- |
| 9 | h87.1 | SEC 149 | 0.803 | ----- | 1.071 | ----- | ----- | ----- |
| 10 | h92.0 | RCR 149 | ----- | 0.944 | 1.055 | 1.047 | 1.040 | 0.914 |
| 11 | h92.0 | SEC 149 | ----- | ----- | 1.108 | 1.131 | ----- | 1.043 |
| 12 | v118 | SEC 23d | ----- | ----- | 1.161 | ----- | ----- | ----- |
| 13 | v184 | SEC 23d | ----- | ----- | 1.084 | ----- | ----- | ----- |
| 14 | v241 | SEC 23d | ----- | ----- | 1.082 | ----- | ----- | ----- |
| 15 | v302 | SEC 23d | ----- | ----- | 1.017 | ----- | ----- | ----- |

For the high energy detectors $^{54}Fe(n,p)^{54}Mn$, $^{58}Ni(n,p)^{58}Co$, $^{46}Ti(n,p)^{46}Sc$ and $^{63}Cu(n,\alpha)^{60}Co$ comparatively low discrepancies between the experiment and the calculations are observed, whereas for the $^{93}Nb(n.n')^{93m}Nb$ and $^{237}Np(n,f)$ reactions rather low C/E values were obtained (with exception of position h92.0 for $^{93}Nb(n.n')^{93m}Nb$). The mean C/E is 1.0077, the standard deviation of C/E 9.07%.

As the niobium measurements have greater uncertainties according to the very low activation and only three niobium detectors at different positions are used, these results cannot be considered as final up to now. Possibly the IRDF-90 $^{93}Nb(n.n')^{93m}Nb$ cross sections are too low. With DOSCROS-84 cross sections e.g. all niobium-C/E values are greater. On the other hand, the niobium data from a new Russian evalua-

tion result in only little higher C/E values than IRDF-90.

## 5. Conclusions

For the low leakage Rovno-3 core high-precision three-dimensional Monte Carlo calculations are performed taking into account all the known details of the reactor and of the irradiation history. Fluence spectra at detector positions are obtained with sufficiently low statistical errors. The agreement between experimental and theoretical values is in general very good. Only for Nb- and Np-detectors the discrepancies are greater than expected and difficult to explain by spectrum changes. As for these detectors independent results from different laboratories do not exist additional inter-laboratory comparisons are recommended.

## Acknowledgments

The authors would like to thank Dmitry Sokolov and Anatoly Berezovets, Rovno NPP staff, for their assistance in the experiment and for providing the reactor core neutron-physical data.

## References

[1] H.-U. Barz TRAMO - a Flexible Multigroup Neutron Transport Code on the Basis of the Monte Carlo Method for Flux Calculations, ZfK- 705, Rossendorf 1990

[2] H.-U. Barz, W. Bertram, Calculation of neutron fluence in the region of the pressure vessel for the history of different reactors by using the Monte-Carlo-method, Nuclear Engineering and Design 137(1992)71-75

[3] H.-U. Barz, B. Böhmer, J. Konheiser, I. Stephan, Ermittlung der Neutronendosis von bestrahlten WWER-Reaktordruckbehältermaterialien, FZR-87, 1995

[4] H.-U. Barz, Problems of Weight Determination for the Multigroup Monte Carlo Code TRAMO for Neutron Flux Calculation, Progress in Nuclear Energy, Vol.24, pp. 69-75,1990

[5] G.I. Borodkin, E.B. Brodkin, A.L. Egorov, S.M. Zaritsky, The Neutron Fluence Monitor System for VVER-1000 Vessels and ist Validation, Proceedings of Radiation protection & shielding topical meeting No. Falmouth, Massachusetts, April 21-25, 1996

[6] G.I. Borodkin et al., Pressure Vessel Fluence Monitoring at NPP with VVER; Routine Technique and New Approaches, Proc. of 8th ASTM-EURATOM Symposium on Reactor Dosimetry, 29 Aug. - 3 Sep. 1993, Vail, Colorado, ASTM STP 1228 Harry Farrar IV et al., Philadelphia, 1994, pp.55-65

# MIGRATION OF POLLUTANTS IN MINING DUMPS

**R. Küchler, K. Noack**

## 1. Introduction

The problem of the dumps that have been produced from wastes of uranium mining is of great environmental concern for Saxonia. Unsaturated flows within subsurface regions control many large-scale hydrological and environmental processes. The aim of this subject is to calculate the release of pollutants from mining dumps due to these processes in the unsaturated zone. Basically, the problem to be solved can be subdivided into two steps:
1. The simulation of the water level and water flow in the dump.
2. The calculation of the transport of pollutants. The description of this transport includes as well chemical reactions as interacting processes which occur when water and oxygen are present.

## 2. Motion of water in the unsaturated zone

The two-dimensional water motion in an unsaturated, incompressible porous medium can be described by the Richards differential equation [1]:

$$\frac{\partial w}{\partial t} = \frac{\partial}{\partial x} k(w) \frac{\partial h}{\partial x} + \frac{\partial}{\partial z} k(w) \frac{\partial h}{\partial z} + e(w, x, z). \tag{1}$$

$w(x, z, t)$ is the volumetric water content of the soil, $h = -\psi + z$ is the total soil water potential (m), and $k(w)$ is the hydraulic conductivity of soil matrix. $\psi$ means the suction of the matrix (matrix potential) and z is the potential of gravity. $x, z$ are the horizontal and vertical coordinates. e(w) considers possible sources and sinks. It is important to note that the hydraulic conductivity strongly depends on the water content in the soil. Usually $k(w)$ is described by

$$k(w) = k_0 \left( \frac{w - w_R}{n_0 - w_R} \right)^m; \qquad m = 3....4, \tag{2}$$

where $n_0$ is the porosity, $w_R$ the residual water content and $k_0$ the saturated hydraulic conductivity ($w = n_0$). The suction $\psi$ of the matrix is a very strong function of water content, too. This can be shown considering the voids as channels of different cross-sectional radii. It is evident that the degree to which voids filled with wetting and no wetting fluid phases is a function of capillary pressure (suction). Normally, the wetting and re-wetting of the soil matrix follows along different $\psi$-curves, i. e. $\psi(w)$ is a hysteresis loop. $\psi$ can only be determined experimentally for the different matrix particles. The function $\psi(w)$ can then be obtained as a fit to the experimental curves. For watery clay which exhibits no hysteresis the fit provides

$$\psi(w) = \frac{0.66}{0.05 + w} - \frac{-2.44}{0.17 + w^2} + \frac{1.01}{0.09 + w^3}. \tag{3}$$

If the water potential h is chosen as the dependent variable from (1) using (3) the

differential equation

$$a(h)\frac{\partial h}{\partial t} = \frac{\partial}{\partial x}k(h)\frac{\partial h}{\partial x} + \frac{\partial}{\partial z}k(h)\frac{\partial h}{\partial z} + e(h) \tag{4}$$

is obtained. With h the transition from unsaturated into saturated state is a continuous process.

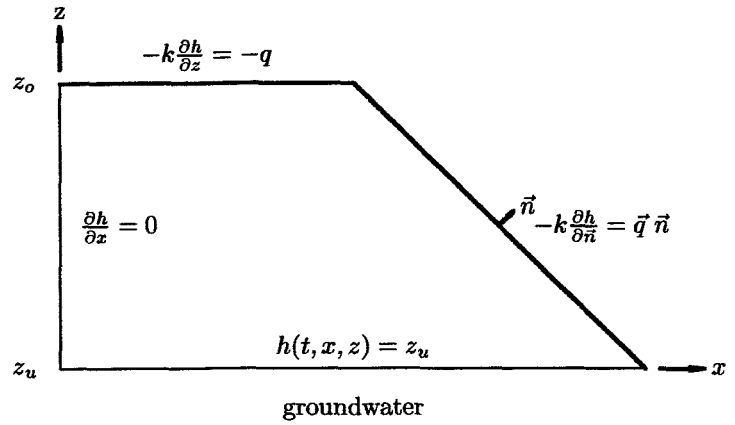


Fig. 1: Schematic representation of the flow domain with boundary conditions

For the geometry of figure 1 the Richards equation can be solved numerically. This geometry, schematically represents the cross section through a mining dump. The boundary conditions which result for the differential equation (4) are:
1. of Dirichlet's type for the plane $z = z_u$ separating the unsaturated zone from groundwater level ($\psi = 0$): $h(t,x,z) = z_u$.
2. of Neumann's type as far as slope and surface of the terrain are concerned $-k\frac{\partial h}{\partial \vec{n}} = \vec{q}(\vec{r}_{surf.},t)\vec{n}$, wherein $\vec{n}$ is the normal vector of the appropriate surface and $\vec{q}(\vec{r}_{surf.},t)$ the time dependent infiltration .

The spatial discretization of the differential equation (4) was performed according to

$$\begin{aligned} L(h_{i,j}) \;=\; & k_{i+\frac{1}{2},j}\frac{h_{i+1,j}-h_{i,j}}{\Delta x} - k_{i-\frac{1}{2},j}\frac{h_{i,j}-h_{i-1,j}}{\Delta x} + \frac{e(h_{i+1,j})+4e(h_{i,j})+e(h_{i-1,j})}{6} + \\ & k_{i,j+\frac{1}{2}}\frac{h_{i,j+1}-h_{i,j}}{\Delta z} - k_{i,j-\frac{1}{2}}\frac{h_{i,j}-h_{i,j-1}}{\Delta z} + \frac{e(h_{i,j+1})+4e(h_{i,j})+e(h_{i,j-1})}{6}. \end{aligned}$$

Time dependence is treated in the implicit form:

$$a(h)\frac{\partial h}{\partial t} \sim \left(\frac{a(h_{i,j}^{t+\Delta t})+a(h_{i,j}^{t})}{2}\right)\frac{h_{i,j}^{t+\Delta t}-h_{i,j}^{t}}{\Delta t} = L(h_{i,j}^{t+\Delta t}).$$

According to Luckner [1] the above implicit solution approach provides best results for such high degree nonlinear differential equations. The nonlinear system of equations with the discrete boundary conditions which results from the scheme of differences is solved by using a pointer matrix and the iterative Gauss-Seidel technique. As results of the calculation the volumetric water content and the flow rate $\vec{v} = -k(w)\ grad\ h$ (Darcy-velocity) are obtained in dependence on space and time. The water content and the flow rate are the essential quantities in the unsaturated zone where pollution release and transport are taking place. In figure (2) the result of a numerical test calculation is

shown for the following conditions:
1. The irrigation of the dump is assumed to be an odd (periodic) rectangle function of the period t=6 days.
2. Concerning the permeability of the matrix $m$ in relation (2) was selected as $m = 4$.
3. The test matrix should be homogeneous watery clay the water potential of which can be described by (3).

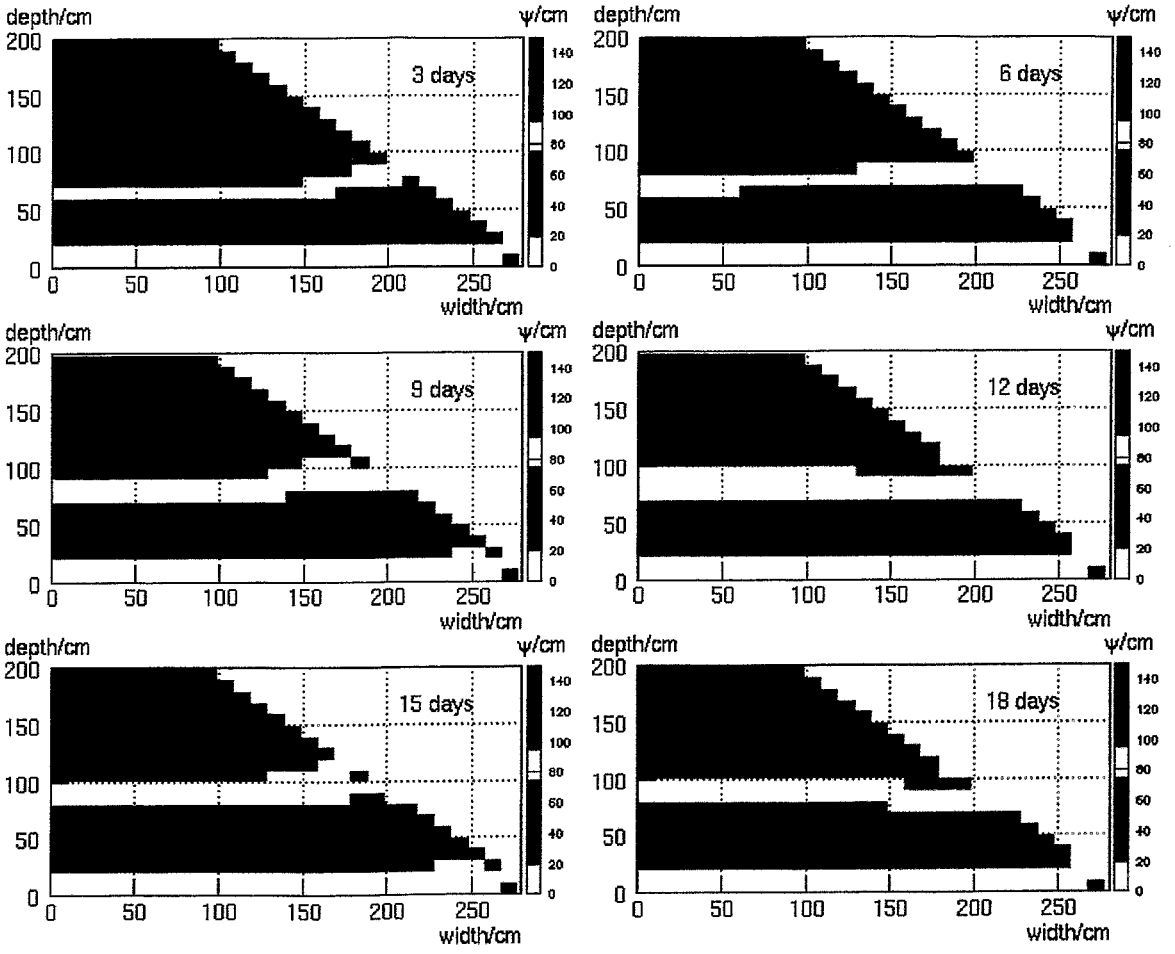


Fig. 2: Suction profiles in a dump caused by periodical irrigation

In figure 2 the water saturated zone is of white colour, the suction (capillary pressure) is equal to zero i.e. the pores of the matrix are completely filled with water ($w = n_o$, $\psi = 0\ cm$). The black colour represents the highest capillary pressure and in this way least water content in the pores. The total area was dry at the time $t = 0$ (black, initial condition, $\psi = 140\ cm$). Due to the strong sucking of the watery clay water from the aquifer zone rises into the dump body. This state is nearly stationary and adjusts quickly to the level determined by suction. Obviously, humidity penetrates deeper and deeper into the dump by periodical irrigation.
Concerning the symmetry plane $x = 0$ water motion behaved one-dimensional in the calculated period (18 days). For this reason it was possible to check the calculation against HYDRUS [2] results. There was complete agreement, deviations were smaller

than $10^{-2}$.

## 3. Transport Equation

As described above, in order to reach the aquifer, water from precipitation infiltrates through the ground surface and percolates downwards through the unsaturated zone. The same is true for pollutants carried with the water. These pollutants my be already present in the water reaching the ground surface or they may be added and removed to the water by dissolution, adsorption and chemical reactions along its path from the ground surface to the underlying aquifer. Simplified models for solute transport in the unsaturated zone lump the effects of several processes. This can be best illustrated in the one-dimensional convective-dispersive solute transport equation written as,

$$\underbrace{w\frac{\partial C}{\partial t}}_{storage} = \underbrace{-v\frac{\partial C}{\partial x} + \frac{\partial}{\partial x}(D\frac{\partial C}{\partial x})}_{transport} - \underbrace{\lambda C}_{decay} + \underbrace{q}_{source}, \tag{5}$$

where $w$ is the volumetric water content and $v$ is the Darcy-velocity (computed from Eq (1)). $C(x,t)$ is the solute concentration in $mol/l$. $x$ is distance in $m$. $D$ is an apparent dispersion coefficient in $m^2/h$. $\lambda$ is a first-order decay constant in $mol/h$, and $q$ is a production function in $mol/l/h$. The dispersion coefficient, $D$, can be related to micro-and macro- processes through the effective dispersion coefficient as $D = D_{diff} + \alpha_L|v|$, where $D_{diff}$ is the diffusion coefficient ($m^2/h$), $\alpha_L|v|$ is the dispersion coefficient and $\alpha_L$ the dispersivity ($m$). The exchange of a chemical species between

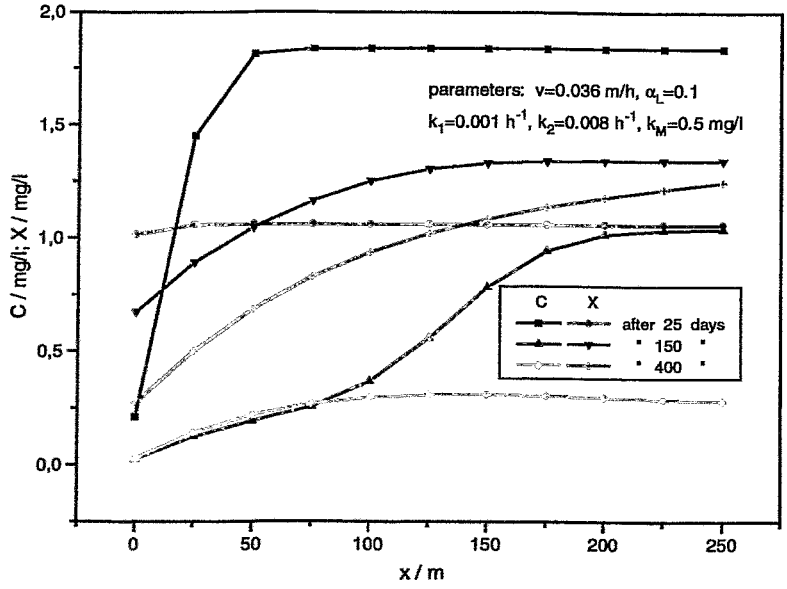


Fig. 3: Kinetic of bioconversion

the mobile ($C(x,t)$) and immobile phase ($X(x,t)$) is considered as an example for the transport equation (5): Mobilization of the pollutant shall be catalyzed by enzymes produced by microorganisms. The simplest model for this process is the Michaelis-

Menten kinetics:

$$\frac{\partial C}{\partial t} = -v\frac{\partial C}{\partial x} + \frac{\partial}{\partial x}(\alpha_L|v|\frac{\partial C}{\partial x}) - \lambda C - \frac{k_1 CX}{k_M + C} \tag{6}$$

$$\frac{dX}{dt} = \frac{k_2 CX}{k_M + C} - \Lambda_B X. \tag{7}$$

Where $X(x,t)$ is the biomass concentration, $\Lambda_B$ is its decay rate, and $k_1, k_2, k_M$ are constants. The time derivative was approximated numerically using the equation of van Genuchten and Gray [3]:

$$\frac{C^{t+\Delta t} - C^t}{\Delta t} = \frac{1}{2}\left[\frac{\partial C}{\partial t} - \frac{\Delta t}{6}\frac{\partial^2 c}{\partial t^2}\right]^{t+\Delta t} + \frac{1}{2}\left[\frac{\partial C}{\partial t} + \frac{\Delta t}{6}\frac{\partial^2 C}{\partial t^2}\right]^{t}. \tag{8}$$

where $\frac{\partial C}{\partial t}$ must be replaced by the spatial terms of the corresponding migration equation (6), and $\frac{\partial^2 C}{\partial t^2}$ by the derivatives of these terms ($\frac{\partial^2 C}{\partial t^2} \sim \left(\frac{v}{w}\right)^2 \frac{\partial^2 C}{\partial x^2}$ ). The results of the numerical calculation are shown in figure 3. In fact, when the component $C$ reduces the population of bacteria increases at first. After 150 days the concentration of bacteria is above the initial concentration of 1 $mg/l$ beginning with the 50-m mark. The concentration of $C$ and in this case the essential living conditions decreased by decay and the substance flowing off to the right which is described by the X-curve at the time t=400 days. The low concentration of $C$ at the surface $x = 0$ is due to the boundary condition $\vec{j} = vC - \alpha_L|v|\frac{\partial C}{\partial x} = 0$. The numerical calculation exactly represents the two boundary solutions which result for the decoupled differential equation system and the space independent case. An analytical solution is available for the decoupled transport equations. The just time-dependent differential equation system was compared with the Runge-Kutta-Fehlberg solution.

## References


[1] L. Luckner und W. M. Schestakow: Simulation der Geofiltration. Verlag für Grundstoffindustrie, 1975, Leipzig.

[2] J. B. Kool and M. Th. van Genuchten: Research Report No. 124, U. S. Salinity Laboratory, USDA, ARS, Riverside, CA

[3] M. Th. van Genuchten and W. G. Gray: Int. Journal of Numerical Methods in Engineering 12 (1978), pp. 387-404.

# NUMERICAL AND EXPERIMENTAL INVESTIGATIONS ON THE VIBRATION BEHAVIOUR OF A BOILING WATER REACTOR

**E. Altstadt, M. Scheffler, F.-P. Weiß, J. Runkel[1], U. Südmersen[1]**

## 1. Introduction

Many of the signals which are continuously measured during the operation of boiling water reactors (BWR) contain not only process information but also information about the vibration behaviour of the reactor pressure vessel (RPV) internals. This makes it possible to use these signals for the surveillance of the mechanical integrity, i.e. for early detection of component faults.

It is an important precondition for efficient vibration monitoring to have an adjusted theoretical model, which allows the physical interpretation of the measurements in such a sense that the measured resonance peaks can be assigned to the eigenfrequencies of the coupled mechanical system and that physically based thresholds for amplitude and frequency shifts can be determined. According to the state of the art such models are based on the finite element (FE) method [1].

The adjustment of the vibration model is carried out on the base of results from operational measurements and from vibration experiments during recommissioning. By means of the adjusted computational model sensitivity studies and the simulation of component faults can be performed. This is done by changeing certain parameters within the FE-model.

Such investigations contribute to the extension of the knowledge base for online vibration monitoring. Moreover, the FE-model is even suited for determining the dynamical component stresses caused by external loads (e.g. earthquake or explosion pressure wave).

## 2. FE-modelling of the reactor pressure vessel and its internals

### 2.1 Building a global vibration model

The theoretical modelling of a typical BWR pressure vesssel and its internals (Fig. 3) is done with the FE-code ANSYS®. The global vibration model comprises the RPV including the main circulating pumps (MCP), the control element drives, the core flux measuring pipes and the RPV internals. The internals which are considered in the model are

- shroud with upper and lower core structure
- fuel assemblies (FA)
- control element guide tubes

---

[1]Universität Hannover, Institut für Kerntechnik und Zerstörungsfreie Prüfverfahren

- steam separator
- steam dryer
- feed water distribution

The following elements are used for the idealization of the reactor structure: pipe elements *PIPE16* (considering the rotational inertia and the shear deflection), beam elements *BEAM4* (with a specific shear deflection coefficient for the back stream region of the shroud), mass elements *MASS21* (e.g. for the fluid) and stiffness matrices *MATRIX27* (connection and support of the main components). The elements of the stiffness matrices are determined by separate calculations with higher dimensional FEs (chpt. 2.2). Fig. 1 shows the topology of the global FE-model. To adjust the model to the measurements performed during a refueling it is necessary to include two operational states in the model:

- status special measurement (reactor cold, increased water level)
- status normal power operation

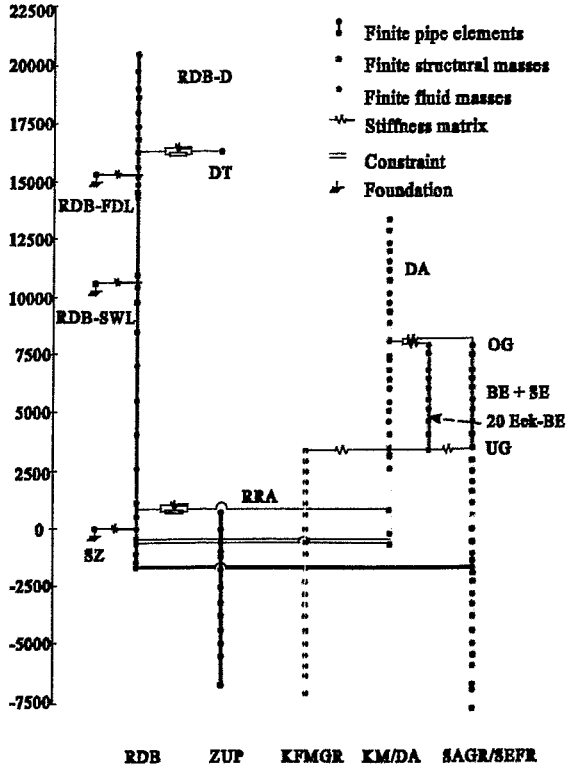


Fig. 1: Topology of the global FE-model

These two states differ especially in the temperatures and the coolant masses. The temperature dependence of the material properties of steel and zircaloy (fuel assembly jackets) can be considered in the model. The coolant is simply modeled by discrete masses (*MASS21* elements). For the power operation model the volumes, temperatures and densities following from the void fraction are taken from data sets of the thermohydraulics code ATHLET.

## 2.2 Separate calculations with local models

More complicate components that cannot be idealized by pipe or beam elements have to be modeled by higer dimensional FE (shell elements *SHELL63*, 3-D elements *SOLID73*). The results of such calculations are used for the initial determination of certain parameters of the global FE-model

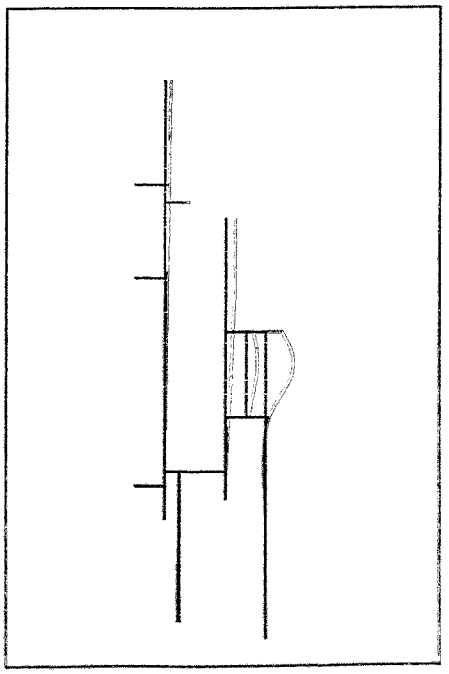

Fig. 2: Mode shape of the global FE-model at 6.5 Hz (assignment of components see Fig. 1)

(especially stiffness matrices). Separate calculations were performed for the RPV support frame, the upper and lower core structure, the back flow cover plate, the support elements of the steam dryer and for the bearing case of the MCPs.

To discriminate the bending modes from the shell modes of the experimentally found eigenfrequencies, the shell vibration modes of the RPV and the shroud were calculated using *SHELL63* and *SOLID73* elements.

### 2.3 Modal analysis with the global FE-model

Table 1 contains the vibrations modes of the adjusted global FE-model up to 30 Hz for both modeled states (special measurement during refueling, power operation). Additionally, the frequencies of the resonance peaks from the spectra of the special measurement are listed for comparison (chpt. 3).

**Table 1:** Eigenfrequencies (in Hz) of the global vibration model after adjustment and comparison with the experiment

| Mode-No. | FE-results | | Experiment | Vibration mode |
|---|---|---|---|---|
| | Special measurement | Normal power operation | | |
| 1 | 2.91 | 2.91 | 2.7 - 3.3 | Basic bending mode: control element drive |
| 2 | 6.36 | 6.53 | 6.5 - 6.7 | In-phase pendular motion: RPV / internals |
| 3 | 8.22 | 8.19 | 7.8 - 8.0 | Basic bending mode: MCP |
| 4 | 8.73 | 8.66 | 8.5 - 8.7 | In-phase pendular motion: RPV and shroud / steam separator, MCP anti-phase; anti-pahse vibration: FA / edge-FA |
| 5 | 10.09 | 9.32 | 10.0 -10.3 | Basic bending mode: edge-FA ; anti-phase vibration: RPV / MCP (small amplitude) |
| 6 | 11.89 | 12.93 | 11.0 - 11.3 | anti-phase vibration: RPV and shroud / stream separator; higher bending mode: edge-FA |
| 7 | 17.99 | 17.69 | 17.7 | Higher bending mode: control element drive ; higher bending mode: edge-FA |
| 8 | 25.09 | 25.24 | 24.0; 24.8 | Higher bending mode: control element drive |
| 9 | 27.00 | 29.05 | 25.0; 25.8 | Pendular motion: RPV; higher bending modes of the other components |
| 10 | 31.89 | 29.45 | | Higher bending mode edge-FA |
| 11 | 30.24 | 29.53 | 29.1 | Torsional vibration: RPV / internals |

For the adjustment of the model to the experimental frequencies mainly the elastic connections between the components are used. Fig. 2 shows the vibration mode 2 at

6.5 Hz as an example.

## 3. Experimental investigations

Vibration measurements were performed at the RPV of the BWR during a scheduled revision. At the time of the measurement the core was fully loaded and the RPV head was mounted. In comparison to the normal operation state the coolant water level was increased. The RPV was excited by an electrodynamic shaker and by an impact hammer. The vibrations were measured with a special temporary instrumentation consisting of 19 acceleration sensors.

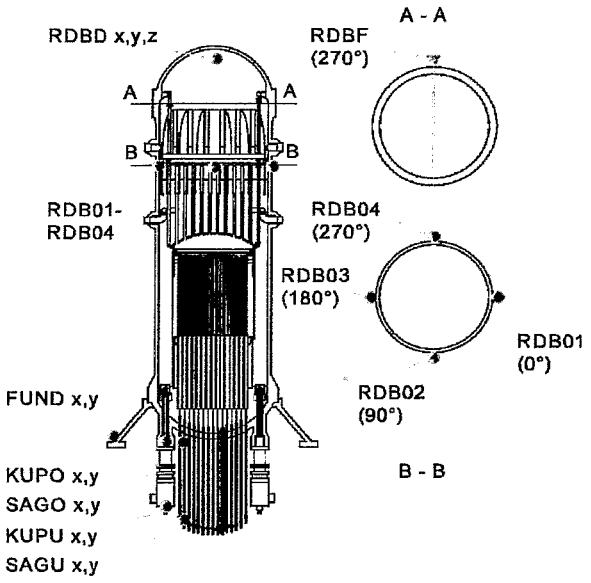


Fig. 3: Positions of the sensors of the special instrumentation

The point of excitation was at the flange of the RPV head. Fig. 3 gives an overview about the measuring positions at the RPV. Using the standard procedures of signal processing and modal analysis the eigenfrequencies and mode shapes in the range up to 30 Hz were extracted from the measurements. On this base the global FE-model was adjusted (see Table 1). Before and after the refueling operational measurements were performed using the standard instrumentation of the BWR (loose parts sensors, neutron flux detectors, pressure tranducers).
Fig. 4 shows the power spectra of an accelerometer for loose parts detection at the upper RPV flange at 180 ° before and after the refueling. The peaks marked by the vertical lines can be assigned to the eigenfrequencies of the modes 1 to 5 (see Table 1).

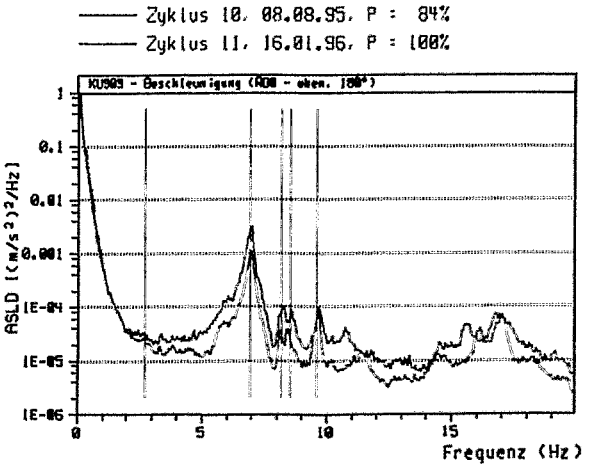


Fig. 4: Power spectra of an accelerometer for loose parts detection (upper RPV-flange, 180°) before and after refueling

## 4. Sensitivity studies

On the base of the adjusted computa-tional model sensitivity studies and the simulation of component damages can be carried out. For this purpose parameter changes which are typical for component failures are applied to the FE-model. Vibration signals that would be measured at the structure in this case are calculated with the modified model.

By means of harmonic analysis the detectability of damages can be evaluated. Within a harmonic analysis the steady state motion of the mechanical system is calculated with the excitation being a harmonic function at different frequencies. The harmonic analysis provides information about the dynamic behaviour of the system (amplitudes and phase relations). The global vibration model is subjected to a displacement excitation (amplitude $10^{-6}$ m in 45° direction) which approximately corresponds to the displacement noise measured.

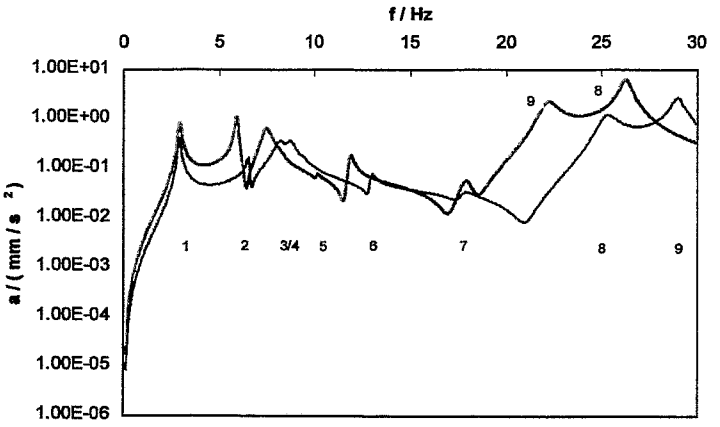


Fig. 5: Change of the acceleration spectrum x-direction control element drive with decreased stiffness of the RPV support frame (power operation). Continuous curve: normal state, dashed curve: decreased stiffness.

This excitation was applied to the three most important coupling points with the rector building (RPV support frame, steampipes, feed water pipes). For the calculation a sliding sine from 0Hz up to 30 Hz with 400 frequency lines was used.

Fig. 5 shows for example the calculated spectrum of the acceleration of the control element drives in x-direction for normal state of the reactor (blue curve) and for a hypothetical decrease of the RPV support frame (red curve). A significant shift of the resonance peaks of the 2nd, 3rd, 4th, 6th, 8th and 9th eigenfrequency can be seen. Moreover, the resonance peak of the 2nd eigenfrequency exhibits a significantly increased amplitude. The shift the 9th eigenfrequency is such large that this frequency sinks below the 8th eigenfrequency.

**References**


[1] Altstadt, E.; Grunwald G.; Scheffler M.; Weiß, F.-P.: Analytische Modellierung mechanischer Schwingungen von Primärkreiskomponenten des Druckwasserreaktors WWER-440 mit finiten Elementen. Abschlußbericht zum BMBF-Förderprojekt Nr. 1500916, Forschungszentrum Rossendorf, Juni 1996

[2] Grunwald, G.: Berechnung der Eigenfrequenzen der Biegeschwingungen von RFR-Wärmeübertragerrohren an Luft und im Wasser einzeln und im Bündelverband, ZfK Rossendorf, Bereich Reaktorphysik, 1989

[3] Fischer, D.; Steiner, H.: Zur Ermittlung der mitwirkenden Flüssigkeitsmasse bei der Eigenschwingungsberechnung flüssigkeitgefüllter Zylinderschalen, Ingenieur-Archiv 44, Springer-Verlag 1975

[4] Altstadt, E.; Scheffler M.; Weiß, F.-P.: Theoretische Modellierung des Druckbehälters und der Druckbehältereinbauten eines SWR. Abschlußbericht zum BMBF-Förderprojekt Nr. 01TS9432, Forschungszentrum Rossendorf, August 1996

# A CYLINDRICAL PENDULUM VIBRATING IN AN AXIAL ANNULAR INCOMPRESSIBLE FLOW - A NUMERICAL APPROACH

**J. Zoller**

## 1. Presentation of the problem

The subject of this investigations are motions of the pendulum sketched in the Figures 1 and 2: The fixed outer cylinder A with radius $R_A$ contains the inner cylinder B which can perform small pendular motions around the $y$-axis as the rotation axis. In between the cylinders an external pressure gradient $(p_1 - p_2)/L$ $(-\vec{e}_z)$ drives the basic flow $\bar{u}_z$ of an incompressible fluid with density $\rho$ and molecular dynamic viscosity $\mu_0$. The elongations of the inner cylinder are small in comparison with the gap width $S$: $=R_A - R_B$ with $R_B$ denoting the radius of cylinder B. The length of the cylinders is $L$. At rest the two axes of the cylinders coincide with the $z$-axis.

The two cylinders A and B are assumed to be rigid bodies. The force driving the pendulum B back into its rest position ($\psi = 0$) can be increased by a spring with spring constant $C$.

The presented problem is a special case of the system investigated by Grunwald and Altstadt [1]. The task is to perform a numerical investigation of the motion of pendulums of the presented type. The purpose of the investigation is a comparison of the numerical results with the analytical results of Grunwald and Altstadt [1].

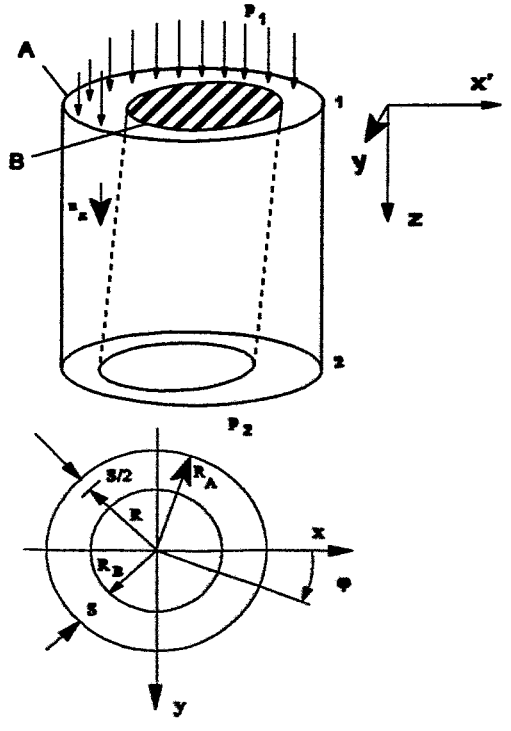


Fig. 1: Geometry of the system.

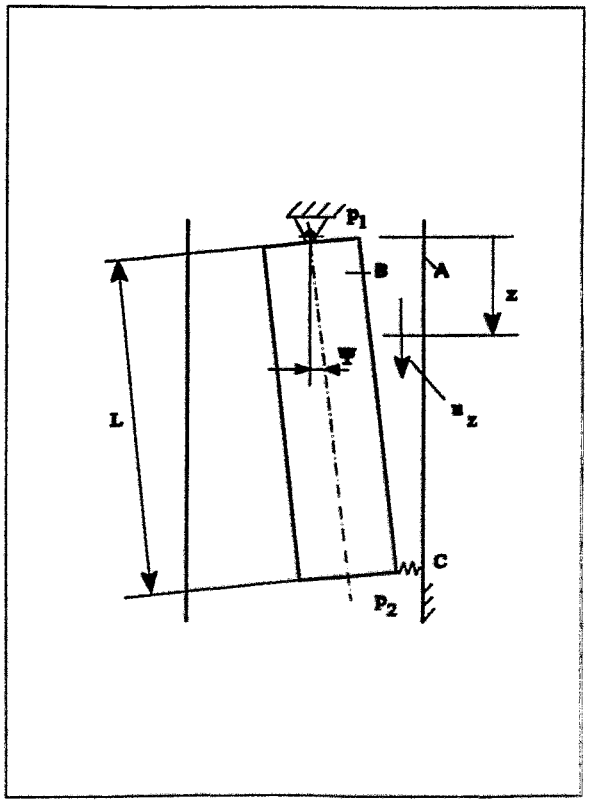


Fig. 2: Mechanical scheme of the system.

The governing equations of the system can be separated into three groups:
(i) The equation of motion of the pendulum.

$$\Theta \frac{d^2\psi}{dt^2} + D_s \frac{d\psi}{dt} + \left( \tilde{m}\, g\, \frac{1}{2} L + C \right) \psi = X. \qquad (1)$$

$X$ denotes the torque being exerted on the pendulum by the fluid, $\Theta$ the moment of inertia, $D_s$ the damping constant due to the hinge, $\tilde{m}g$ the gravitational force on the pendulum reduced by the buoyancy.
(ii) The governing equations of the motion of the fluid are the Navier-Stokes equation, the incompressibility constraint and the boundary conditions. The Navier-Stokes-Equations describe the evolution of velocity field of the fluid in time. Written in cylindrical coordinates but in different formulations these equations can be read in the references [2, 3]. The results presented here were obtained from the arbitrary Lagrangian-Eulerian formulation of the Navier-Stokes-Equations [4]. On the jackets of the cylinders no-slip conditions hold. In the plane with $z \equiv L$ the pressure in the fluid has the constant value $p_2$[5], in the plane with $z \equiv 0$ the fluid pressure has the constant value $p_1$ at every time. It is not clear whether this last boundary condition at $z \equiv 0$ meets the physical reality. However, a deviation from this boundary condition hardly influences the results provided that the deviation is not too large.
(iii) The balance of forces on the jacket of the movable cylinder B [3, 4]. This equation expresses the interaction between the motions of the fluid and the rigid body.

## 2. Spatial discretization of the fluid equations

In order to transform the governing equations into discrete equations a hybrid spectral/Finite Element method was applied [3]. As an approximation of the velocity and the pressure fields in the fluid, the dependence of these fields on the circumferential coordinate is expanded in a truncated Fourier series. The dependence of the velocity field on the radial and axial coordinate is approximated by a sum of bilinear Finite Element shape functions (bilinear quadrilaterals). In each Finite Element the shape functions of the pressure field are constant [6].

The streamline upwind/Petrov-Galerkin (SUPG) formulation from reference [7] was slightly modified in order to make this method applicable to a hybrid spectral/Finite Element method [3].

## 3. Turbulence model for narrow gaps

In the case $S \geq 0.2(1/2)(R_A + R_B)$ only laminar flows can be calculated. In the case $S \leq 0.1(1/2)(R_A + R_B)$ turbulent flows are modelled by adding a viscosity $\mu_t \geq 0$ to the molecular viscosity $\mu_0$ according to Prandtls mixing length hypothesis [8]. At a certain point in the fluid domain the turbulent viscosity $\mu_t$ is a function of both the Reynolds number and the distance to the wall. The spatial dependence of $\mu_t$ is implemented according to empirical formulas of Nikuradse [9] and van Driest [10].

## 4. Time integration

The time integration of the discrete equations is performed employing a predictor-multicorrector method described in reference [4].

## 5. Results

The numerical procedure sketched in this article was put into action in a Fortran code which was given the name `FSIGAP'. In reference [1] an experimental setup of a pendulum in water is described. In the Figures 3 and 4 results of `FSIGAP' (f numerical, D numerical) are compared with measurements of ref. [1] (f experimental, D experimental) and the analytical results of ref. [3] (f analytical, D analytical) which are based on ref. [1]. In the analytical formulas of ref. [1] the boundary conditions are slightly different from that in `FSIGAP'. Therefore also the analytical results of ref. [1] combined with the added stiffness effect from ref. [11] are depicted ( f analytical alternative boundary conditions).

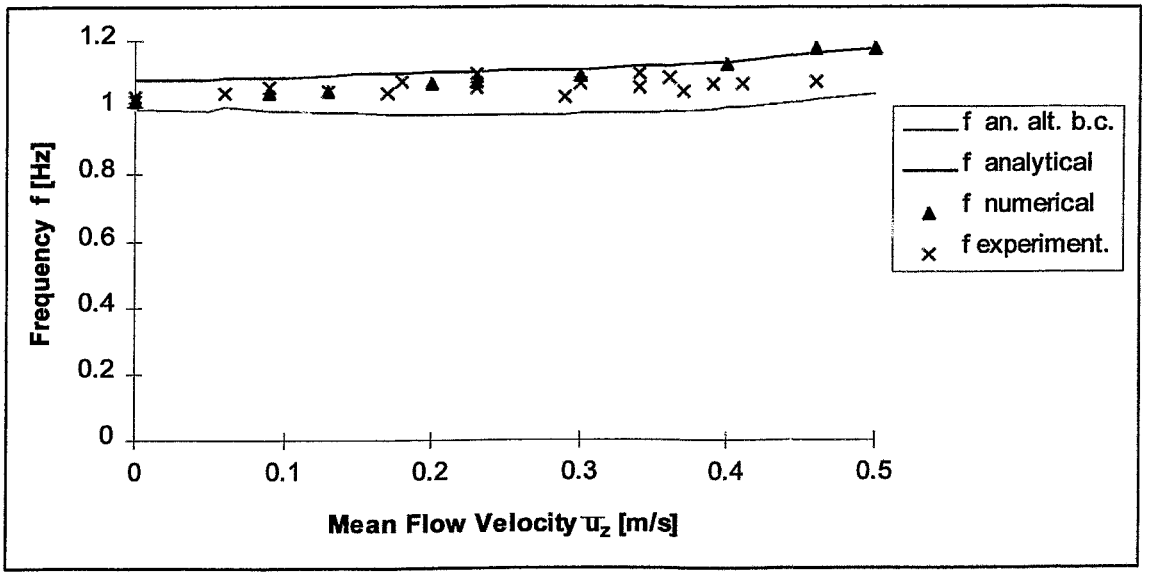


Fig. 3: Eigenfrequencies of a pendulum in water.

The experimental setup corresponds to the scheme in Fig. 2. The experiments were characterized by the following main parameters: Moment of inertia of the pendulum with respect to the hinge $\Theta = 0.445 \cdot kg\ m^2$ ; mass of the pendulum $m_B = 8.65 kg$ ; mean radius of the two cylinders $R = 5.16 \cdot 10^{-2} m$ ; gap width $S = 3.1 \cdot 10^{-3} m$ ; length of the pendulum $L = 0.392\, m$ distance between the hinge and the center of gravity of the pendulum $l_s \approx L/2$.

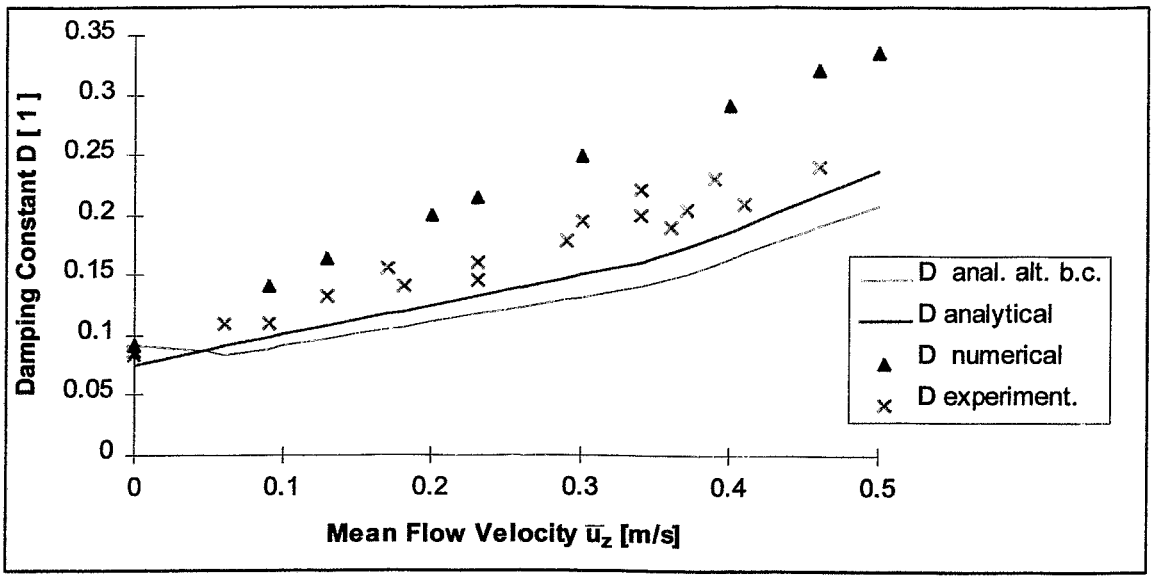


Fig. 4: Dimensionless damping constants of the pendulum in water for different flow velocities.

For the same pendulum but over a wider velocity range Fig. 5 compares numerical values of the eigenfrequencies with the analytical approximation in ref [3].

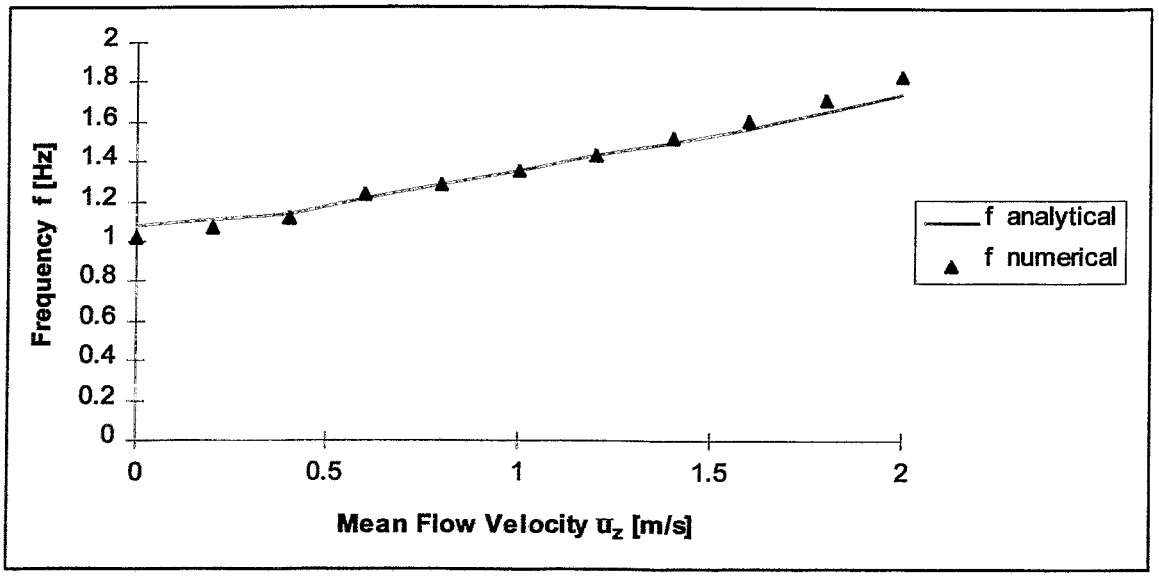


Fig. 5: Numerical and analytical values of the eigenfrequencies of the pendulum in water.

## 6. Conclusions

The Fortran program 'FSIGAP' confirms in principle the validity of the analytical results of Grunwald and Altstadt in ref. [1] and of the result of Zoller in ref.[11], which were used to integrate fluid-structure-interaction into a vibration model of a VVER reactor. Limitations of the validity of the analytical results can be investigated by parameter studies.

## References


[1] Grunwald G., and E. Altstadt
"Analytische und experimentelle Untersuchungen zur Modellierung der Fluid-Struktur-Wechselwirkung in einem 2D-Ringspalt."
Report FWSM - 1/93, Research Centre Rossendorf, Institute for Safety Research, Departement for Mechanical Integrity.

[2] Perotin L., and S. Granger
"A numerical model for fluid-structure-coupling of a confined cylinder submitted to an axial annular flow."
The Winter Annual Meeting of the ASME, Anaheim, CA, Nov. 8 -13, 1992. In: PVP-Vol. 244, Int. Symposium on Flow-Induced Vibration and Noise - Vol. 5,, pp. 1-16. ASME, 1992. Eds: M.P. Païdoussis and M.K. Au-Yang.

[3] Zoller J., PhD-thesis, in preparation.

[4] Nomura T., and T.J.R. Hughes
"An arbitrary Lagrangian-Eulerian finite element method for interaction of fluid and a rigid body."
Comput.Methods Appl. Mech. Engrg. 95, (1992), pp. 115-138.

[5] Grunwald G., W. Zimmermann, and J. Zoller
"Experimentelle und theoretische Untersuchungen an einem Pendel-Luft-Modell."
Report, Reasearch Centre Rossendorf, Institute for Safety Research, Departement FWSM, in preparation.

[6] Thomasset F.
"Implementation of Finite Element Methods for Navier-Stokes Equations."
Springer, New York, 1981.

[7] Brooks A.N., and T.J.R. Hughes
"Streamline Upwind/Petrov-Galerkin Formulations for Convection Dominated Flows with Particular Emphasis on the Incompressible Navier-Stokes Equations."
Comput.Methods Appl. Mech. Engrg. 32, (1982), pp. 199-259.

[8] Prandtl L.
"Über die ausgebildete Turbulenz."
ZAMM, 5, (1925), p.136.

[9] Nikuradse J.
"Gesetzmäßigkeiten der turbulenten Strömung in glatten Rohren."
VDI Forschungsheft 356, VDI-Verlag, 1932.

[10] van Driest E.R.:
"On Turbulent Flow Near a Wall."
J. Aero. Sci, 23, (1956), pp.1007-1011 and p. 1036.

[11] Zoller J.
"Added Stiffness Relating to Small Motions of Two Concentric Cylinders Submitted to Axial Annular Incompressible Flow."
Research Report FZR-146 of the Research Centre Rossendorf, 1996.

# EARLY FAULT DETECTION IN CHEMICAL SEMIBATCH REACTORS

**G. Hessel, W. Schmitt, N. Tefera, K. van der Vorst, F.-P. Weiß, J. Neumann[1] and S. Schlüter[1]**

## 1. Introduction

The early detection of faults is of particular importance in the safe and economical operation of chemical plants. If potentially hazardous situations are recognized by the personnel in due time, it may be possible to take the necessary counter measures to avoid temperature and pressure excursions which might result in thermal explosions and in the release of the reaction mixture or even in the destruction of the plant. As accident analyses show, in particular batch and semibatch reactors are endangered because a wide range of processes are carried out in those reactors, and very often they involve transient operation conditions due to the discontinuous process control.

Therefore, on-line supervision methods are to be developed for the early detection of dangerous process states in the framework of a joint project. For this purpose different faults are investigated in a laboratory reactor. The objective of the experiments is to find efficient features for classifying faults, to verify the dynamic process simulation software, and to test supervision methods based on neural networks.

## 2. Experimental

The safety relevant experiments were carried out in a laboratory reactor at Oberhausen [1]. The main part of this plant is a computer-aided reaction calorimeter (RC1 of Mettler-Toledo) with a steel vessel (HP60: 1.8 litre, 60 bar) and a jacket cooling. Figure 1 shows the stirred reactor vessel and its peripheral units such as feed tanks (B), balances (W), pumps (P), the level indicator (PI56) and the product tank (B7). In order to avoid faulty dosing of reactants, valves (V) and back pressure valves (RS) were used in the feed pipes. The reactants can be preheated using the heat exchangers (WT) installed in the feed pipes. For controlling the temperature of the reactor (TIR52) or of the jacket (TIR53) and the feed temperature of the reactants (WIRC), the control unit (RD10) of the RC1 was used.
For in-pile measurement of process parameters and their fluctuations a special measuring probe was inserted into the laboratory reactor (Fig. 1). It allowed to measure the temperature and pressure of the reactor content at different positions. For example, two NiCr-Ni-thermocouples (diameter: 0.5 mm), one PT100-resistance thermometer, and one dynamic pressure sensor were installed at different heights. The signals of the measuring probe and of the RC1 instrumentation were simultaneously acquired and processed (Fig. 1). In the present development phase the neural-network-based supervision system works off-line, i.e. the data sets are transferred manually by means of a disc from the RC1-measuring and control system to a special PC and then the data are sent via Internet to the supervision system at Rossendorf.
The data transmission to the host computer at Rossendorf was carried out using the

[1] Institute for Environmental, Safety and Energy Technology Inc., Oberhausen

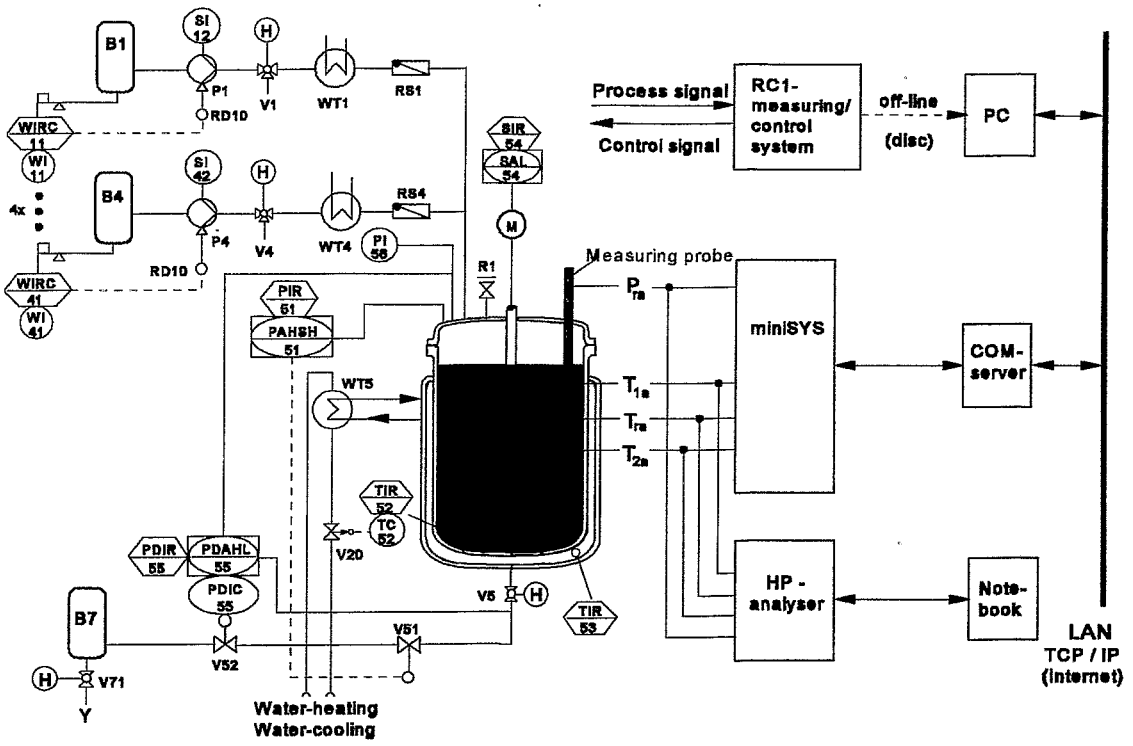


Fig. 1: Scheme of the laboratory reactor and the data acquisition system

signal processing unit miniSYS and a COM server that is connected to the Internet. The miniSYS consists of a communication control board (MSKOP) and up to eight signal processor boards (MSDSP) each being equipped with two analog inputs and outputs. All MSDSPs contain one digital signal processor and memory. So in each board, the signal acquisition and processing, the feature extraction as well as a decentralized preliminary classification based on neural networks could beperformed on a first level. The main tasks of the MSKOP are:

- to communicate with the host computer,
- to transfer data to the host computer, and
- to carry out the second level classification.

For that the neural networks will have to be externally trained before they are implemented in the miniSYS. The objective is to use the miniSYS as a decentralized supervision device in industrial plants.

## 3. Experimental simulation of faults and failures

For assessing the safety of a chemical plant during a fault, it is necessary to know whether there is a potential hazard so that an accident could be initiated by a fault or a failure when appropriate counter-measures will not be taken by the personnel. In this context, fault is defined as an unpermitted deviation of at least one characteristic variable of the system from the acceptable (standard) value, while the term failure characterizes a permanent interruption of a systems ability to perform a required

operational function.

To investigate the effects of different faults or failures at an exothermic reference process, namely the catalytic esterification of acetic anhydride with methanol in a laboratory reactor, a number of possible causes of these disturbances were simulated experimentally, e.g. loss of cooling, loss of agitation (stirrer failure), inappropriate feed rate of reactants, inappropriate concentration of catalyst, different reaction temperatures, etc. To diminish the risk of a serious runaway reaction, this strongly exothermic reaction was accomplished in a semibatch process instead of a batch process. In particular at the beginning of a batch process, the risk of a runaway reaction is very high when a critical fault occurs, because the reactor contains the total mass of the reactants at that time.

In this work the effects of the stirrer failure are examined closely because its potential hazard to cause a dangerous stage is underestimated in general. Figure 2 shows the influences of a stirrer failure on the temperature and pressure profiles in the reactor.

During this process, initially acetic anhydride and sulfuric acid (catalyst) were added to the reactor vessel, and then by stirring they were heated up to the start temperature and were tempered at 40 °C. After some time, the impeller of the stirrer was disconnected and methanol was then charged into the reactor vessel over 20 min (ME-dosage in Fig. 2). During the stirrer failure (10 min), there is no mixing between methanol and acetic anhydride with catalyst due to the lower density of methanol. Therefore without mixing, a stratification establishes with the acetic anhydride below the methanol. The reaction product is deposited between those two reactants.

As shown in Fig. 2 by the temperature signals Tra (PT-100) and T2a (thermocouple at the bottom of the probe, see Fig. 1), practically there is no reaction without intermixing. However, the increase of temperature by about 15 K, measured by the thermocouple T1a which was 7 mm below the interfacial area, indicates that an exothermic chemical reaction has obviously occurred at the vicinity of the interfacial area between methanol and the reaction mix (acetic anhydride with catalyst). An increase of the reactor pressure by 1 bar was also observed. After that the temperature T1a decreases slowly due to the formation of a non-reactive layer (product) which hinders the methanol to diffuse into the co-reactant. After dosing methanol over 10 min without intermixing, the impeller was reconnected and the agitation was restarted at 200 rpm. Consequently, the large amount of the accumulated methanol was ransformed within about 20 s (see Fig. 2). Obviously, there is an acceleration of the reaction rate at the interfacial area where a maximum temperature of 143 °C is observed, in spite of the maximum global temperature was only 79 °C during restarting the stirrer.

Moreover, the rapid increase of the pressure to about 4.5 bar indicates that a significant generation of gas occurs simultaneously. Because of the mixing of the cold and hot liquids of the different zones and due to the increasing the cooling capacity, a runaway reaction was avoided in this case. However, such an accumulation of reactants is a frequent cause for a runaway reaction if a critical fault ensues [2].

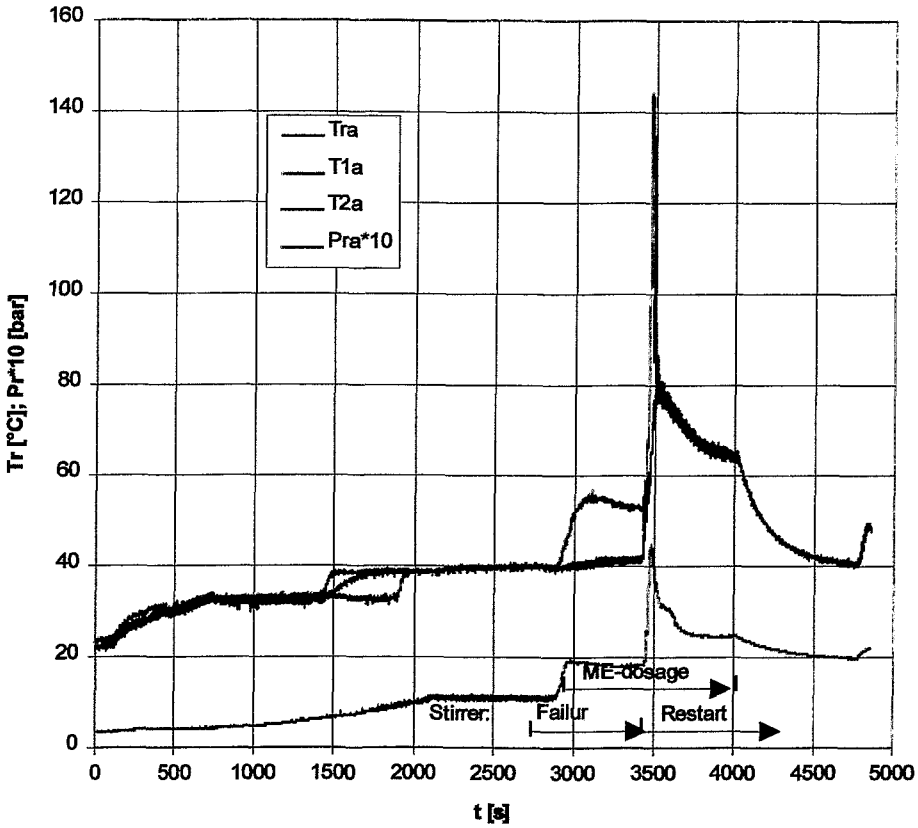


Fig. 2 Profile of the axial reactor temperatures and the pressure during failure and restart of the stirrer (set point 40 °C)

Combinations of the stirrer fault and other faults such as an increasing of feed rate or a deviation from the optimum isoperibolic temperature by 12 K during adding methanol were investigated. An optimum isoperibolic temperature is defined as the temperature at which a minimum reaction temperature would be reached if a cooling failure (loss of cooling) exists [3]. Because of an increased accumulation of the reactants, both combination faults mentioned above resulted in an increase of the reaction temperature by 10 K in comparison with the stirrer fault alone.

## 4. Comparison between experimental and simulated results

In order to have a reliable tool for process optimization and safety assessment as well as for developing and for testing the supervision method, it is very important to validate the dynamic process simulation software. For this purpose, the experimental results from the laboratory reactor (RC1) were compared with the simulation results which are calculated using the RC1-simulator of the BATCHCAD software.

Figure 3 shows the experimental and numerically simulated profiles of the reactor temperature during an isoperibolic semibatch process without any disturbances (set point 28 °C). After adding methanol and after intermixing, the reactor temperature increases rapidly due to the heat generation by the strongly exothermic reaction. The

temperature profile calculated by the RC1 simulator (Tr,model) is in relatively good agreement with experimental data (Tr,exp) for the reaction enthalpy $\Delta H_r$ = - 65 kJ/mol [4]. A similar good result was obtained by the CASI simulator (UMSICHT Oberhausen) after using the same value of the reaction enthalpy and a corrected flow rate of the

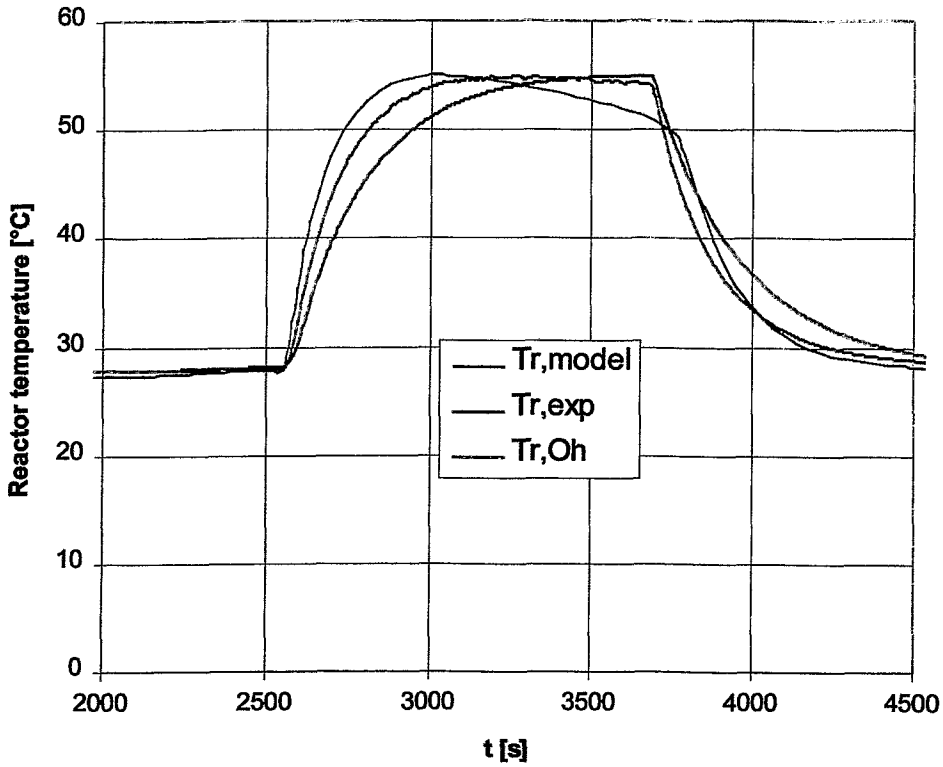


Fig. 3: Experimental and numerically simulated profiles of the reactor temperature of a normal semibatch reaction (set point 28 °C)

coolant (see Tr,Oh, Fig. 3).

It is impossible to simulate correctly the stirrer fault using the BATCHCAD simulator which assumes a homogeneous reaction mixture. To estimate the sudden temperature jump during the stirrer restart, it was assumed that the amount of accumulated methanol will be charged into the reactor within about 20 s. Temperature profiles of the experimental and two numerically simulated results during dosing methanol at a set point of 40 °C are depicted in Fig. 4. The maximum temperature (Tr,vak = 160 °C) estimated by entirely adding the accumulated methanol at the restart of agitation within 20 s is higher than the temperature (T1a = 143 °C) measured by the thermocouple in the vicinity of the interfacial area.

However, as shown by in-pile-measuring the temperature (T1a), obviously part of the accumulated amount of methanol has already been consumed at the interfacial area during the stoppage of the stirrer (see T1a in the time period from 2900 to 3400 s, Fig. 4). If one assumes only 50 % of methanol were accumulated till the restart of the agitation, then the temperature profile Tr,tak is obtained with the maximum (112 °C)

below the experimental value of the local temperature of 143 °C. The simulated temperature drops slowlier than the measured one. This is obviously caused by the assumption of complete mixing in the simulation so that there are no cold and hot zones in the reaction mixture. In praxi due to the intermixing with the cold liquid, the temperature of the hot zone decreases faster and consequently the reaction rate is also faster reduced than that of the model.

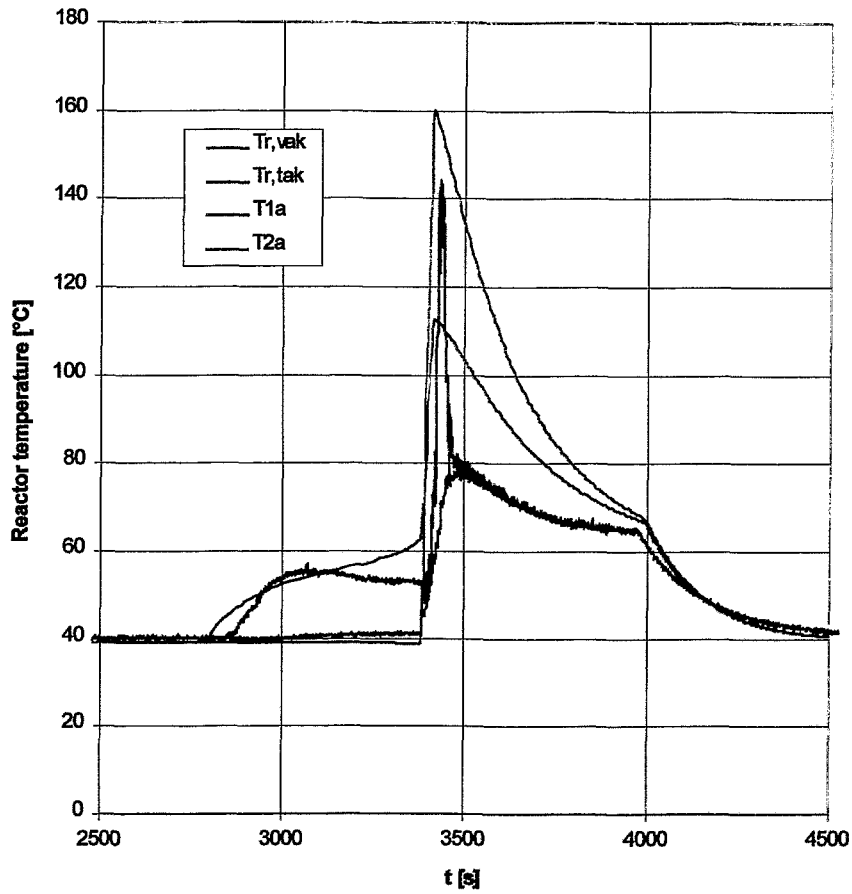


Fig. 4: Comparison between measured and simulated reactor temperatures (RC1 simulator) during failure and restart of the stirrer

## 5. Fault detection using neural networks

The efficiency of neural networks to recognize faults in technical plants has experimentally been proven. For example, the method was described in detail in [5]. For identifying dangerous process states, the neural network first has to be trained by process data from normal conditions and from faulty states which can be simulated in the laboratory reactor. To form an appropriate input vector of the neural network, features were extracted from both the process signals (filling height, feed temperatures, valve positions, number of revolutions of the stirrer, pressure, feed rates, temperatures of reactor vessel, jacket and of the coolant, etc) and from calculated

values of the RC1-measuring/controlling-computer (e.g., thermal capacity and volume of the reaction mass, heat of reaction and reactor-temperature gradient).

To avoid multiple networks each for a special set point of temperature or pressure, all features are normalized by relating the different features to the normal process state. For example, temperatures were normalized as relative deviation from their normal set point. Furthermore, all features of the input vector were normalized into the range from 0 to 1.

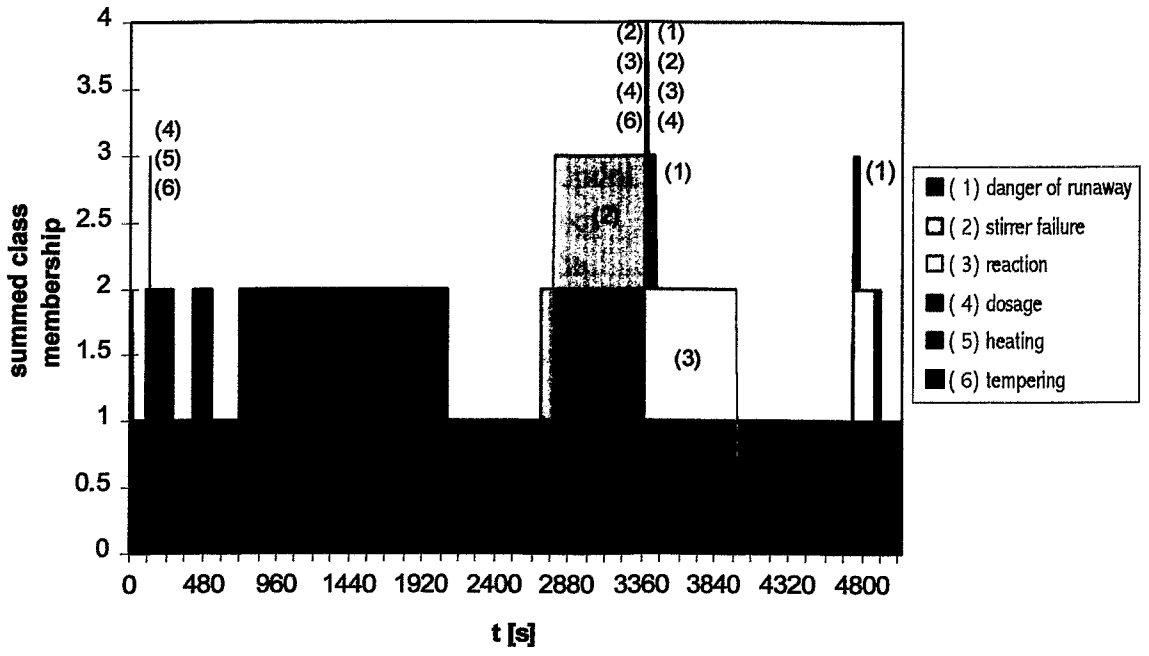


Fig. 5: Expert classification of the semibatch reaction with stirrer failure

To classify even faulty process states which simultaneously involve more than one fault, the neural networkhad to be modified regarding the defined state classes and the display of the classification results. For this purpose, a summed class membership was introduced (see Figs. 5 and 6).

Figure 5 shows all process states of a semibatch reaction which were used for training. The interval during the failure and the restart of the stirrer (2700-3400 s) is the most important one. While the stirrer is off (class 2), the dosage of the methanol starts (class 4). Due to the absent intermixing, there is no reaction heat to be removed by the cooling system. Therefore, the class 6 is active up to the moment of stirrer restart. Then the reaction starts suddenly and produces a lot of heat. This activates the classes 3 (dosage/reaction) and 1 (danger of runaway). At the end of the experiment (t = 4800s), the pipes were cleaned with acetic anhydride for safety reason. Therefore, some reaction takes place and so the classes 1, 3, and 4 become active.
A neural network (24/4/18) trained with these process data is capable of classifying the trained data very well (no figure). Due to the generalization capability, the neural network can also classify unknown process courses with different set points. Figure 6

shows the classification of a process with the temperature set point at 28 °C. That means the normalization of the temperatures described above works well for a semibatch reaction.

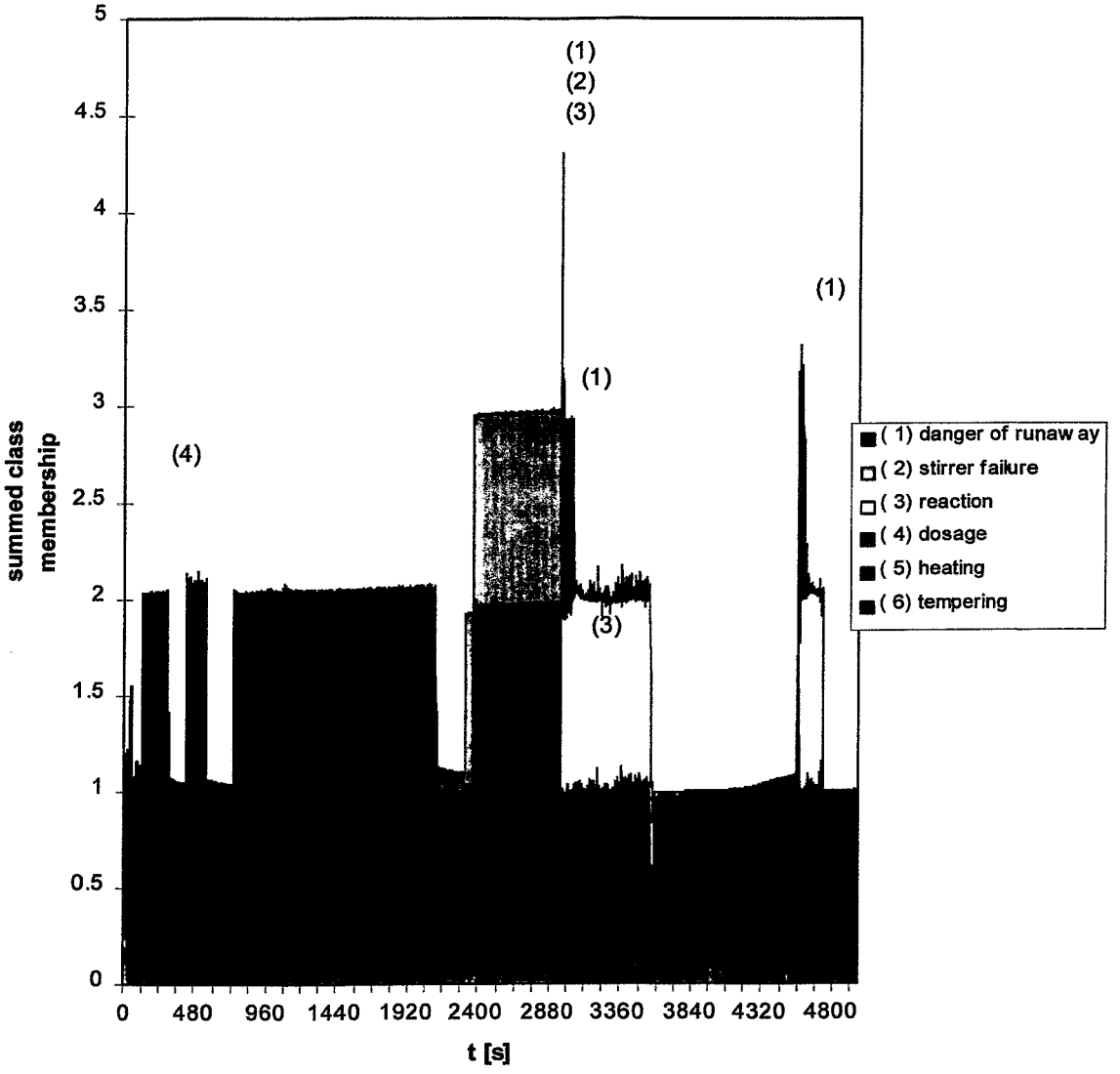


Fig. 6: Classification of an untrained process course with a stirrer failure (set point 28°C) by a perceptron network

Due to the nature of measuring signals, the membership to the clsses can differ from one time step to the next one, particularly at the second appearance of class 4 (dosage) because the pump has to charge very small amounts of the catalyst with single pump lifts. The resolution in Fig. 6 cannot reproduce this and so it shows only a black area at 480 s. The critical situation during stirrer fault, the further methanol dosage, and the stirrer restart, here there exists a danger of runaway, is classified very well. Even if the methanol is charged twice as fast as under the normal condition, all process states are assigned correctly.

## 6. Conclusions

For assessing the safety of chemical semibatch reactions, the importance of the experimental simulation of faults could be proven. In particular, the investigation of stirrer faults has shown that even in small reactor vessels there is a non-uniform axial temperature profile which, due to the accumulation of reactants, leads to a potential hazard. In this case, human errors or severe technical faults (e.g., loss of cooling) could initiate a runaway reaction if strongly exothermic chemical reactions are carried out in semibatch or batch operation.

The often occurring stirrer faults were not capable of being correctly simulated by the dynamic process simulator because the point-kinetics is no appropriate approximation. When training the experimentally simulated data, the stirrer fault was correctly classified by the perceptron network. Further investigation showed that for training the neural network both data from the process simulator and experimental data should be used. To improve the identification of dangerous process states in industrial plants, the concentration values and the temperature distribution should additionally be monitored in the reaction mixture.

## References


[1] J. Rabe
Experimentelle Untersuchungen zur Gefahrenabschätzung bei exothermen Reaktionen
Diplomarbeit Universität Dortmund, 1996

[2] O. Klais, U. Wörsdorfer, F. Westphal
Thermochemische Untersuchungen zum Störfall Griesheim
Chem.-Ing.-Tech. 66 (1994) Nr. 9, S. 1165-1176

[3] J. Steinbach
Methodische Vorgehensweise bei der sicherheitstechnischen Beurteilung exothermer Reaktionen
Praxis der Sicherheitstechnik, Vol. 3, DECHEMA, 1995, S. 61

[4] G. Wehmeier
Forsch.-Ber. VDI Reihe 3 Nr.373
Düsseldorf, VDI-Verlag 1994

[5] G. Hessel, W. Schmitt and F.-P. Weiß
A Neural-Network Approach for Acoustic Leak Monitoring in Pressurized Plants with Complicated Topologies
Control Engineering Practice, **4**, 9 (1996), pp. 1271-1276



*The project this report is based on is funded by the BMBF (Bundesministerium für Bildung, Wissenschaft, Forschung und Technologie) and is registered with No. 01RG94235.*

# FLOW CONTROL BY MEANS OF ELECTROMAGNETIC FORCES

**G. Mutschke, T. Weier, G. Gerbeth**

## 1. Introduction

In many fields of fluid mechanics it is desirable to control the flow field in order to achieve certain beneficial goals, such as mixing enhancement, drag reduction, separation prevention, suppression of instabilities, etc. Examples can easily be found in many areas of daily life and are of immense technological importance. Flows of electrically conducting fluids offer the attractive opportunity of contactless control due to the Lorentz force

$$\mathbf{f} = \mathbf{j} \times \mathbf{B} \tag{1}$$

if electromagnetic fields are applied. Here **B** denotes the magnetic field, and **j** denotes the electric current density, which is defined from Ohm's law as

$$\mathbf{j} = \sigma (\mathbf{E} + \mathbf{v} \times \mathbf{B}) \tag{2}$$

where $\sigma$ is the electric conductivity of the fluid, **E** is the electric field, and **v** is the velocity field of the flow. Additional attractive features of the Lorentz force for controlling a flow field are:

- The Lorentz force, externally applied, can be controlled readily in direction and magnitude as well as in space and time.
- No moving parts are involved.
- The Lorentz force is a body force, which means it could be applied at a distance: instead of pushing at the edges of a fluid stream, the force grabs it in midstream.
- If done right, the energy expenditure could be kept at a minimum, improving the efficiency of the flow control device.

In most cases as described below (excluding astrophysical phenomena) the induced magnetic field can be neglected, i.e. **B** denotes the externally applied magnetic field, and the Maxwell equations decouple from the flow problem described by the Navier-Stokes equation. One can further distinguish between induced and externally applied currents. Induced currents are due to the motion of the fluid and due to induced electric fields. Introducing a scalar electric potential $\Phi$ as gradient of the induced electric field, $\Phi$ can be determined from the Poisson equation

$$\Delta \Phi = \mathrm{div}\,(\mathbf{v} \times \mathbf{B}). \tag{3}$$

and has to be computed at every instant for time-dependent flows. From equation (2), it follows that the strength of the Lorentz force for fixed fields is proportional to the electric conductivity $\sigma$ of the fluid. Because of a large range of possible values (molten metals, semiconductors: $\sigma \approx 10^6$ S/m; electrolytes, sea water: $\sigma \approx 10$ S/m) it is

clear that one has to distinguish between control strategies for highly conducting fluids and weakly conducting fluids.

## 2. Highly conducting fluids

For highly conducting fluids, e.g. molten metals, already the application of external magnetic fields can lead to considerable effects on the flow. Apart from a stabilizing influence of static fields that has been known for many years, recent research covers the more advanced combination of static and time-varying fields, which opens many new opportunities. Typical applications are in the field of metallurgy or crystal growth, where certain details of the flow (convection, thermal distribution, surface/interface shapes etc.) can be custom-designed by applying appropriate forces [1]. Apart from research that is close to industrial applications, there is still a need in basic research on the fundamental effects in magnetohydrodynamics (MHD). Many of the classical results were obtained decades ago but can be considerably refined today. Additional motivation comes from serious measurement technique problems that are existing in melt flows. Due to this, numerical simulations become even more attractive in this field.

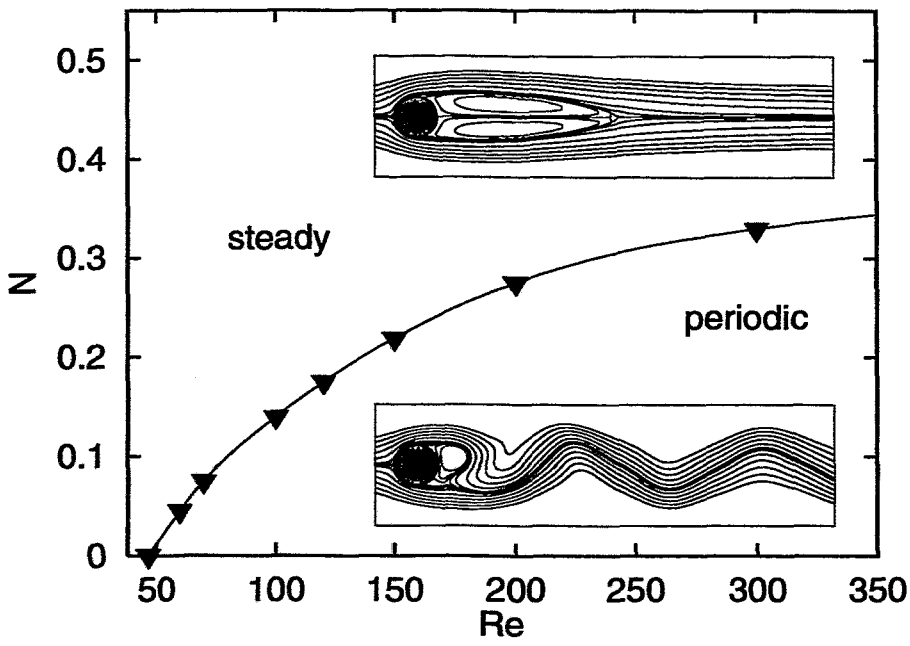


Fig. 1: Curve of neutral 2-D stability for the 2-D cylinder flow subjected to a constant aligned magnetic field. The inserts show isolines of the 2-D stream-function. Re=200, N=0.4 (top), and N=0.05 (bottom).

The research project described below is focused on the study of instabilities in the MHD flow around a circular cylinder as a canonical example for bluff body wakes. It was partly done in cooperation with Dr. V. Shatrov (ITAM, Novosibirsk) and Dr. A. Tomboulides (ETH, Zürich). A numerical code has been developed that incorporates the Lorentz body force including induced parts according to eq. (3) into the Navier-Stokes equation.

Firstly, the influence of steady magnetic fields on 2-D instabilities was investigated. The hydrodynamic cylinder flow is well known to become 2-D unstable at Re≈46, leading to the von Karman vortex street. By applying magnetic fields, depending on its direction, a damping of the 2-D instability can be achieved, and the 2-D flow remains steady until considerably larger values of the Reynolds number. Fig. 1 shows the curve of neutral stability for a magnetic field aligned with the freestream, obtained from a 2-D numerical simulation [2]. Here the interaction parameter $N \propto \sigma B^2/U$ characterizes the ratio between electromagnetic and inertial forces, and Re is the Reynolds number based on the cylinder diameter and the freestream velocity U. Above the stability curve the vortex street is suppressed, and the flow remains steady. For a magnetic field being transverse to both the freestream and the cylinder axis, the stabilizing influence is even stronger, and the recirculation of the steady flow can be suppressed as well. Further results of the 2-D flow can be found in [3].

The next step was, naturally, the investigation of 3-D instabilities in the flow. However, only recently the nature of the first 3-D instability towards a spanwise periodic flow at Re=188 for the hydrodynamic cylinder flow was understood [4]. Therefore, first it was investigated how a magnetic field influences such a 3-D instability at a Reynolds number of Re=200. A numerical 3-D linear stability analysis was performed, and the results were compared with and confirmed by a full 3-D numerical simulation. The results for all three directions of the magnetic field showed that there is mainly a damping influence of the magnetic field on the 3-D instabilities. However, for increasing aligned or transverse magnetic fields the underlying 2-D flow changes simultaneously, which leads to a nonmonotonic behaviour in the temporal growth rates of 3-D instabilities. In particular, for an aligned magnetic field the damping process with increasing magnetic field is relatively slow. In a certain range above the 2-D stability threshold 3-D instability still exists. Fig. 2 shows such a steady 3-D flow regime obtained by a full 3-D simulation.

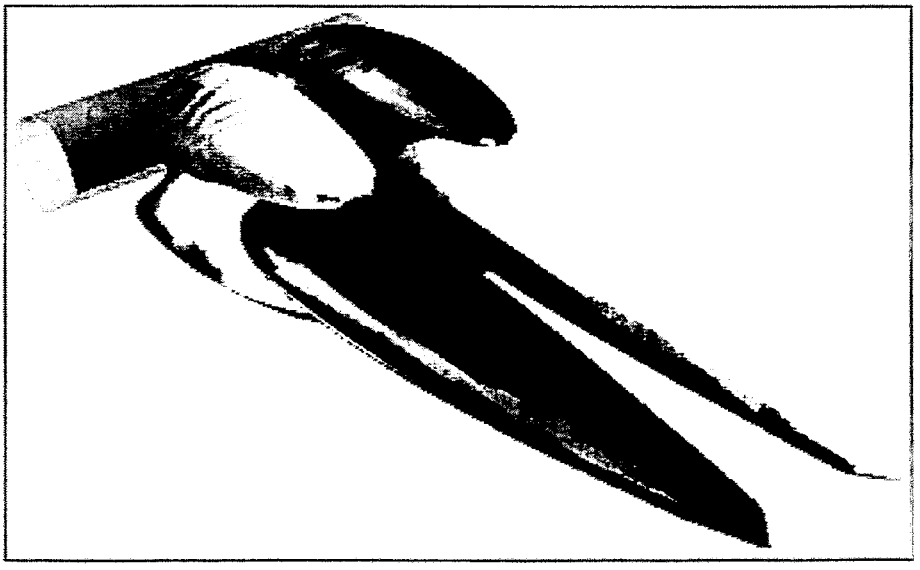

Fig. 2: Iso-surface of positive and negative spanwise velocity component of level 0.025 for the 3-D cylinder flow in an aligned magnetic field. Re=200, N=0.4.

This effect can lead to flow regimes where the order of instabilities is reversed, i.e. by increasing the Reynolds number for a fixed magnetic field strength, the flow first becomes 3-D unstable and only later-on 2-D unstable [5]. This result is qualitatively in line with the fact that the Squire theorem of local stability for parallel flows does not hold in the MHD case [6]. Furthermore, a broadening of the range of unstable wavenumbers due to the magnetic field action was detected in the numerical simulations which qualitatively confirms recent experimental results [7].

## 3. Weakly conducting fluids

For weakly conducting fluids like seawater ($\sigma \approx 4$ S/m) one can easily show that the electromagnetic forces due to induced currents have almost no influence on the flow. This is simply because the electrical conductivity is about six orders of magnitude smaller than for molten metals as discussed earlier. However, if an electric current is externally applied, considerable effect can be obtained. Because Joule dissipation takes place in all volume elements carrying currents, for a reasonable input amount of electric power it is desirable to keep the distance between the electrodes small. That means, large fluid volumes can hardly be controlled, but an influence on local flow properties, e.g. near a wall, is possible with reasonable energy expenditure. Specifically, any boundary layer phenomena like flow separation and transition might easily be influenced by placing electrodes and magnets on the surface of the body. Already in the sixties the flow over a flat plate equipped with suitable magnets and electrodes was investigated by applying laminar boundary layer theory [8]. It was shown, at least theoretically, that friction drag can be reduced by delaying transition of the boundary layer to turbulence. Only recently, even the control of turbulent boundary layers by electromagnetic forces became a topic of intensive research in the USA.

Experimental and numerical work of the group focuses on the control of bluff body wakes by means of electromagnetic forces localized in the boundary layer and directed parallel to the body surface.The experimental setup is described in detail in [9]. The following results were obtained for different configurations of steady forcing at a cylindrical body. Depending on the force direction relative to the mean flow it is possible to shift the separation points towards the front or the rear stagnation point. A wide range of flow regimes can be established, reaching from enhanced vortex shedding with separation near the front stagnation point to potential-flow-like regimes without vortex shedding to flows with a jet originating at the rear stagnation point.

The unforced flow around a circular cylinder at a Reynolds number of Re=760 is shown in Fig. 3. The boundary layer separates unsteadily, and the typical von Karman vortex street appears downstream of the cylinder. In general, boundary layer separation occurs when fluid decelerated by friction forces is exposed to a sufficiently strong adverse pressure gradient. Increasing the near-wall energy by accelerating the fluid using a wall-parallel Lorentz force, the wall layer retarded flow is able to withstand the up-hill pressure gradient and separation is therefore prevented. Fig. 4 shows such a flow regime at Re=760, N=2.5 (The definition of N is based on both applied fields: $N \propto jB/U^2$). The von Karman street is clearly suppressed. No recirculation is detectable, i.e. there is almost no form drag left. However, the boundary layer is laminar in the Reynolds number range considered here, and a body force with a maximum at the wall will lead to a steeper gradient of the wallparallel velocity

Fig. 3: Experimental visualization of the uncontrolled vortex street.

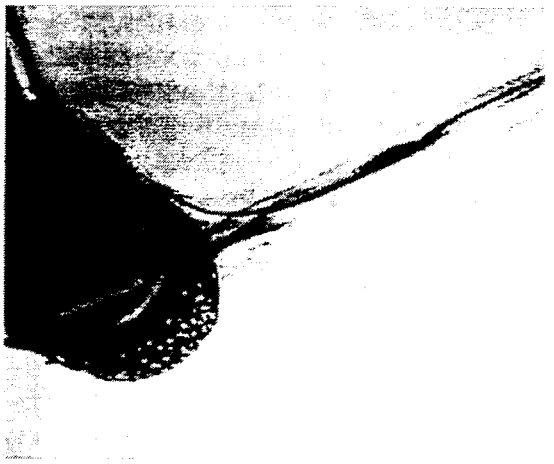

Fig 4: Experimental visualization of electromagnetic downstream forcing resulting in separation suppression.

and therefore to higher skin friction compared to the unforced case. Thus, with growing interaction parameter, although form drag is suppressed, skin friction drag increases. The sum of both kinds of drag has a minimum at a certain interac-tion parameter. Taking into account the momentum added by the Lorentz force, there is already a net thrust on the cylinder at small interaction parameters. So the total drag of the cylinder is negative for interaction parameters larger than a threshold value. A more detailed discussion is given in [10].

Apart from influencing the drag, the lift can also be controlled by applying a Lorentz force of fixed angular direction around the surface. Thus, a situation similar to the well known Magnus effect arises. The body experiences a lifting force resulting from the circulation produced by the Lorentz force.

Time-periodic boundary layer forcing opens a new rich variety of different flow regimes. Accordingly, opposite objectives like enhanced mixing and reduced drag can be achieved with properly chosen control parameters. Some of the preliminary results indicate that by using sufficiently large interaction parameters it is even possible to suppress the vortex street with forcing frequencies that are high compared to the Strouhal number. An obvious advantage of such control from the technical point of view is that alternating currents do not produce electrochemical bubbles at the electrodes and thereby corrosion is seriously reduced.

## 4. Summary

For highly conducting fluids control of bulk flows is possible and of immense technological importance in diversified fields such as metallurgy and crystal growth. Basic research on an MHD cylinder flow showed that 2-D and 3-D instabilites of the near wake can be controlled by applying external magnetic fields.
For weakly conducting fluids, such as saltwater, the possibility of electromagnetic flow control was demonstrated experimentally and theoretically for a cylindrical body. Further research will extend this investigation to larger values of the Reynolds num-

ber in properly designed configurations of electrodes and magnets. The ultimate aim is to achieve beneficial control with minimum energy expenditure. This research could lead to a variety of useful applications in sea vessels. A cooperation with German shipbuilders (Hamburgische Schiffbau-Versuchsanstalt HSVA, Howaldtswerke Deutsche Werft AG, Kiel) was initiated in order to identify possible fields of industrial applications. Further projects will cover first flat-plate experiments in a saltwater facility at HSVA and the design and construction of a saltwater tunnel in Rossendorf. In July 1997, an international workshop on „Electromagnetic Boundary Layer Control" will be hosted by the Rossendorf group.

**References**


[1] Innovationskolleg Magnetofluiddynamik elektrisch leitfähiger Flüssigkeiten Erstes Arbeitstreffen, TU Dresden, ILR, 24. Oktober 1996.

[2] G. Mutschke, G. Gerbeth, V. Shatrov,
"2-D and 3-D instabilities of the cylinder wake in external magnetic fields",
Lecture at: American Physical Society, 49th Annual Meeting of the Division of Fluid Dynamics, Syracuse, 25.11.96; Bulletin of the American Physical Society, Vol. 41, No. 9 (1996) p. 1715.

[3] V. Shatrov, G. Mutschke, G. Gerbeth,
"Numerical simulation of the two-dimensional MHD flow around a circular cylinder", Magnetohydrodynamics, vol. 33 no. 1 (1997) pp. 3–13.

[4] D. Barkley and R. Henderson,
"3-D Floquet Stability Analysis of the Wake of a Circular Cylinder",
J. Fluid Mech. vol. 322 (1996) pp. 215-236.

[5] G. Mutschke, G. Gerbeth, V. Shatrov and A. Tomboulides,
"2-D and 3-D Instabilites of the Cylinder Wake in an Aligned Magnetic Field",
to appear in Physics of Fluids, 1997.

[6] J.C.R. Hunt,
"On the stability of parallel flows with parallel magnetic fields",
Proc. Roy. Soc., Ser. A, vol. 293 (1966), p. 342.

[7] T. Weier, G.Gerbeth, G. Mutschke, A. Alemany, A. Pilaud,
"On the stability of the MHD flow around a cylinder in an aligned magnetic field", Magnetohydrodynamics, vol. 33 no. 1 (1997), pp. 14–22.

[8] A. Gailitis & O. Lielausis,
"On a Possibility to reduce the Hydrodynamical Resistance of a Plate in an Electrolyte", Applied Magnetohydrodynamics. Reports of the Physics Institute, Riga, vol. 12 (1961), pp. 143–146 (in Russian).

[9] T. Weier, G. Gerbeth, G. Mutschke, O. Lielausis, E. Platacis,
"Separation control of the cylinder wake using surface localized electromagnetic forces", Lecture at: American Physical Society, 49th Annual Meeting of

the Division of Fluid Dynamics, Syracuse, 25.11.96; Bulletin of the American Physical Society, vol. 41, no. 9 (1996), p. 1750.

[10] T. Weier, G. Gerbeth, G. Mutschke, O. Lielausis, E. Platacis, "Experiments on cylinder wake stabilization in an electrolyte solution by means of electromagnetic forces localized on the cylinder surface", to appear in Int. Journal of Experimental Heat Transfer, Thermodynamics and Fluid Mechanics, 1997.

*The projects summarized in this report are funded by Deutsche Forschungsgemeinschaft under grant No. Ge 682/3-4 and in frame of Innovationskolleg Magnetofluiddynamik. Further support from the European INTAS programme under grant No. 94-1504 is gratefully acknowledged.*

# WIND ENERGY POTENTIAL IN SAXONY

**W. Hirsch, U. Rindelhardt**

## 1. Introduction

Since 1990 investigations of the wind energy potential in Saxony have been performed [1]. They based on a special wind measuring programme running between 1992 and 1995. In the frame of this programme wind data sets (speed,direction, measuring height about 35 m) at 14 sites in Saxony were gained [2,3]. Similar data sets provided by the Deutsche Wetterdienst [4] for some other sites as well as for the geostrophic wind in Dresden-Wahnsdorf were also available.

The Danish Wind Atlas and Analysis Programme WASP [5] was used for the estimation of the Saxon wind energy potential. This code allows the extrapolation of the measured wind conditions from the measuring sites to their surroundings. Applying WASP the main task is the estimation of the area limits in which the extrapolation holds. WASP ressource calculations were performed over a great part of Saxony in a grid of 250 m to explore the natural potential of wind energy in Saxony. The WASP results were compared with results of mesoscale computer code simulationes, which were performed at the Universities of Karlsruhe and Oldenburg for some regions of Saxony [6,7].

The total technical wind energy potential was finally estimated on the basis of a reference wind energy converter (power 500 kW, 60 m hub height). The results were compared with yields of operating wind energy converters.

## 2. The application of WASP to interior regions

The WASP code was applied to calculate the wind atlas libraries of the measuring sites and to extrapolate the results to other sites. WASP was originally developed and verified mainly for coast and lowland regions, wich represents large areas of the same wind climate. Since many years the program has been applied with remarkable success for the evaluation of those sites. During the last years it has been used - frequently without sufficient verification - more and more also for interior areas.

WASP uses three simplified models to calculate the regional wind climate around the wind measuring station, which take into account the influences of obstacles, roughness, and orography upon the wind conditions. In case of low influence of the surrounding on the wind conditions (flatland with low roughness, few obstacles in the neighbourhood of the wind measuring station) the WASP atlas data set is compatible with the geostrophic wind. However, in Saxony the orographic conditions are rather complex, and therefore the WASP atlas data set represents only the regional wind climate in a limited region around the wind measuring station (representance area). The application of WASP to complex terrain therefore always requires investigations about the representance areas of the available wind data sets.

This verification was done by comparison of measured and calculated wind conditions

at different wind measuring stations in Saxony. Only in case of neglecting small differences between measured and (with data from an other measuring station) calculated wind conditions the considered wind measuring stations belong to the same wind climate. The investigations of the representativeness of 22 available data sets (8 from Deutscher Wetterdienst) are described in [8] in detail. It could be shown that the wind conditions in large regions of Saxony can be described by only 8 data sets. Fig. 1 shows the representance regions belonging to the different data sets. In some areas no useable data sets are available at present. The sites of redundant data sets are marked by empty symbols (circle: Deutscher Wetterdienst, triangle: site of wind measuring programme). In the upper regions of Erzgebirge (complex terrain) the application of WASP in the most cases is impossible.

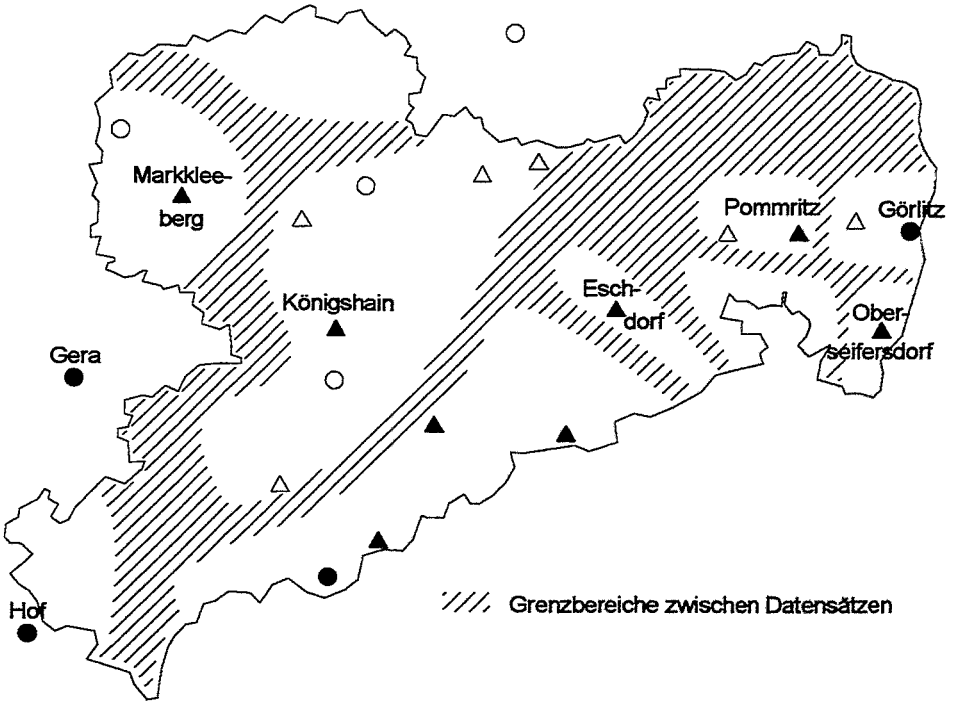


Fig. 1: Representance of WASP data sets in Saxony

### 3. The estimation of the wind energy potential by mesoscale models

Mesoscale computer simulation models were originally developed especially for weather forecasts in mesoscale regions (in contrast to european region for example) and for simulation of atmospheric transport of pollutants [9]. They can also be used for the estimation of the wind energy potential, but in this case many simulation runs are necessary to obtain an acceptable statistics for the mean annual wind energy.

Mesoscale models describe the atmospheric processes based on the fundamental physical equations with the geostrophic wind as driving force. Another advantage of applying these models is the possibility to calculate much greater regions then the WASP code. The disadvantages of complex mesoscale models are mainly the weak resolution (limit for grid distances approximately 2 - 5 km) caused by the applied

numerical approximations and also the need of large computer capacity. The wind prediction for single wind energy converter sites is therefore impossible. The result of a mesoscale calculation is the mean wind climate over a grid element.

The wind conditions in a large region of Saxony (Zentralsachsen) were calculated by Adrian [6] with the mesoscale code KAMM. The comparison of KAMM results with WASP estimations of wind conditions showed considerable differences [10]. The mean wind speed at 40 m height above ground level was generally overestimated by KAMM (about 0.6 m/s to 1.5 m/s). Obvious there are some fundamental problems (probably the transformation of the wind statistics of geostrophic wind into such for the wind over the ground) in applying the mesoscale models for wind energy prognoses.

Nevertheless,a better agreement between the calculated and measured and WASP estimated wind conditions in the same region could be obtained with the reduced mesoscale models AIOLOS [7]. Because of the drastically reduced computing time it is possible to make computations for all conditions of the geostrophic wind. Therefore, at least a realistic estimation of the wind statistics over the ground is possible. Furthermore, this code allows the computation with smaller grid distances than complex mesoscale models. Therefore the orography can be taken into account in more detail.

The differences of wind speed between AIOLOS results and the measured values in Zentralsachsen are significantly lower (in large regions better than ± 0.5 m/s) compared with results of complex mesoscale models. However, for the purposes of wind energy estimation the differences are still inacceptable.

**4. The estimation of the wind energy potential in Saxony**

The mean wind speed in a fixed height above ground level is frequently used to characterize the wind energy potential of a site or an area. But this holds only under the presumption of identical wind speed distributions at different sites. Practically the wind speed distribution differs remarkably, which results in different mean wind power densities. Therefore the mean wind speed is not suitable to characterize the wind energy potential. Note that the distribution is also dependent from the height.

To define the natural wind energy potential the mean power density in the hub height of a modern wind energy converter (today about 60 m) is the characteristic value. The technical potential of wind energy is much lower, because real wind energy converters cannot exploit the whole wind energy offered over an area. To calculate the technical wind energy potential the natural wind energy potential has to be weighted by the power curve of the wind energy converter and with the number of possible converters. Practically the yield of a modern reference wind energy converter is used.

Fig. 2 shows the regions with good wind conditions in Saxony, which were evaluated based on WASP calculations over 2/3 of the Saxon territory and additional evaluations based on the yields of operating wind energy converters. In the marked regions a yield of more than 1500 full-load hours can be expected for modern wind energy converters at open sites. However, even outside of the marked areas a large number of single sites exist.

By the WASP calculations useable wind conditions were identified in an area of 976 km² (about 5 % of Saxonys total area). Assuming a total use of this area (that means installation of wind energy converters with the highest possible density) and taking into account the ressources of the (not calculated) smaller areas in Saxony like Erzgebirge a total technical wind energy potential of almost 20000 GWh/a was estima-

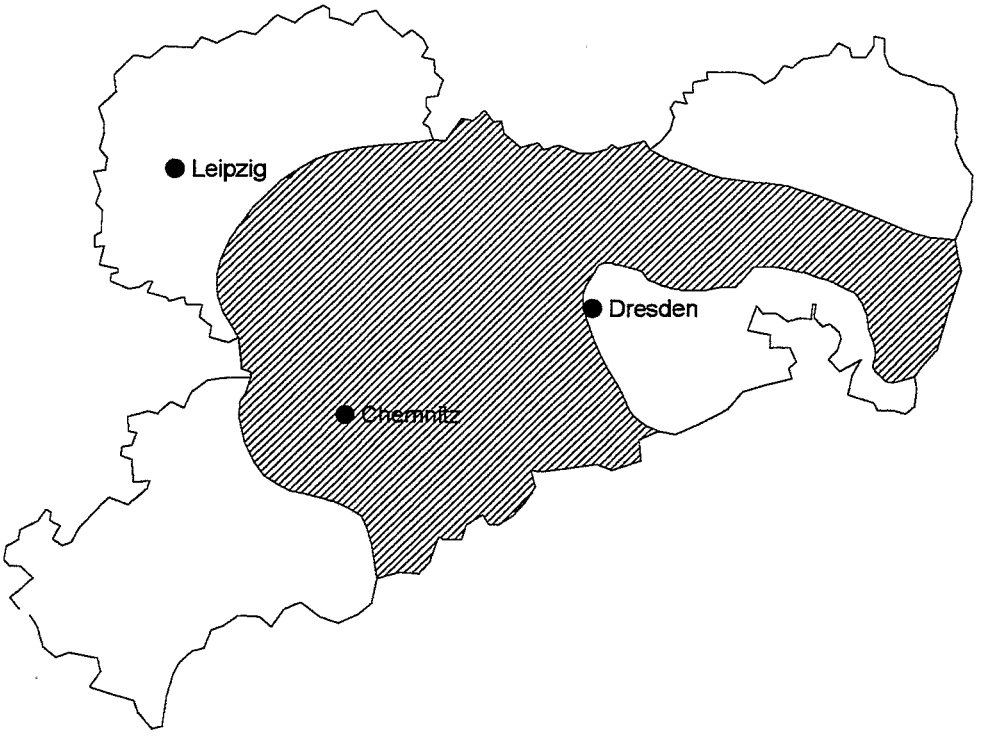


Fig. 2: Regions with useful wind potential in Saxony

ted. In a more realistic approach with consideration of 50 % reduction caused by other use of the identified areas and further 50 % reduction caused by a lower converter density the realistic technical potential was estimated to be 5000 GWh/a. This value corresponds to 25 to 30 % of the actual electricity consumption in Saxony.

## 5. Exploitation of the wind energy potential

The use of wind energy in Saxony started in 1991 with the grid connection of the first wind park in Satzung (Ergebirge). Since 1992 in Saxony the wind energy use has been dynamically developed. It based mainly on the technical progress made in the converter technology, which led to a continuous decrease of the costs. The development was stimulated by supporting programmes of the Federal Government (electricity feed law, 250-MW-Programme) and also of the Freistaat of Saxony. At the end of 1996 159 wind energy converters with a total power of 70 MW were installed and in operation. They produced an energy of about 65 GWh in 1996.

The yield of each converter reflects the wind conditions at the site. Therefore it can be used for the direct verification of WASP results ( if no technical problems at the con-

verter occured). A yield of about 2000 full-load hours was reached in 1996 at the best Saxon sites (located in the Sayda region in the Erzgebirge, also Laucha in the Oberlausitz). This is particulary remarkable, because the year 1996 was an untypically weak wind year. A yield of about 1650 full-load hours can be expected as mean value (in normal wind years) for the converters operated in 1996. At the other hand the results from 1996 proof that some converters were installed and operated at sites not suitable for wind use (yield less than 1000 full-load hours). In such cases a profitable operation is impossible.

These results demonstrate the need for further progress in the 3D wind field calculation in orographic complex regions. Considering the above mentioned methodical difficulties with the codes used so far systematic further investigations would be useful.

**References**


[1] U. Rindelhardt, H. Müller: Wind- und Kleinwasserkraft in Sachsen
Neue Energie 1 (1991) 136

[2] "Windenergienutzung im Freistaat Sachsen, Windmeßprogramm"
Staatsministerium für Umwelt und Landesentwicklung, Dresden 1994

[3] "Windenergienutzung im Freistaat Sachsen,
Windmeßprogramm Sachsen, Teil II (Abschlußbericht)"
Staatsministerium für Umwelt und Landesentwicklung, Dresden 1996

[4] Deutscher Wetterdienst: Winddaten für Windenergienutzer
Offenbach 1996

[5] N. G. Mortensen, et al.
"Wind Atlas Analysis and Application Program (WASP)"
Risø National Laboratory, Roskilde, Denmark, Jan.1993

[6] G. Adrian,N. Dotzek, F. Fiedler: Bestimmung geeigneter Standorte für die Windenergienutzung in topografisch gegliedertem Gelände mit mesoskaligen Strömungsmodellen
Karlsruhe, August 1995

[7] R. Müller: Untersuchungen zur Windpotentialbestimmung im gegliederten Geländemit Hilfe eines massenkonsistenten strömungsmechanischen Modells"
Diplomarbeit Universität Oldenburg, Fachbereich Physik, 1996

[8] W. Hirsch, U. Rindelhardt and D. Brünig: Windpotentiale in Sachsen
Abschlußbericht Forschungszentrum Rossendorf, März 1997

[9] H. Schlünzen, M. Schatzmann: Atmosphärische Mesoscale Modelle - Ein Überblick
G.M.L. Wittenborn Söhne, Hamburg 1984

[10] W. Hirsch, U. Rindelhardt, G. Tetzlaff:The Saxon Wind Energy Resources: Comparison of WASP and KAMM Results
Proc. of the 1996 EU Wind Energy Conference and Exhibition
20-24 May 1996, Göteborg, Sweden, p. 604



*The project this report is based on was funded by the Saxon State Ministry of Environment.*

# THE APPLICATION OF DECISION ANALYSIS TO THE REMEDIATION DECISION - METHODOLOGICAL DEVELOPMENTS

**S. Kruber**

## 1. Introduction

Decisions in the public sector (e.g. waste disposal problems, sustainable city development, siting of hazardous industrial facilities or remediation of contaminated sites) are very complex and conflict-ridden, but the stakes involved in these decisions are high and the consequences can be tremendous. Therefore it seems very profitable and scientifically challenging to support this kind of decision and to make it transparent.

From a methodological point of view, decision-analysis is well adapted to these decisions and to overcome some inherent problems (uncertainty, multiple objectives, several agents with diverging interests). Unfortunately, it is quite difficult to introduce such an abstract and mathematical approach to decision-making as the standard procedure for public decisions.

The workgroup 'Applied Decision Analysis and Risk Assessment' investigates the applicability of decision-analysis in this context. During the last years its work focused primarily on remediation decisions, which are prototypical for the public. For this purpose, as a demonstration object, a municipal waste disposal site ('Bergen') which threatens the groundwater was chosen in 1994. Together with the responsible state and local authorities (decision-makers) a set of criteria to assess possible remediation concepts was established. In co-operation with remediation companies some plausible concepts were projected and evaluated with respect to the criteria. The results were presented to the decision-makers to finally reach a conclusion about the preferred concept. A detailed description of this work can be found in [1], [2] and [3].

This document reports selected methodological deficits of the standard procedure of decision analysis [4] which were identified during the application at 'Bergen'. Approaches to overcome these problems will be presented.

## 2. Elicitation Procedure for the Total Utility Function

Eliciting total utility functions from decision-makers in public decisions can be characterised by three problems:

- The persons involved in the decision have little knowledge about the methodological aspects of decision analysis. Therefore it is necessary to impart fundamental knowledge about decision analytic techniques during elicitation.
- It is a misconception to assume, that the decision-makers accept to weigh up the criteria. They rather try to avoid explicit statements necessary for this procedure as far as possible. One reason for this reluctance is the fear of the persons, that their statements will be misused and may raise unexpected legal problems.
- Quite often the persons do not have an *a-priori* preference structure about possible results.

These problems contradict the opinion, that the only task for elicitation is to represent the internal preference structure as a mathematical model. Therefore the methods developed previously (cf. [5] for a detailed description) turn out to be insufficient for public decisions. As a result of the items above, four goals have to be pursued within the elicitation of total utility functions:

1. Development of preference structures
2. Dissemination of decision analytic techniques
3. Gain acceptance for the decision analytic approach
4. Determination of the total utility function

To overcome the problems of conventional approaches and to cope with the requirements defined above, an indirect approach for the elicitation of total utility functions has been developed and tested. The primary intention of this approach is to demonstrate to the decision-maker, that the formal decision system defined by the total utility function, is based on his statements and represents properly his decisions in simple situations. The approach lays the foundations for the finer adjustment of the total utility components (e.g. utility functions and trade-off-rates). Thus this approach does not replace the conventional methodology, it just complements it.

The approach consists of the following steps:

1. Selection of two criteria relevant for the decision maker

   In the following example the cost of the remediation action $x$ and the final concentration $y$ for the most relevant contaminant were chosen. The utility function $u(x,y)$ used in the following represents a generic part of the total utility function.

2. Presentation of several simple decision problems (cf. Table 1) and determination of qualitative properties of the total utility function

   The intention of this first step is to assist the decision-maker in the development of an internal preference structure for results. Additionally qualitative properties of this structure (e.g. boundaries for acceptable results, non-linear preferences) have to be determined and the decision maker must be led to a balancing of results for decision-making.

| Concept | Cost | Final Contaminant Concentration[1] | Decision |
|---|---|---|---|
| 1A | 10 MDM | 130 % | not feasible due to contaminant concentration |
| 1B | 13 MDM | 90 % | to be preferred |
| 1C | 45 MDM | 50 % | feasible but not preferred |
| 1D | 50 MDM | 0 % | not feasible due to cost |

[1] The contaminant concentration is measured in percentage of the legal threshold value.

Table 1: Selected Decision Problem for the Elicitation of Qualitative Structures of the Total Utility Function

3. Presentation of refined decision problems and adjustment of a mathematical formula

Based on the information from step 2 a mathematical formula for the total utility function has to be selected. In the test case the following formula was assumed:

$$u = -\frac{e^{\alpha x}-1}{\alpha} - k_y \cdot \frac{e^{\beta y}-1}{\beta} \; ; \; \alpha,\beta,k_y > 0$$

Then refined decision problems must be designed, which will give a maximum of information for the determination of the free parameters in the formula. The decision problems presented for the test case are sketched in Fig. 1.

The decisions of these problems can be used to determine approximately the local trade-off-rates of the total utility function at different co-ordinates. With the total utility function $u(x,y)$ the trade-off-rate $t$ is defined as: $t(x,y) = \partial x / \partial y|_{u=\text{const}}$. If the decision problems are constructed like in Fig. 1, a linear function $c=a \cdot K+b$ through the point of the preferred concept must be constructed, which does not cut the straight lines connecting the concepts. The gradient $a$ of this function is equal to the trade-off-rate $t$ at this point. With this information it is possible to fit the parameters $\alpha$, $\beta$ and $k_y$. In the test case a Levenberg-Marquardt-method [6] for non-linear parameter fitting was used.

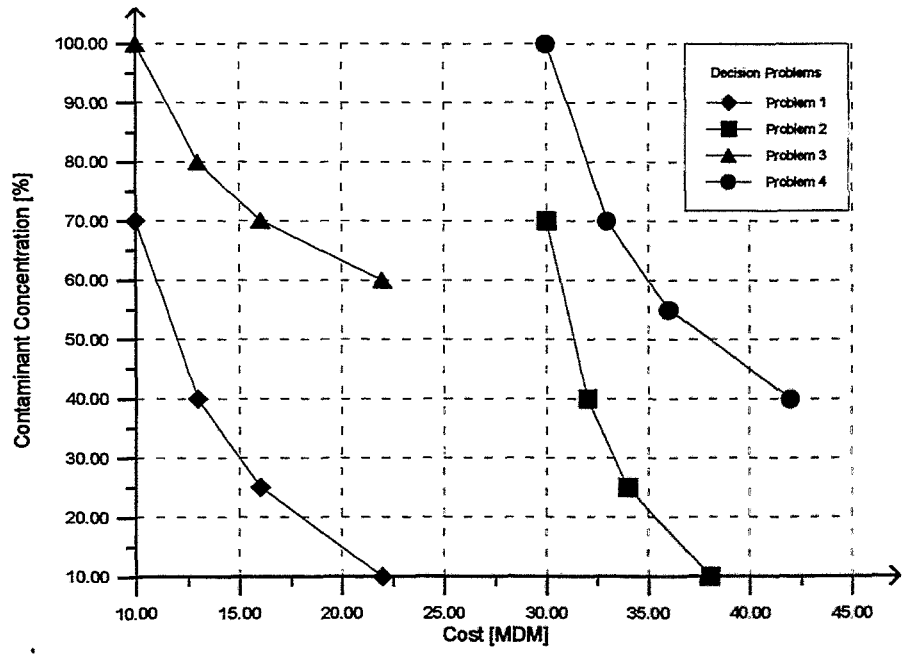


Fig. 1: Refined Decision Problems for the Adjustment of the Total Utility Function

4. Validation of the adjusted formula

To validate the appropriateness of the parameters determined in the last step, several control decision problems should be constructed. They have the same form as those presented above; the procedure for parameter fitting also remains the same. The process of validation and adjustment has to be iterated, until the parameters have converged and the total utility function represents the decisions accurately.

5. Presentation of the results to the decision-maker

   The fitted total utility function and the way it represents the decisions made have to be demonstrated to the decision-maker within this step. Additionally the necessity of formal models (like the total utility function) should be explained now. In the test case it was observed, that this procedure finally yielded acceptance for the total utility function in contrast to a previous reluctance.

6. Iterative Determination of the Total Utility Function for the Other Criteria

   The procedure defined above (step 1-5) has be executed for all other criteria in order to get a complete total utility function for all criteria. The results can be used as a starting point for conventional elicitation procedures for utility functions.

In summary it can be said, that the elicitation of total utility functions only with conventional methods will fail for public decisions. The approach described above circumvents the problems of those methods and has shown to be applicable and well-accepted by decision-makers.

## 3. Action Networks

The experiences made through the application of decision analysis support the following hypothesis: The representation of remediation alternatives with conventional techniques of decision analysis (e.g. decision trees [7] or influence diagrams [8]) turns out to be insufficient. Reasons are as follows:

1. The pilot tests and field experiments possibly executed before remediation provide very complex information (e.g. about the feasibility of technologies, simultaneous reduction of multiple uncertainties). The value of such investigations cannot be estimated within the framework of value-of-information calculations [9].
2. The decision-makers exhibit the tendency to split the decision into smaller subdecisions and the alternatives into activities. This approach requires the representation of sequential decisions and the structuring of alternatives.
3. For many remediation technologies it is not possible to estimate in advance whether they are feasible under the site-specific circumstances. This is especially true for modern technologies (e.g. biological and *in-situ* techniques). In some cases, pilot tests will help to determine the applicability; in other cases even pilot tests will not yield absolute certainty of success. The late refusal or withdrawal of permission can be another reason for the failure of remediation concepts.
   If the selected remediation concept fails, the decision-maker will be confronted with the starting decision problem again (only approximately because time and money will have been lost). This problem cannot be represented by criteria because the potential disadvantages depend heavily on the alternatives. Instead, it must be handled within the action structure by the new concept of 'recursive decision problems'.

None of the methods available for decision analysis nowadays is capable to represent decision problems caused by these three problems. Based on an example, the use of 'action networks' for such decision problems will be sketched. Action net-

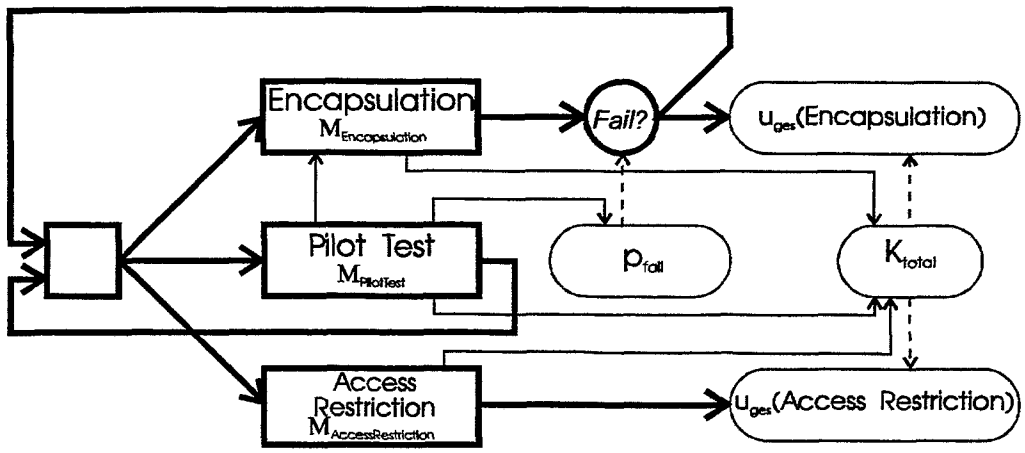


Fig. 2: Action Network for a Complex Decision Problem

works[1] are based primarily on decision trees. They add some new components and features to them.

As working example the following situation will be regarded which occurred similarly at the test site "Bergen":

> For remediation the concepts 'encapsulation' *E* and 'access restriction' *A* are considered. *E* has the disadvantage, that it may prove to be leaking with a probability $p_{fail}$. In this case, *A* has to be carried out in addition. The total cost $K_{total}$ will be in this case: $K_{total}=K_E+K_A$. $K_E$ can only be predicted approximately. To determine $K_E$ exactly, a pilot test can be made. This test also gives the information whether *E* will fail or not, but it will increase the total cost.

An action network to represent this decision problem is presented in Fig. 2. Its components and features will be described now:

- The action network contains some standard elements of decision trees: decision nodes (squares) and chance nodes (circles).
- As a new component of action networks 'information nodes' (rounded rectangles) have been introduced. These information nodes contain probabilistic data e.g. simple probability density functions up to Markov-nets. Those information nodes which are connected to the flow of action (thick lines), have to provide a method for calculating the resulting total utility $u_{ges}$.
- Another new component are 'action nodes' (rectangles). These nodes can modify (thin lines) information nodes (e.g. the probability distributions stored within them) and other action elements. All action nodes contain a feasibility flag (M) to prevent endless recursion and to mark processed paths.
- The data dependencies of all nodes are indicated by thin dashed lines.
- A characteristic of action networks is the circular flow of action (e.g. from the chance node $p_{fail}$ and the action node pilot test back to the root decision node). With this tool, recursive decision problems can be displayed.

[1] The expression 'action networks' has already been introduced in literature for an extension to influence diagrams [10]. The model structure presented here has very little in common with that described in [10] and was developed independently.

## 6. Further Developments

The action networks described above are a graphical representation of complex decision problems and data dependencies. Currently investigations which aim at the definition and implementation of an evaluation algorithm for action networks are under way [3]. Thus action networks will become a valuable computational aid for complex decision problems.

The methodological developments presented in this report will be put into practice within the framework of envisaged decision problems in the public sector. Special emphasis will be given to the implementation of supporting tools for the methods described above. The workgroup 'Applied Decision Analysis and Risk Assessment' especially concentrates on the application of decision aiding techniques. Many fundamental problems for decision analysis can be identified in the public sector. Consequently the refinement of methods which are directly applicable for the end-user will be a basic task for the future.

## References


[1] Ferse, W. and Kruber, S. (1994): Applied Decision Analysis and Risk Evaluation, Report, Institute for Safety Research, Research Centre Rossendorf, pp. 62-67

[2] Kruber, S. and Ferse, W. (1995): Applied Decision Analysis for Remedial Decisions at Contaminated Sites, Report, Institute for Safety Research, Research Centre Rossendorf, p. 122

[3] Kruber, S. (1997): Anwendung der Entscheidungsanalyse bei der Sanierung von Altlasten, Ph.D. diss., Institute for Safety Research, Research Centre Rossendorf, in german, to appear

[4] Keeney, R. L. and Raiffa, H. (1993): Decisions with multiple objectives, Cambridge University Press, Cambridge

[5] Keeney, R. L. (1975): Energy Policy and Value Trade-offs, Research memorandum, IIASA, RM-75-76, Laxenburg

[6] Press, W. H., Teukolsky, S. A., Vetterling, W. T. and Flannery, B. P. (1992): Numerical Recipes in C, 2nd ed., Cambridge University Press, Cambridge

[7] Raiffa, H. (1968): Decision Analysis, Reading, Addison-Wesley

[8] Shachter, R. D. (1986): Evaluating Influence Diagrams, Op. Res., **34**, p. 871-882

[9] Howard, R. A. and Matheson, J. E. (1989): Readings on the principles and applications of decision analysis, Strategic Decisions Group, Menlo Park, Calif.

[10] Darwiche, A. and Goldszmidt, M. (1996): Action Networks: A Framework for Reasoning about Actions and Change under Uncertainty, in Uncertainty in Artificial Intelligence, Proc. 10th Conf., ed. de Mantaras, R. L. and Poole, D., Morgan Kaufmann Publishers, San Francisco, Calif.

# Short Contributions

## Thermal hydraulic and neutron-kinetic computer codes for accident analyses

*D. Lucas*
*H.-M. Prasser*

### Theory of depressurisation of chemical reactors

The VW foundation supports the development of a computer model describing the complex depressurisation system of a chemical reactor, which includes the reactor itself, the safety valve, vent lines, a separator, and a catch tank. This is a joint research project of FZR together with the University of Hannover. FZR is responsible for the modelling of reactor, vent line and safety valve.

In the present stage, the mixture level model for the reactor was coupled with a model of the vent line. A linear stability analysis predicted the existence of strong mass flow oscillations in the vent line, appearing under unfortunate conditions. This theoretical prediction was experimentally confirmed at the pressure vessel test facility of the Hochschule für Technik, Wirtschaft und Sozialwesen Zittau/Görlitz (FH). The oscillations were characterised by needle probes (void fraction) inside the vent line and the pressure drop over the vent line.

*A. Aszodi*
*E. Krepper*
*U. Rohde*

### Multidimensional fluid dynamic simulations

The convective motion inside a storage tank during an external heating in case of fire was modelled with CFX-4 (FLOW3D) and an own 2D-computer code. The result of the calculations was in good agreement with measuring data from experiments in three different scales (experiments of VKTA). In case of heating the side wall of the cylindrical vessel, a temperature stratification occurs, which causes an early start of the evaporation of the liquid inventory, long before the average temperature reaches saturation. The calculations with CFX-4 aimed at the optimisation of baffle plates for the intensification of mixing. The baffle plates improve mixing by breaking the boundary layer. The time before evaporation can be increased by approximately 20%.

The models were extended to consider gravel as an additional component. The presence of gravel origins from the assumption that building rubble falls into the tank during the accident.

Another 3D analysis was related to the secondary side of the emergency condenser of boiling water reactors. The calculations were performed for the NOKO test facility representing the emergency condenser of the SWR1000 developed by Siemens. During the single-phase heat-up period, a significant stratification with a dead water region at the bottom of NOKO was found. The results are in good agreement with NOKO data.

*U. Grundmann*
*S. Kliem*
*U. Rohde*
*A. Seidel*
*T. Schulz*

**Coupled code DYN3D-ATHLET**

An up-dated version of the neutron-kinetics code DYN3D was released. It joints the last program developments, which are: coupling interface, stand-alone mode, burn-up module, coolant mixing module for partial loop operation, decay heat release. The KASSETTA library of macroscopic cross-sections was linked to extend the neutron physical data basis.
The analysis of an assumed steam line break accident at a WWER-440 plant was completed. It was shown that, due to the coolant temperature decrease, a re-criticality of the shut-down reactor is possible, when the coolant mixing in the lower plenum is incomplete. Nevertheless, the re-criticality does not lead to a significant energy release.

*E. Krepper*
*F. Schäfer*

**Verification of the thermohydraulic system code ATHLET**

FZR takes part in the verification of ATHLET applied to Russian type reactors. The activities also comprised the calculation of a 1% break experiment conducted at the test facility PMK-2 in Budapest. The test included a primary bleed as accident management procedure. The calculation has confirmed the experimental findings, that the primary bleed procedure avoids core uncovery.
The post-test calculations of two natural circulation tests at the ISB-WWER facility in Electrogorsk were finished. During the experiments, different types of fluid dynamic instability were observed, which could be interpreted theoretically. These phenomena were adequately modelled by ATHLET.
In the frame of the external ATHLET verification cluster initiated by BMBF, FZR has started post-test calculations of two BETHSY tests.

## Experimental investigation of safety relevant thermal fluid dynamic effects in two-phase flows

*T. Kern*
*D. Lucas*
*H.-M. Prasser*
*H. Steinkamp*

**Depressurisation of chemical reactors**

Depressurisation experiments were conducted in a 3 l batch reactor model by carbon dioxide production during the decomposition of a carbonate solution with sulfuric acid. The influence of surfacting additives (alcohols of low molecular weight, tensides) on the process was studied. The additives lead to an intensive foam production that causes a significant increase of the fluid flow discharged from the reactor. One percent of alcohol (e.g. isopropanol) increases the quantity of liquid ejected from the reactor by a factor three.
During the depressurisation of pure Ethanol at a lab reactor of Hoechst AG (scale 100 l, 1 MPa), axial void fraction distributions were measured with needle probes. The results were

successfully reproduced in calculations with the code BLDN developed in Rossendorf.

*A. Böttger*
*H.-M. Prasser*
*P. Schütz*
*J. Zschau*

**Development and calibration of two-phase flow measurement techniques**

A mesh-sensor for the visualisation of the two-phase flow in pipelines was developed. The resolution is 1024 frames per second at 16 x 16 measuring points distributed over the cross section. The achieved time resolution surpasses the devices known from literature almost by a factor 10. The new method does not require tomographic image reconstruction, which is a great advantage in comparison to other methods. The sensor is being applied to transient two-phase flows. Experiments at a test facility of UMSICHT Oberhausen aim at the visualisation of cavitation behind a fast acting valve in a pipeline. Beside the mesh-sensor, needle probes and ultrasonic sensors are used in Oberhausen.

*A. Böttger*
*H.-M. Prasser*
*J. Zschau*

**Participation in thermal hydraulic experiments**

The flow pattern inside a heat exchanger tube of the NOKO emergency condenser test facility in Jülich was visualised for the first time. This was achieved by arrays of needle probes. NOKO is a model of the emergency condenser of the SWR-1000 being under development at Siemens KWU. Needle probes were also applied to a small break LOCA experiment at the PMK-2 (VVER-440/213) test facility in Budapest. The experiment, an inadvertent opening of the pressurizer safety valve, was part of a project of the EU PHARE programme.

*A. Grahn*

**Thermoconvection and instabilities at the boundary layer of two non-miscible liquid reacting components**

Different kinds of thermoconvection at the boundary layer between two non-miscible liquids were visualised in a capillary gap. The convection was driven by thermal and density effects. Several exothermic reactions and, as a reference case, the non-reactive mass transfer of a diluted component were investigated. By using either cyclohexane or brome-cyclohexane as organic solvent in contact with water, the stratification was inverted without changing the chemical reaction. The water is the heavy phase in the first case, the light phase in the second. Different kinds of self-organising structures were visualised and explained qualitatively.

*F. Hensel*

**Application of radiotracers**

The planned experiments concerning the turbulent mixing of a liquid tracer in a bubbly flow were carried out and evaluated. A tracer solution containing F-18 was injected into a bubbly flow, and the mixing was recorded by an array of PET detectors. The flow was either created by air injection into water or by hydrogen peroxide decomposition at a platinum surface. The better spatial resolution of the PET method in comparison to previous work allowed to eliminate errors caused by the convective motion of the liquid. In the result, the obtained more realistic values of the turbulent dispersion coefficient are smaller, than the data from the literature. Further, a simplified detector assembly was constructed that facilitates the practical application of positrones to the density measurement of low density materials.

*A. Böttger*
*H.-M. Prasser*
*J. Zschau*

**Improvement of needle shaped conductivity probes**

Special probes for a diversified level indication in boiling water reactors were developed. Prototypes are being tested under long term conditions in a test facility of the NPP Gundremmingen.

## Materials safety

*H.-W. Viehrig,*
*W.-D.*
*Leonhardt*

**Commissioning of a radioisotope laboratory for mechanical testing**

The commissioning of a radioisotope laboratory for mechanical testing was widely finished. The laboratory disposes of a hot double box with a specimen storage. The containment shields a servohydraulic testing machine and an instrumented pendulum impact tester. With the shielding containment a new way regarding the mechanical testing in hot laboratories has been gone. Whereas usually the complete testing machine is placed within the hot cell, in the new design only the testing machines are inside the containment. The engine unit, the control system etc. remain outside. Thus, they are not contaminated and are easily accessible for maintenance and exchange.

*H.-W. Viehrig,*
*J. Böhmert*

**Specimen Reconstitution Technique for Charpy Size Specimens**

Specimen reconstitution is a technique that incorporates a small piece from a previously tested specimen into a new compound specimen. It allows to multiply the number of tests. Reconstituted Charpy size specimens are produced by cutting off insert pieces from broken halves of Charpy V-notch specimens, by welding end blocks to the insert pieces and by machining the slug to a reconstituted Charpy specimen. In spite of the welding heat applied to the specimen the mechanical properties of the

reconstituted specimen must be identical with these of the original one. For Charpy impact tests the comparison of dynamic strength and toughness parameters does not reveal differences beyond the typical scattering. Fracture toughness and crack initiation toughness which have been determined by means of the partial unloading compliance technique with reconstituted side grooved and precracked Charpy size specimens, however, show small deviations. This proves that the compliance of the specimen depends on the response of the whole compound specimen. Thus, for the determination of fracture mechanics parameters the reconstitution technique needs the application the same material for end blocks and insert and does not tolerate welding failures.

*supported by BMBF*

*M. Grosse, J. Böhmert*

**Irradiation effects in reactor pressure vessel steels**

Small angle scattering techniques were applied to reveal the influence of the irradiation temperature on the microstructural changes. Two heats of the American A533-B-1 reactor pressure vessel steel differing in their Cu content (0.07 and 0.14 wt.-%) were irradiated to a fluence of $1 \times 10^{18}$ n/cm$^2$ at temperatures of 60, 121, and 288°C, respectively. Independent from the Cu content only for the irradiation at the lowest temperature irradiation effects could be proven by small angle neutron and X-ray scattering measurements. Surprisingly, the irradiation-caused change of the scattering intensity appears at low scattering vectors Q. Thus, the irradiation defects are relatively large (R = 10 nm). The measured A-ratio (ratio between nuclear and total scattering length density) is approximately 1.4 for higher Q-values. The energy dependence of the small angle X-ray scattering is identical for the matrix and the precipitates. This stimulates the assumption that the scattering defects are inhomogenities with a number density like voids or dislocation loops.

*supported by BMBF*

*M. Grosse, J. Böhmert*

**Local effects ahead of a crack tip detected by scanning micro-beam small angle X-ray scattering**

Scanning micro-beam small angle X-ray scattering (SM-SAXS) is a new technique which allows to identify positional and/or compositional deviations from the normal matrix structure at nanometer scale with a high lateral resolution. The micro-structure ahead of a crack tip of a bended specimen from pure and alloyed Al was investigated by this technique at the MICRO-FOCUS beam line of the ESRF Grenoble. Intensive and partly very anisotropic scattering intensities could be observed. The scattering intensity inside the plastic zone follows a power law. Both the exponent of the power law and the integral scattering intensity decrease with increasing distance of the crack tip and shape a pattern corresponding to the plastic zone.

*supported by DFG*

The scattering effects can be explained by scattering due to dislocation. A proof for the existence of microvoids near the crack tip could not be found.

*U. Bergmann, F. Bergner, J. Böhmert*

**Measurement of crack initiation and growth by ultrasonic (US) methods**

An ultrasonic time-of-flight diffraction method has been developed in order to monitor the in situ crack growth in small 3-point bending specimens. The method uses a transversal wave that is diffracted at the crack tip. To improve the evaluation of the measured signals a new evaluation technique was developed. This technique presents the sequence of the measured US signals in a displacement-US time-of-flight diagram by transforming the US wave amplitudes into different grey levels. This presentation enables to recognize the process of crack blunting and crack initiation. Additionally, crack growth can even be measured if the measuring signal is superimposed by other echos. In this way, the application of the US method is even possible for materials with a heterogeneous microstructure. The methods was tested with different Fe alloys. In all cases the crack length which was measured with the US method was in correspondence to the optically measured crack length within a scattering band of 15% as required by the standards.

## Simulation of particle and radiation transport

*H.-U. Barz, B. Boehmer, J. Konheiser, I. Stephan*

**Neutron dosimetry of reactor pressure vessels**

In the framework of a research project funded by the BMBF neutron dosimetry calculations were performed for the Russian Rowno-3 VVER-1000 reactor. Using the 3-dimensional Rossendorf Monte Carlo Code TRAMO and modern ENDF/B-6 neutron data fluence integrals and fluence spectra were calculated at positions near to the outer surface of the pressure vessel. Variance reducing techniques were extensively applied. The fission sources considered the burn up and the detailed power distribution in the fuel elements including the low leakage elements in the core edge. The calculations were compared with ex-vessel activation measurements. For that Russian and German fluence monitors were installed in the cavity. For their activities a mean calculation/experiment-ratio of C/E=1.01 and a mean standard deviation of 9% have been achieved. Moreover, the calculated fluence spectra were adjusted to the measurements to further improve the accuracy.

*H. Kumpf,*
*S. Collatz*[1]

**Recriticality after core damage accidents in Ligth Water Reactors**

Increased safety requirements demand a careful analysis of the possibilities for the formation of critical fuel configurations after core damage accidents in Light Water Reactors. Therefore a research project has been launched to analyze the neutron-physical properties of typical moderator/fuel configurations. Typical in- and ex-vessel scenarios and configurations have been identified in the framework of a conceptual study. The needed software to generate stochastic geometries for the following Monte Carlo criticality calculations has been developed and linked to MCNP.

From a number of MCNP calculations for various fuel-water-configurations those most endangered by recriticality could be identified.

[1] *Visitor to the Institute of Safety Research*

*H.-U. Barz,*
*B. Boehmer*

**Transport simulation of high energy ions and of fragmentation products**

The existing ion transport code that was developed to simulate the transport of high energetic, light ions through human tissue during cancer treatment has been improved with respect to several issues. The semiempiric fragmentation model of Sihver was supplemented by the Morrissey method. Some investigations were done concerning the free distance parameter of the Bohr model for electron straggling. It was found that the energy deposition is rather insensitive to this parameter.

The code was applied to study the electron density approximation and to calculate the production and transmission of protons. It could be shown, that the electron density approximation , i. e. to consider the tissue as water with the same electron density as the real composition, provides almost the same energy dose distribution as the exact treatment. The proton calculations were performed to estimate the dose contribution due to light particles. It was assumed that the fragmentation yield of neutrons is the same as that for protons.

Work was started to replace the semiempiric fragmentation models by an extended internuclear cascade model. First calculations were performed using the Russian Monte Carlo hadron transport code SHIELD.

*R. Küchler,*
*K. Noack*

**Migration of radioactive isotops**

The problem of the dumps that have been produced from wastes of uranium mining is of great environmental concern for Saxonia. Unsaturated water flow within subsurface regions of mining dumps controls various large-scale hydrological and geochemical processes. The aim of this subject is to calculate the release of radioactive isotops due to these processes. The problem to be solved can be subdivided into two steps:

1. the simulation of water flow through the dump and
2. the calculation of the water-carried pollutant transport.

A two-dimensional code for the calculation of the unsaturated water flow has been developed and needs verification by experimental data. The elaboration of a numerical reaction model describing the relevant chemical interactions during the transport of uranium isotops is in progress.

*St. Krahl, K. Noack, G.Otto, S. Collatz*[2]

*[1]supported by SMWK and BMBF*

*[2]Visitor to the Institute of Safety Research*

**Physics data base of a plasma neutron source**[1]

The collaboration between the Institute of Safety Research (ISR) and the Budker Institute Novosibirsk (BIN) is directed to the project of a plasma neutron source. After a substantial upgrade of the vacuum system of the "Gasdynamic Trap" facility (GDT) at the BIN a series of benchmark experiments was carried out. Some of them were remotely controlled via Internet from Rossendorf. These experiments were especially devoted to the verification of the neutral gas transport code TUBE coupled with the fast ion code FIT which have been developed by the ISR. The agreement between numerical and experimental results is satisfying. Hence, the neutral gas dynamic during a plasma shot can be clearly interpreted on the base of the code models.

## Mechanical integrity of technical systems and process monitoring

*E. Altstadt, M. Scheffler, G. Grunwald, F.-P. Weiß*

**Vibration modelling of russian type VVER reactors**

The work contributes to the improved evaluation of the mechanical integrity of the russian-type VVER reactors especially, to a sensitive early failure detection and to the localization of mechanical damages of reactor components by means of vibration monitoring. For that purpose the mechanical vibration of all primary circuit components was modelled by finite elements.

The interaction between the coolant flowing in the downcomer and the vibrating components has been considered by a fluid-structure element, which describes additional mode selective damping and intertia due to the coolant displacement when the downcomer geometry changes.

For the adjustment of the model dedicated experiments were performed at original VVER-440s. Now, the model for the WWER-440 can be regarded to be widely verified. It was applied to clarify how hypothetical damages of reactor internals influence the vibration signature of the primary circuit. Such kind of damage simulation is an appropriate means to find sensitive measuring positions for on-line monitoring and to define physically based threshold values.

In principle, the model is even suited to estimate the loads of reactor components which might be imposed by external events (explosion, earthquake).
A vibration model for the WWER-1000 type was elaborated as well. The adjustment of this model is still under work.

*E. Altstadt, F.-P. Weiß, M. Werner, H.-G. Willschütz*

**Structural and thermal behaviour of boiling water reactor (BWR) components during accident related loads**

In cooperation with the utility of a 1300MW BWR in-vessel components (shroud, upper and lower core structure, steam separator, feed water distributor) were modeled based on the finite element method. The models were assembled from 3D structural and thermal elements using temperatur dependent material properties.
In the simulation the components were exposed to temperature transients and pressure waves due to emergency core cooling after station black-out or to the break of the feed water line. The resulting structural displacements and the stresses were calculated showing that the integrity of the components can be maintained.
Moreover a global vibration model is available, mainly assembled from 1D pipe elements and stiffness matrices for element coupling, that can be used to estimate the component loads from external events like earthquake and explosion pressure wave.

*G. Hessel, W. Schmitt, N. Tefera, K. van der Vorst, F.-P. Weiß*

**Simulation of hazardous states in semibatch reactions**

Investigations on hazardous states in semibatch reactions were carried out in a laboratory reactor at Oberhausen. In particular, safety relevant faults such as loss of cooling, stirrer failure, inappropriate feed rate of reactant, inappropriate concentration of catalyst, and different temperatures were examined in a strongly exothermic chemical standard reaction. These experimental data were used to validate the dynamic process-simulation software (BatchCAD, CASI), to find efficient features for classifying faults, and to test supervision methods based on neural networks.
A comparison between experimentally and numerically simulated faults showed that stirrer faults, often occurring in industrial plants, could not be correctly simulated because in this case the point kinetic approximation is not valid.
Using a special probe for in-pile measurement during stirrer faults, it was found that even in a small reactor there is an extreme irregularity in the axial temperature profile which, due to the accumulation of reactants, could initiate a runaway reaction after the restart of the agitation.

To classify even faulty process states which involve simultaneously more than one fault, the supervision method based on a neural network was modified and successfully tested with experimental data.

*M. Beyer, H. Carl, A. Seidel, P. Schumann, J. Zschau*

**Realization of a remote monitoring system for the operational monitoring of the Zaporozh'ye nuclear power plant (Unit 5) by the State Supervisory Authority of Ukraine - Third level of realization -**

After the improvement of the user software by the scientific and technical centre of the Ukrainian supervisory authority and the operator, to which the German partners contributed by consultative support, and after the reliability verification under nuclear power plant conditions, the industrial testing phase of the system was started in the middle of 1996. Since then, supervisory authority and operator have been able to fulfil their monitoring duties more efficiently than before by direct access to the actual operational data.

The level achieved in the application of the operational, radiological and meteorological measuring channels supplied in 1995/96 required further support to the Zaporozh'ye NPP by FZR and the partner TÜV Rheinland. For the completion of the technical system in the Zaporozh'ye NPP by integrating all six units and both auxiliary buildings a financial effort of about 430 000,- DM is estimated. For the information transfer between the Zaporozh'ye NPP and the Kiev Centre the Ukrainian supervisory authority will make available a special data line.

*sponsered by BMU.*

## Hazard ranking and risk management for waste deposits

*S. Kruber, W. Ferse*

**The application of decision analysis to the remediation decision**

In 1996 the investigations about the application of decision analysis to remediation decisions at contaminated sites (with the municipal waste disposal site 'Bergen' as demonstrational object) were completed. In co-operation with the responsible state authorities, case- and person-specific utility functions were determined. The combination of these utility functions with the previously constructed and evaluated remediation concepts gave a final ranking of the concepts. As a result it was shown, that the standard procedure of decision analysis cannot directly be applied for decision in the public sector. New approaches were developed, to facilitate the determination of utility functions and represent complex, recursive decision problems.

*W. Ferse, T. Reitz*

**The development of the risk assessment system XUMA /GEFA**

XUMA/GEFA is a knowledge based program system for the uniform evaluation of environmental hazards due to contaminated sites. XUMA/GEFA which has been developed in co-operation with the Research Centre Karlsruhe and the Technical University of Dresden was designed to assess conventionally polluted sites.

In 1996 different methods and programs for the evaluation of military sites were investigated. The goal of this study was to analyse whether the data structure of the knowledge base of XUMA/GEFA also allows to implement special criteria and rules for the evaluation of military sites. It could be shown that the knowledge acquisition tool of XUMA/GEFA is flexible enough to manage this problem. The necessary changes of the knowledge base content have been carried out.

*A. Polte, W. Ferse*

**The application of decision analyses to the comparative assessment of industrial facilities in urban areas**

In 1996 first investigations concerning the application of decision analyses to the assessment of industrial facilities in urban areas were started. The first step was to generate a comprehensive list of decision criteria, related to planning and siting hazardous industrial facilities. With the help of these criteria it shall be possible to analyse the different techniques and/or sites concerning their effects on human health, individual quality of life, social impacts, environmental and economic impacts.

The criteria which are based on several international investigations, mainly on the Polyproject "Risk and Safety of Technical Systems" of ETH Zürich, were adapted to the specific conditions in Saxony.

## Magneto-hydrodynamics of conductive fluids

*S. Eckert, G. Gerbeth, H. Langenbrunner, W. Witke*

**Local velocity measurements in a turbulent MHD channel flow**

The streamwise velocity component and their fluctuations were measured in a sodium flow exposed to an external transverse magnetic field by means of own developed potential probes. The experiments were performed in the new test section of the Rossendorf sodium facility.

The rectangular channel was equipped with special inserts (honeycombs, wall channel inserts, turbulence promoters) in order to guarantee defined hydraulic inlet and electrical boundary conditions, respectively. The results indicate the existence of quasi-two-dimensional vortices in the flow being typical for turbulent MHD flows at high Hartmann numbers. The

measurements are in good qualitative agreement with other authors, but cover higher values of the Hartmann number and the MHD interaction parameter, too.

*supported by DFG*

*F. Stefani, G. Gerbeth*

**Velocity profile optimization for the Riga dynamo experiment**

The Riga dynamo experiment is intended to verify for the first time the magnetohydrodynamic dynamo effect in a laboratory set-up. One of the main problems for this experiment is the strong dependence of the magnetic field self-excitation threshold on the shape of the axial and azimuthal velocity profiles. A wide variety of profiles have been tested numerically in order to minimize the critical magnetic Reynolds numbers. Helicity maximizing profiles (Bessel Functions) were shown to reduce the critical Rm by 20 per cent.

*supported by DFG*

*A. Cramer, G. Gerbeth*

**Experimental study of liquid metal surfaces**

Measurements on free liquid gallium surfaces performed with the first special vacuum box containing Gallium with a purity of 99.99% indicated an inversed coefficient of surface-tension temperature dependence compared to the usually reported negative values of pure elements. The transition of the flow structure was directly from the inversed direction, steady flow to a turbulent regime.

A second series of experiments were thus carried out with a different container filled with higher purity (99.9999%) liquid Gallium. For small temperature gradients the inversed motion could be verified, but increasing it to even the highest reachable values was not followed by the transition sequence observed at the first box. For a certain mean temperature the steady, laminar flow changes its direction. Convergent flows from hotter and colder regions to that at mean temperature clearly indicate a change of sign in the temperature-coefficient of surface-tension. The experiments show that the usually reported, constant negative values of the derivative of surface-tension to temperature do not hold for practical applications. Even very small concentration of impurities have significant influence on the whole bulk fluid motion because they are enriched at the temperature-sensitive free surface.

## Renewable energies

*H. Futterschneider, U. Rindelhardt, G. Teichmann*

### Investigations on photovoltaic (PV) systems

Based on the analysis of a 43 years irradiation data serie (Dresden-Wahnsdorf) sizing rules for stand alone PV systems were provided. The values of sizing irradiation and system autonomy were derived from a statistical analysis, taking into account realistic properties of the system components. In the case of a continuously operating load (load power P) the nominal generator power was estimated to be 30*P and the needed system autonomy (battery size) must be 14 days. The results could be proven by monitoring two stand alone systems during the winter 1995 to 1996.

The long time monitoring programme of 50 small grid connected PV systems in Saxony was continued. The concerned PV systems were installed in the frame of the "1000-Roofs-Programme" between 1992 and 1994. Technical inspections at 25 systems, which include also measurements of the generator I-U-characteristics, were carried out in 1996.

*supported by BMBF*

### Comparison of wind energy calculations with different codes

*D. Brünig, W. Hirsch, U. Rindelhardt*

The wind energy ressources of a selected Saxon area (64 km x 48 km) were investigated in detail. The region is characterized by a mean height of 200 m a.s.l. with a complex surface profile. Based on measuring data from three stations WASP calculations with a grid step of .25 km were performed for the whole region. The results were compared with calculations of the mesoscale models KAMM and AIOLOS, which were performed at the Universities of Karlsruhe and Oldenburg, resp. Both mesoscale models used the geostrophic wind measured in Prague (Czech Republic) as driving force.

The comparison showed unacceptable differencies between the 3 codes. Therefore further investigations are needed about the use of mesoscale models for wind climate predictions.

*supported by SMU*

# Publications

# Publications in scientific and technical journals and in conference proceedings

**Anikeev, A. V., e. a., K. Noack, H. Kumpf, St. Krahl, G. Otto**
Plasma confinement and stability studies in the gas-dynamic trap experiment
16. IAEA fusion energy conferency, IAEA-CN-64/CP-22
Montreal, Canada, October 7-11, 1996

**Aszodi, A.**
Simulation der transienten Naturkonvektion in einem seitlich beheizten Behälter
Jahrestagung Kerntechnik '96
Mannheim, 21. - 23. Mai 1996, Tagungsbericht S. 106 - 109

**Aszodi, A., P. Liewers, E. Krepper, H.-M. Prasser**
Investigation of an externally heated storage vessel
3. Fachtagung Anlagen-, Arbeits- und Umweltsicherheit
Köthen, 7./8. November 1996, Preprints, S. 251 - 258

**Barz, H.-U., B. Böhmer, J. Konheiser, I. Stephan, G. Borodkin**
Determination of Pressure Vessel Neutron Fluence Spectra for a low Leakage Rovno-3 Reactor Core Using Three Dimensional Monte Carlo Neutron Transport Calculations and Ex-vessel Neutron Activation Data
Proc. of the 9. International Symposium on Reactor Dosimetry
Prague, Sept. 2-6, 1996

**Barz, R.-U., G. Gerbeth, U. Wunderwald, E. Buhrig. Yu. M. Gelfgat**
Modelling of the Isothermal Melt Flow due to Rotating Magnetic Fields in Crystal Growth
Int. Workshop on Modelling in Crystal Growth
Durbuy (Belgien), Oct. 13-16, 1996, to appear in: J.Crystal Growth

**Bergner, F., U. Bergmann, U. Fleischer**
Das Konzept des Ultraschall-Laufzeit-Prozeßablauf-Bildes
Seminar für zerstörungsfreie Materialcharakterisierung
Jena, Okt. 1996, Berichtsband 54, DGZfP, S. 253-258

**Bergmann, U., F. Berner, K.-J. Langenberg, Ch. Hofmann**
Ultrasonic Time-of-Flight Diffraction Method for Monitoring Stable Crack Growth
Proc. of the 14th World Conference on NDT
New Delhi, December 8-13, 1996, pp. 2325-2328

**Bergmann, U.**
Mathematisch-numerische Modellierung der Ultraschallstreuung an oberflächenverbundenen Rissen mit dem EFIT-Code
Nova Acta Leopoldina Supplementum Nr. 14, S. 361-376 (1996)

**Bergmann, U., F. Bergner, J. Böhmert**
Rißfortschrittsmessung an Dreipunkt-Biegeproben mit Ultraschall
Vortrags- und Diskussionstagung "Werkstoffprüfung 1996"
Bad Nauheim, 5.-6.12.1996, Tagungsband S. 143-151

**Beyer, M., H. Carl, B. Schikora, P. Schumann, A. Seidel, J. Zschau, K. Nowak, P. Tolksdorf**
Fernüberwachung ukrainischer Kernkraftwerke
Jahrestagung Kerntechnik '96
Mannheim, 21.-23. Mai 1996, Tagungsbericht S. 476-479

**Beyer, M., H. Carl, P. Schumann, A. Seidel, F.-P. Weiß, J. Zschau**
A technical system to improve the operational monitoring of the Zaporosh'ye nuclear power plant (remote monitoring system in Ukraine - first level of realization)
Proc. of the FOURTH INTERNATIONAL WORKSHOP on real-time computing of the environmental consequence of an accident release from a nuclear installation
Aronsborg, Sweden, Oct. 07-11, 1996, Paper-No. 82

**Beyer, M., H. Carl, K. Nowak, P. Schumann, A. Seidel, F.-P. Weiß, J. Zschau**
A technical system to improve the operational monitoring of the ukrainian nuclear power plant Zaporosh'ye (Unit 5)
Proc. of the OECD/NEANSC Specialists' meeting on in-core instrumentation and reactor core assessment
Mito-shi, Japan, Oct. 14-17, 1996, Paper-No. 88

**Bojarevics, A., Y.Gelfgat, G.Gerbeth, S.Simanovskis, J. Maniks**
Procedure and method of MHD phenomena investigation on juvenile surfaces of liquid metal
8th Beer-Sheva Int. Seminar on MHD flows and turbulence
Jerusalem, February 1996, to appear in: Progress in Astronautics and Aeronautics, Ed.: H. Branover, Y. Unger, Washington

**Böhmer, B., G. Manturov**
Influence of Input Neutron Spectrum Covariances on Results of Pressure Vessel Neutron Spectrum Adjustments
Proc. of the 9th International Symposium on Reactor Dosimetry
Prague, Sept. 2-6, 1996

**Böhmert, J., M. Große, H.-W. Viehrig**
Einfluß bestrahlungsinduzierter Ausscheidungen auf die Zähigkeit von Cr-Mo-V-legierten Reaktordruckbehälterstählen
28. Tagung DVM-Arbeitskreises Bruchvorgänge
Bremen, 26./27. Feb., DVM-Bericht 228, S. 173-182

**Böhmert, J., K. Törrönen, M. Valo**
Nachuntersuchungen an Reaktordruckbehältern des stillgelegten KKWs Greifswald - eine Chance zur realistischen Bewertung der Neutronenversprödung
Jahrestagung Kerntechnik '96
Mannheim, 21.-23. Mai 1996, Tagungsbericht S. 176-179

**Brockmann, R., R. Henkel, U. Rindelhardt**
40-$KW_p$-Photovoltaikanlage Kirnitzschtalbahn
11. Symposium Photovoltaische Solarenergie
Staffelstein, 13.-15. März 1996, Tagungsband S. 289-293

**Eckert, S., G. Gerbeth, H. Langenbrunner, W. Witke**
MHD turbulence measurements in a sodium channel flow
8th Beer-Sheva Int. Seminar on MHD flows and turbulence
Jerusalem, February 1996, to appear in: Progress in Astronautics and Aeronautics, Ed.: H. Branover, Y. Unger, Washington

**Ferse, W.**
A Computer System for Evaluation of Contaminated Sites
Environmental Engineering and Pollution Prevention - European Network of Excellence and Partnership
NATO ASI Series: Environment - Vol. 8, Kluwer Academie Publishers, 1996

**Ferse, W., Reitz, Th.**
A Risk Evaluation System for Contaminated Sites
Proc. of the FOURTH INTERNATIONAL WORKSHOP on real-time computing of the environmental consequence of an accident release from a nuclear installation
Aronsborg, Sweden, Oct. 07-11, 1996, Paper No. 82a

**Galindo, V., M. Teuner, G. Gerbeth, D. Langbein**
Drop tower experiments on the thermocapillary drop migration
Proceedings Drop Tower Days
Bremen, July 8-11, 1996, pp. 2-10

**Gerbeth, G., G. Mutschke, V. Shatrov**
Cylinder wake control by magnetic fields in liquid metal flows
Flow Control-Workshop
Cargese, July 1-5, 1996; to be published in:
Int. J. of Experimental Heat Transfer, Thermodynamics, and Fluid Mechanics

**Große, M., A. Hempel, J. Böhmert, G. Brauer, F.M. Haggag**
Influence of the Irradiation Temperature on the Formation of Defects in Reactor Pressure Vessel Steels
Proc. of the MRS Fall Meeting 1996
Boston (USA), Dec. 2-6, 1996

**Große, M., G. Brauer, P. Nitzsche, J. Böhmert, G. Goerigk**
ASAXS-Investigation of the Structural Changes in Laboratory Heats of the Reactor Pressure Vessel Steel 15 Kh2MFA after Irradiation in a Nuclear Power Plant
DESY, Jahrsbericht 1995, HASYLAB am Deutschen Elektronen-Synchrotron
Annual Report II, Jan. 1996, S. 833

**Große, M., P. Nitzsche, J. Böhmert, G. Brauer**
Investigation of the Development of Irradiation - Induced Precipitates in VVER-440-Type Reactor Pressure Vessel Steels and Weld Metals During Irradiation and Annealing
Proc. of the 18. Int. Symposium "Effects of Radiation in Materials"
Hyannis (USA), June 25-27, 1996, ASTM STP 1325

**Große, M., A. Hempel, J. Böhmert, F. Eichhorn, C. Riekel, P. Engström**
SAXS Investigation of the Structural Changes in the Plastic Zone Ahead of a Crack Tip in Ductile Metals
Journal of Molecular Structure 383 (1996) S. 267-270

**Grundmann, U., S. Kliem, D. Lucas, U. Rohde**
Coupling of the termohydraulic code ATHLET with the 3D neutron kinetic model DYN3D
Proceedings of the 6th symposium of AER
Kirkkonummi, Finland, Sept. 23-26, 1996, pp. 179 - 191

**Grundmann, U., U. Rohde**
The reactor code DYN3DR - transient calculations of NEACRP benchmarks for PWR and BWR
Jahrestagung Kerntechnik '96
Mannheim, 21.-23. Mai 1996, Tagungsbericht S. 23 - 26

**Grundmann, U., U. Rohde**
DYN3D - a 3D Core Model for Steady State and Transient Analysis in Thermal Reactors
Proc. of the Int. Conf. on Physics of Reactors PHYSOR'96,
Mito (Japan)16.-20.09.96, pp. J-70 - J-79

**Heinemann, D., R. Müller, H. P. Waldl, W. Hirsch, U. Rindelhardt**
Windpotentialmodellierung in komplexen Gelände
DEWEK 96
Wilhelmshaven, 23. - 25.10.1996, Tagungsband S. 334-337

**Hensel, F.**
Untersuchung von Zweiphasenströmungen gasförmig/flüssig mit Positronenemittern
Kraftwerkstechn. Kolloquium
Dresden, 29.-30. Oktober 1996, Tagungsband I, S. 101

**Hessel, G., W. Schmitt, F.-P. Weiß**
A Neural-Network Approach for Acoustic Leak Monitoring at Pressurized Plants with Complicated Topology
Control Engineering Practice, Vol. 4, No. 9,1996, pp. 1271-1276

**Hessel, G., W. Schmitt, K. van der Vorst, F.-P. Weiß**
Akustische Lecküberwachung mit neuronalen Netzen an Druckanlagen komplizierter Topologien
TÜ - Techn. Überwachung, Bd. 37 (1996), Nr. 4, S. 17-21

**Hessel, G., W. Schmitt, K. van der Vorst, F.-P. Weiß**
Comparison between Neural Networks and Fuzzy Classification for Acoustic Leak Monitoring
Proc. of EUFIT '96
Aachen, Sept. 2-5, 1996, pp. 1492-1496

**Hessel, G., Schmitt, W., van der Vorst, K., Weiß, F.-P.**
Anwendung neuronaler Netze zur akustischen Leckortung und Leckratenabschätzung
IV. Kolloquium "Technische Diagnostik"
Dresden, 14./15.03.1996, Tagungsband S. 203-211

**Hessel, G., W. Schmitt, K. van der Vorst, F.-P. Weiß**
Anwendung neuronaler Netze zur Identifizierung gefährlicher Betriebszustände in Chemieanlagen
3. Fachtagung Anlagen-, Arbeits- und Umweltschutz
Köthen, 7./8. Nov. 96, Preprint S. 141-147

**Hessel, G., W. Schmitt, K. van der Vorst, F.-P. Weiß, J. Neumann, S. Schlüter**
Anwendungsmöglichkeiten neuronaler Netze zur Früherkennung in Chemieanlagen
DECHEMA-Jahrestagung '96
Wiesbaden, 21.-23. Mai 1996, Tagungsband II, S. 86-88

**Hirsch, W., U. Rindelhardt, G. Tetzlaff**
Saxon Wind energy ressources: Comparison of WASP and KAMM results
Proc. of the EUROPEAN UNION WIND ENERGY CONFERENCE
Göteborg, 20.-24. Mai 1996; pp. 604-607

**Hollstein, F.**
Nodales Modell zur Berechnung des Neutronenflußrauschens infolge zufälliger Regelelementschwingungen in WWER-440-Reaktoren
Jahrestagung Kerntechnik '96
Mannheim, 21.-23. Mai 1996, Tagungsbericht S. 79

**Ihle, T., U. Rindelhardt, G. Teichmann**
Betriebsverhalten von netzgekoppelten Photovoltaikanlagen aus dem 1000-Dächer-Programm
11. Symposium Photovoltaische Solarenergie
Staffelstein, 13.-15. März 1996, Tagungsband S. 294-298

**Kolevzon, V., G. Gerbeth**
Light scattering analysis of waves destabilization at a liquid gallium surface
Proceedings of the Second European Symposium Fluids in Space
Neapel, April 22-26, 1996, pp. 447-453

**Kolevzon, V., G. Gerbeth**
Light scattering spectroscopy of a liquid gallium surface
J. Physics D: Applied Physics, Vol. 29, 2071-2081, 1996

**Kossok, N., H.-M. Prasser, P. Schütz**
Messung der Volumenströme von Gas und Flüssigkeit in einer Zweiphasenströmung mit Ultraschall und Mustererkennung,
Kraftwerkstechn. Kolloquium
Dresden, 29.-30. Oktober 1996, Tagungsband I, S. 121

**Krepper, E.**
Post test calculations for a small break loca experiment at the integral test facility ISB-VVER using the thermalhydraulic code ATHLET
Jahrestagung Kerntechnik '96
Mannheim, 21. - 23. Mai 1996, Tagungsbericht S. 122 - 125

**Kyrki-Rajamäki, R., U. Grundmann, A. Kereszturi**
Results Three-Dimensional Hexagonal Dynamic Benchmark Problems for VVER Type Reactors
Proc. of the Int. Conference on the Physics of Reactors PHYSOR '96
Mito (Japan), 16. - 20.09.1996, pp. J-229 - J-238

**Lucas, E., H.-M. Prasser**
Schwankungen des Massenstroms bei Druckentlastungsvorgängen
3. Fachtagung Anlagen-, Arbeits- und Umweltsicherheit
Köthen, 7./8. Nov. , Preprint S. 233 - 240

**Mach, M., K. Vanoli, U. Luboschik, P. Schalajada, M. Schnauss, G. Valentin, A. Gassel, U. Rindelhardt**
Measured hot water consumption in apartment buildings as key design parameter for solar collector installations
Proc. of Eurosun '96
Stuttgart, September 1996, Vol. 1, pp. 246-250

**Markina, N. V., Riasanov, D. K., Tellin, A. I., Lichadeev, V. V., Pavlov, V. V., Tsikanov, V. A., Brodkin, E. B., Egorov, A. L. Zaritsky, S. M., Bars, B., Stephan, I., Voorbrack, W., Nolthenius, H., Ait Abderrahim, H.**
Experimental and Calculation Characterization of Irradiation Facility KORPUS
Proc. 9th Internat. Symp. on Reactor Dosimetry
Prague, Sept 2-6, 1996

**Mittag, S.**
Burnup and Rod Worth Calculations for Paks-2 Using the Code DYN3D with two Different Group Data Librarres
Proc. of the 6th Symposium of AER,
Kirkkonummi (Finland), 23. - 26.09.1996, p. 499

**Mutschke, G., G. Gerbeth, V. Shatrov**
2-D and 3-D instabilities of cylinder wake in external magnetic fields
Bulletin Am. Phys. Society, vol. 41, No. 9, 1996, p. 1715

**Noack, K., A. D. Rogov**
Experiences with the parallel version of MCNP-4A on a SUN workstation network and on the CONVEX SPP-1000system
Proc. of the International Conference on Computation Modelling and Computing in Physics
Dubna, Russia, Sept. 16-21, 1996, p. 52

**Prasser, H.-M., A. Thess**
Spektrale Simulation in einer Blasensäule
DECHEMA-Jahrestagung '96
Wiesbaden, 21.-23. Mai 1996, Band II, S. 308-309

**Priede, J., G. Gerbeth**
On the role of thermal boundary conditions in the instability of thermocapillary driven low-Prandtl-number convection
Proc. of the Second European Symposium Fluids in Space
Neapel, April 22-26, 1996, pp. 508-511

**Richter, H., J. Böhmert, H.-W. Viehrig**
Determination of Crack-Initiation Toughness by Impact and Dynamic Testing
Proc. of the 11th European Conference on Fracture - ECF 11,
Poitiers-Futurscope, France, Sept. 1996, Vol. III, pp. 2001-2006

**Rindelhardt, U., H. Futterschneider, J. Garche, L. Schulze**
Sizing and Testing of Stand Alone PV Systems
Proc. of Eurosun '96,
Stuttgart, September 1996, Vol. 2, pp. 848-852

**Shatrov, V., G. Mutschke, G. Gerbeth**
A numerical 3d stability analysis of the MHD cylinder wake flow
8th Beer-Sheva Int. Seminar on MHD flows and turbulence
Jerusalem, February 25-29, 1996, to appear in: Progress in Astronautics and Aeronautics, Ed.: H. Branover, Y. Unger, Washington

**Treuner, M., V. Galindo, G. Gerbeth, D. Langbein, H.J. Rath**
Thermocapillary bubble migration at hight Reynolds and Marangoni numbers under low gravity
International Journal of Colloid and Interface Science, vol. 179, No. 1, pp. 114-127 (1996)

**Valo, M., J. Böhmert, U. von Estorff, K. Törrönen**
Post-Service investigation of Material from the RPV's of Greifswald NPP
Proc. of the CSNI/CEC Workshop on Aged and Decommissioned Material Collection and Testing for Structural Integrity Purposes
Mol (Belgium), June 1995, OCED/GD (1996) 10, pp. 131-146

**Viehrig, H.-W., J. Böhmert**
Sichere Bewertung des Materialzustandes in Altanlagen durch Probenkonstitution
INNOMATA 1996, 2. Ausstellungstagung für Materialtechnologie und Werkstoffanwendung
Dresden, Mai 1996, Comp. S. 323

**Viehrig, H.-W., J. Böhmert**
Erweitertes Überwachungsprogramm der Strahlenversprödung durch Probenrekonstitution
Jahrestagung Kerntechnik '96
Mannheim, 21.-23. Mai 1996, Tagungsbericht S. 172-175

**Weier, T., G. Gerbeth, G. Mutschke, O. Lielausis, E. Platacis**
Separation control of the cylinder wake using surface localized electromagnetic forces
Bulletin Am. Phys. Society, 41, No. 9, 1996, p. 1750

**Weier, T., G. Gerbeth, G. Mutschke, E. Platacis, O. Lielausis**
Experiments on cylinder wake stabilization in an electrolyte solution by means of electromagnetic forces localized on the cylinder surface
Workshop "Flow Control"
Cargese (France), 1-5 July 1996, to be published in: Int. J. of Experimental Heat Transfer, Thermodynamics, and Fluid Mechanics

## Conference contributions

**Altstadt, E., G. Grunwald, F.-P. Weiß**
Ein FE-Schwingungsmodell zur Unterstützung der Diagnose von Reaktoren des Typs WWER
IV. Kolloquium "Technische Diagnostik"
Dresden, 15. März 1996

**Bergmann, U., F. Bergner, J. Böhmert**
Rißfortschrittsmessung an Dreipunkt-Biegeproben mit Ultraschall
Vortrags- u. Diskussionstagung "Werkstoffprüfung 1996"
Bad Nauheim, 5.-6. Dez. 1996

**Beyer, M., H. Carl, B. Schikora, P. Schumann, A. Seidel, J. Zschau, K. Nowak, P. Tolksdorf**
Ein technisches Informationssystem zur verbesserten betrieblichen Überwachung des Kernkraftwerkes Saporoshje/Ukraine
Postervortrag zum IV. Kolloquium "Technische Diagnostik"
Dresden, 14.-15. März 1996

**Bojarevics, A., Yu. Gelfgat, G. Gerbeth**
A novel experimental technique to study different phenomena at a free liquid metal surface
The 125th TMS meeting, Experimental methods in Microgravity
Anaheim (USA), February 4-8, 1996

**Bojarevics, A., Yu. Gelfgat, G. Gerbeth, A. Cramer**
Second Experimental studies on different phenomena at free liquid metal surface
European Symposium Fluids in Space
Neapel, April 22-26, 1996

**Böhmert, J., M. Große, P. Nitzsche**
SANS Investigations of the Irradiation-Caused Structural Damages in VVER-440-Type Reactor Pressure Vessel Steels
1st European Conference on Neutron Scattering
Interlaken (Switzerland), Oct. 1996

**Ferse, W.**
Die Struktur des wissensbasierten Systems XUMA-GEFA,
Seminar der Anwenderländer des Baden-Württemberger Altlastenbewertungssystems
Bad Schandau, August 1996

**Ferse, W.**
Die Anwendung der Entscheidungsanalyse zur Unterstützung öffentlicher Entscheidungen
KOVERS-Seminar, ETH Zürich, 28. November 1996

**Galindo, V., M. Treuner, G. Gerbeth**
Experiments on thermocapillary migration of drops in a drop tower
Escuela de Fisico-Quimica de Fluidos: Drops, bubbles and film
Santander, September 9-13, 1996

**Gebbeken, B., H.-M. Prasser, R. Eggers**
Entspannungsverdampfung während der Druckentlastung von $CO_2$ aus dem überkritischen Anfangszustand
GVC-Fachausschuß Mehrphasenströmungen, Vortrag 2.27
Lahnstein, 06.-08. März 1996

**Hensel, F.**
Dichtemessung mit Positronenstrahlung
ACHEMA '97, Frankfurt/M.

**Kossok, N., H.-M. Prasser, P. Schütz**
Identifikation und diagnostische Überwachung von Zweiphasenströmungen in Rohrleitungen
IV. Kolloquium "Technische Diagnostik"
Dresden, 15.03.1996

**Kruber, S.**
Die Praxis-Anwendung der Entscheidungsanalyse für die Bewertung und Auswahl optimaler Sanierungskonzepte,
KOVERS-Seminar
ETH Zürich, 28. September 1996

**Langenbuch, S., M. Lizorkin, U. Rohde, K. Velkov**
3D Neutronic Codes coupled with Thermal-hydraulic System Codes for PWR, BWR and VVER Reactors
OECD/CSNI Workshop on Transient Thermal-Hydraulics and Neutronic codes Requirements
Annapolis, Md (USA), November 5-8, 1996

**Meyer, K., F. Hollstein**
Analytical Model to Calculate the Transfer Functions of Neutron Noise coused by Random Pendulum Motions of a VVER-440 Control Element
IMORN-26
Piestany, May 27 - 29, 1996

**Polte, A.**
Diskusion eines Kriteriensystems zur Bewertung der Ansiedlung von Industrie un urbanen Gebieten
KOVERS-Seminar
ETH Zürich, 28. November 1996

**Prasser, H.-M.**
BLDN - Modell zur Berechnung der axialen Dampfgehaltsverteilung bei der Druckentlastung
42. Sitzung des DECHEMA/GVC-Arbeitsausschusses "Sicherheitsgerechtes Auslegen von Chemieapparaten
Rossendorf, 15.-16.10.1996

**Prasser, H.-M., H. Steinkamp, G. Wehmeier**
Dampfgehaltsmessungen bei der Druckentlastung von Ethanol
42. Sitzung des DECHEMA/GVC-Arbeitsausschusses "Sicherheitsgerechtes Auslegen von Chemieapparaten
Rossendorf, 15.-16.10.1996

**Schikora, B., J. Zschau**
Parallele Erfassung und Übertragung nicht synchronisierter Datenströme aus mehreren Echtzeitrechnern
Workshop Modular Computers
Dresden, 27.06.1996

**Schikora, B., J. Zschau, H. Wiedemann**
OS/9-Anwendung zur parallelen Erfassung nicht synchronisierter Datenströme aus mehreren Echtzeitrechnern
OS/9-Konferenz des Europ. Forums für OS/9
Emmetten, 20. - 22.09.1996

**Viehrig, H.-W., J. Böhmert, H. Richter**
Determination of Fracture Mechanical Values Using Charpy Size SENB Specimens and Correlation with Charpy-V Impact Test Results
AMES TG1C Workshop on Property-Property Correlation
Petten, 1-2 Oct. 1996

**Viehrig, H.-W.**
Herstellung und Prüfung von Charpy-V-Verbundproben
Jahressitzung 1996 der DVM-Arbeitsgruppe "Instrumentierter Kerbschlagbiegeversuch"
Merseburg, 13.09.1996

**Zoller, J., E. Altstadt, G. Grunwald, W. Zimmermann**
Consideration of Added Stiffness Resulting from Edging Out of an Axial Annular Flow by Motions of the Pressure Vessel and the Pressure Vessel and the Core Barrel
IMORN 26
Piestany, May 27-29, 1996

## FZR-reports and other publications

**Altstadt, E., M. Scheffler, F.-P. Weiß**
Theoretische Modellierung des Druckbehälters und der Druckbehältereinbauten eines Siedewasserreaktors (SWR)
FZR-147, August 1996

**Beyer, M., H. Carl, B. Schikora, P. Schumann, A. Seidel, J. Zschau**
Lieferung von Investitionsgütern zur Erhöhung der Betriebssicherheit des Kernkraftwerkes Saporoshje - 2. Realisierungsstufe -
FZR-135, April 1996

**Beyer, M., H. Carl, B. Schikora, P. Schumann, A. Seidel, J. Zschau**
Aufbau eines behördlichen Fernüberwachungssystems zur betrieblichen Überwachung des KKW Saporoshje (Block 5) - 3. Realisierungsstufe -
Abschlußbericht, Anlage A: Fachbericht, Anlage B: Materialsammlung
Rossendorf, Dezember 1996

**Brünig, D., U. Rindelhardt**
Solare Warmwasserbereitung und Fernwärmeeinspeisung
- Waldblickschule Freital -
FZR-137, April 1996

**Ferse, W., Kruber, S.**
ECON - Ein System zur Lastmodellierung
Bericht Forschungszentrum Rossendorf, Institut für Sicherheitsforschung, 1996

**Ferse, W., Geiger, W., Reitz, Th. u.a.**
Spezifikation und Struktur der Altlastenbewertung mit dem Programmsystem XUMA-GEFA
Bericht Forschungszentrum Rossendorf, Institut für Sicherheitsforschung, 1996

**Futterschneider, H., W. Hirsch, U. Rindelhardt, G. Teichmann**
Elektroenergieerzeugung einer kombinierten Wind-Photovoltaik-Anlage in Ottendorf-Okrilla (Sachsen)
FZR-138, April 1996

**Hirsch, W., U. Rindelhardt**
Windmeßprogramm Sachsen, Teil
Abschlußbericht
Herausgeber: Sächs. Staatsministerium für Umwelt und Landesentwicklung
(Materialien zum Klimaschutz 1/1996)
Dresden, November 1996

**Kumpf, H., Noack, K.**
Application of the Guiding Centre Approximation to the Transport of Injected Fast Ions in a Mirror Based Plasma Neutron Source
FZR-121, 1996

**Kolevzon, V.**
Surface Light Scattering Spectroscopy of the Gallium Liquid-Vapor Interface
FZR-124, Februar 1996

**Schumann, P.**
Bestimmung eines repräsentativen Wertes aus einr Folge von Meßwerten
Fachbericht FWSF 02/96, August 1996

**Zoller, J.**
Added Stiffness Relating to Small Motions of two Concentric Cylinders Submitted to Axial Annular Incompressible Flow
FZR-146, August 1996

# Meetings and Workshops

## Meetings and Workshops

Arbeitstagung der Arbeitsgruppe SWR-Nachrüstung der Vereinigung der Großkraftwerksbetreiber
Rossendorf, 29. - 30. Januar 1996

6. Internationaler Workshop zum BMU-Vorhaben
"Fernüberwachung KKW Saporoshje"
Rossendorf, 18. - 22. März 1996

Workshop anläßlich des Besuches von Prof. Keßler und Prof. Kröger
Rossendorf, 29. - 30. April 1996

Internationales Arbeitstreffen zum BMU-Vorhaben
"Fernüberwachung KKW Saporoshje"
Rossendorf, 26. - 30. August 1996

24. Sitzung des DECHEMA/GVC-Arbeitsausschusses
"Sicherheitsgerechtes Auslegen von Chemieapparaten"
Rossendorf, 15. - 16. Oktober 1996

Work Meeting on Vibration Modelling of WWER Type Reactors
Rossendorf, 5. - 7. November 1996

Institute Seminars

# SEMINARS 1996

01. Dr. H. Kumpf
Ionentransport in der Plasmaneutronenquelle
25. 01.96

02. Dr. E. Krepper
Naturumlaufversuch am ISB-WWER
22. 02.96

03. Prof. A. Haghighat (Pennsylvania State University)
Development of parallel algorithms for neutron diffusion and transport calculations at the PSU
06.03.96

04. Dr. J. Böhmert
Der Verlauf der mechanischen Eigenschaften über die Dicke bei Schmiederingen für WWER-Reaktordruckbehälter
07. 03.96

05. H. Utke
Migration von Schadstoffen speziell im Hinblick auf die Situation von Schüttgütern (Halden) in Sachsen und Thüringen
12.03.96

06. T. Kern
Dynamik von Zellenschaum
21. 03.96

07. S. Elkin (Kurchatov-Institut Moskau, Institut für nukleare Sicherheit)
Analyse einer Speisewassertransiente im KKW Kalininskaja mit dem Code RELAP5/MOD3.2
28.03.96

08. Dr. H.-U. Barz, B. Böhmer
Berechnungen zum Ionentransport (Tumor-Therapie)
02.04.96

09. Dr. E. Altstadt, M. Scheffler
Überblick zur mechanischen Modellierung von DWR- und SWR-Komponenten mit der Finite-Elemente-Methode
02. 05.96

10. Dr. A. Kryukov (RCC Kurchatov-Institut Moskau)
New results on the characterization of irradiated materials from operating or decommisioned VVER-440-type nuclear power plants
31.05.96

11. Dr. Kozmenkov (IPPE Obninsk)
RELAP5/MOD3 application to the analysis of ABV-67 LOCA without scram

Dr. Kumayev (IPPE Obninsk)
Development of the Code DINCOR for numerical simulation of 2D thermo-hydraulics including melting and solidification processes in multicomponent systems
05.06.96

12. Dr. W. Schmitt, K. van der Vorst
Anwendung neuronaler Netze und Fuzzy-Klassifikatoren zur Fehlererkennung in chemischen Reaktoren
11. 06.96

13. Dr. A. Tilgner (Universität Bayreuth)
Numerische Untersuchungen zum homogenen Dynamo
18.06.96

14. Dr. G. Bauer (Paul Scherrer Institut Villigen, Schweiz)
Spallations-Neutronenquellen mit hoher Leistung und damit verbundene Targetprobleme
28.06.96

15. Dr. D. Lucas
Schwankungen des Massenstromes bei Druckentlastungsvorgängen
11.07.96

16. Dr. N. Kossok
Identifikation von Gas- und Flüssigkeitsströmen mit Ultraschall und autoregressivem Signalmodell
22.08.96

17. Dr. H. Steinkamp
Druckentlastung von Batch-Reaktoren
26.08.96

18. St. Kruber
EA-Anwendung bei Altlastensanierung
05.09.96

19. Dr. M. J. Zheleznyak (Kiev)
Modelling of Radionuclide Transport in Rivers and Reservoirs: Post-Chernobyl Experience
09.09.96

20. Dr. R. Stieglitz (Forschungszentrum Karlsruhe)
Geodynamo: Kann man das Erdmagnetfeld in einem Laborexperiment simulieren?
26.09.96

21. G. Mutschke, B. Bracher (TUD)
Parallelisierung von CFD-Codes
10.10.96

22. Dr. N. M. Sobolevsky (INR RAS Moskau)
Computer-Simulation of high-energy particle transport in complex systems
14.10.96

23. Dr. G. Jehmlich (Ludwig Bölkow Systemtechnik München)
Solarleuchten in Afrika
22.10.96

24. D. Pachur (KFA Jülich)
Deutung der Bestrahlungsversprödung
24.10.96

25. Dr. Kalkhof (PSI Villigen)
Forschungsarbeiten zur Bauteil- und Schadensanalyse am PSI Villigen
28.10.96

26. Dr. W. Bernnat (IKE Stuttgart)
Beiträge zur Entwicklung und Anwendung reaktorphysikalischer Daten und Methoden zur Auslegung und Sicherheitsanalyse von Leistungs- und Forschungsreaktoren
04.11.96

27. Dr. S. Molokov (Coventry University, UK)
Magnetohydrodynamic Flows in Rectangular Ducts in Strong Magnetic Fields
11.11.96

28. Dr. R. Küchler
Radionuklidtransport in Halden
21.11.96

29. M. Berta (Szechenyi Istvan College)
The role of the condition number in the evaluation of measurements of CBM by excore neutron detectors

Dr. L. Tolnai (Szechenyi Istvan College)
Eine berührungsfreie Meßmethode für periodische und nichtperiodische Verschiebungen
22.11.96

30. Prof. Y. Trushin (Ioffe-Institut, St. Petersburg)
Physikalische Grundlagen der Strahlungsschädigung
25.11.96

31. A. Grahn
Instabilitäten an fluiden Phasengrenzen bei Anwesenheit chemischer Reaktionen
28.11.96

32. Dr. N. Tefera
Dynamische Simulation kritischer Betriebszustände in Batch- und Semibatch-Reaktoren
05.12.96

33. T. Kunze (HTWS Zittau/Görlitz)
Der Zittauer Forschungsreaktor und seine meßtechnischen Möglichkeiten
10.10.96

34. A. Schaffrath
Untersuchungen zur Wirksamkeit des Notkondensators des SWR-1000
11.10.96

35. Dr. W. Ferse
Arbeiten zur Entscheidungsanalyse im Institut für Sicherheitsforschung
16.10.96

36. M. Große
Charakterisierung von bestrahlungsinduzierten Ausscheidungen durch Kleinwinkelexperimente
19.12.96

**Doktorandenseminare**

1. C. Schneider
Fluidmechanische Eigenschaften von Schaum
08.02.96

2. A. Grahn
Chemische Grenzflächenreaktionen
08.02.96

Lecture Courses

## Lectures

1. U. Rindelhardt
   Erneuerbare Energien I und II
   Universität Leipzig, Fakultät für Physik und Geowissenschaften
   SS 96 und WS 96

2. F.-P. Weiß
   Zuverlässigkeit und Sicherheit technischer Systeme
   TU Dresden, Fakultät für Maschinenwesen
   SS 96 und WS 96

## Practical Training

1. U. Rindelhardt, G. Teichmann
   Photovoltaik
   TU Dresden, Fakultät für Maschinenwesen

2. W. Schmitt, G. Hessel, F.-P. Weiß
   Reaktor-Neutronenrauschen
   TU Dresden, Fakultät für Maschinenwesen

# Departments of the Institute

Forschungszentrum Rossendorf, e.V.

Organigram
07.12.1996

Institute of Safety Research
01314 Dresden, PF 510119

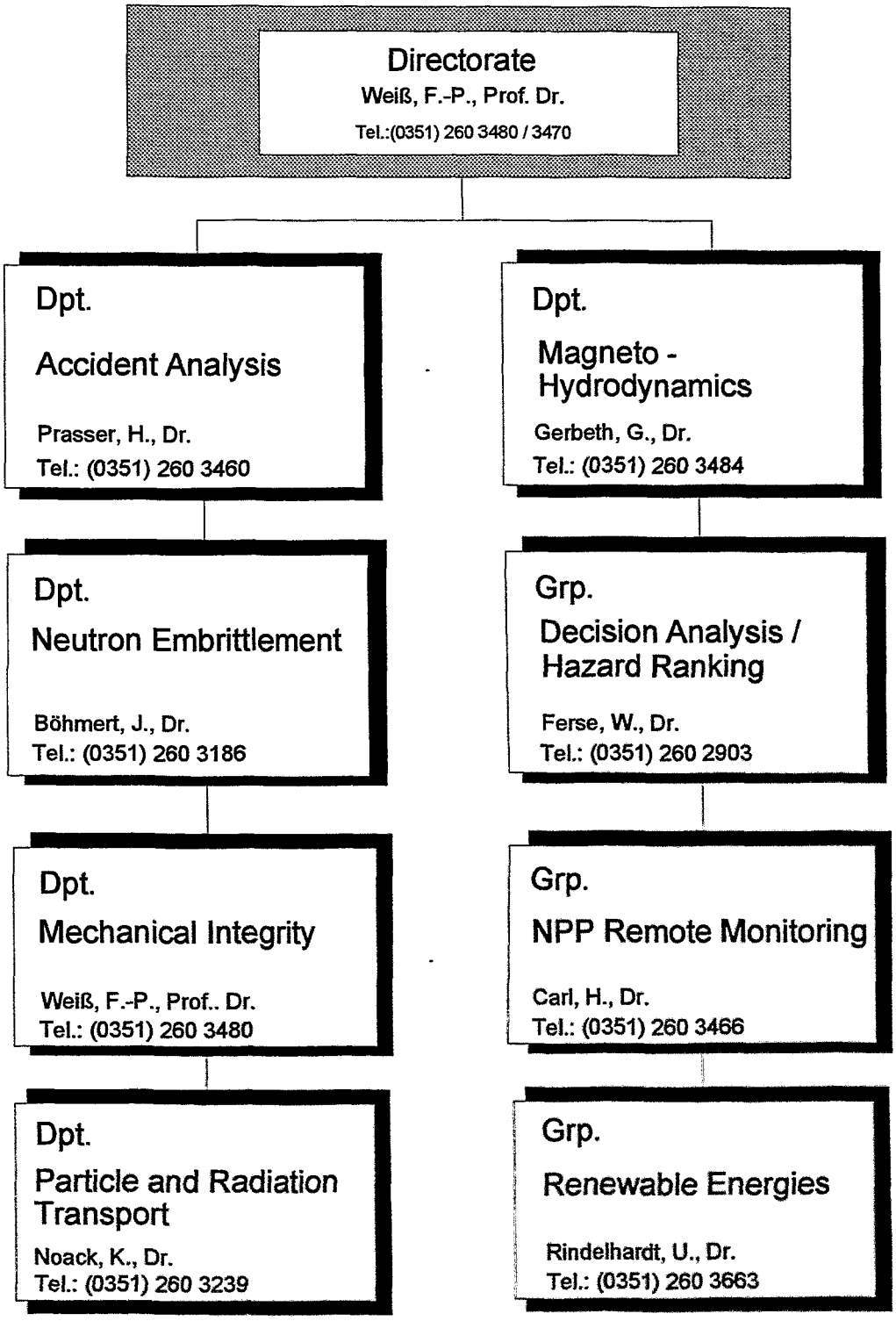

# Personnel

**Director:** Prof. Dr. F.-P. Weiß

**Scientific Staff**

Altstadt, Eberhard Dr.
Barz, Hansulrich Dr.
Barz, Ralph-Uwe Dr.
Bergmann, Ute
Beyer, Matthias
Brünig, Dietlinde Dr.
Böhmer, Bertram
Böhmert, Jürgen Dr.
Carl, Helmar Dr.
Cramer, Andreas
Erlebach, Stephan
Ferse, Wolfgang Dr.
Galindo, Vladimir Dr.
Gerbeth, Günter Dr.
Große, Mirco
Grundmann, Ulrich Dr.
Hessel, Günter
Hirsch, Werner Dr.
Hollstein, Frank Dr.
Kliem, Sören
Kolevzon, Vladimir
Konheiser, Jörg
Krahl, Steffen
Krepper, Eckhard Dr.
Kumpf, Hermann Dr.
Lielausis, Olgerts Prof.
Lucas, Dirk Dr.
Mittag, Siegfried Dr.
Mutschke, Gerd
Naehring, Friedrich Dr.
Nitzsche, Petra
Noack, Klaus Dr.
Prasser, Hans-Michael Dr.
Priede, Janis Dr.
Rindelhardt, Udo PD Dr.
Rohde, Ulrich Dr.
Scheffler, Michael
Schikora, Bernd
Schmitt, Wilfried Dr.
Schütz, Peter
Schumann, Peter Dr.
Seidel, Andre
Stephan, Ingrid Dr.
Teichmann, Günther
Tefera, Nurelegne Dr.
Utke, Holger
van der Vorst, Klaus
Viehrig, Hans-Werner Dr.
Weiß, Frank-Peter Prof. Dr.
Werner, Matthias Dr.
Witke, Willy
Zschau, Jochen Dr.
Zippe, Winfried Dr.

**Post Doc**

Steinkamp, Helmut Dr.

**PhD Students:**

Bergmann, Ute
Eckert, Sven
Grahn, Alexander
Hensel, Frank
Richter, Holger
Schäfer, Frank
Schneider, Carola
Schulze, Lars
Weier, Tom
Zoller, Jürgen

**Technical Staff**

Baldauf, Dieter
Behrens, Sieglinde
Blumentritt, Thea
Böttger, Arnd
Borchardt, Steffen
Eichhorn, Christine
Futterschneider, Hein
Heinze, Gerda
Kaule, Christian
Kunadt, Heiko
Leonhardt, Wolf-Dietrich
Leuner, Bernd
Losinski, Claudia
Lotzmann, Roland
Otto, Gerlind
Pietzsch, Jens
Richter, Annett
Richter, Henry
Richter, Joachim
Richter, Karl-Heinz
Richter, Petra
Rott, Sonja
Russig, Heiko
Schleßiger, Heike
Seidler, Christa
Skorupa, Ulrich
Tamme, Marko
Tamme, Günter
Webersinke, Wolfgang
Weichelt, Steffen
Weiß, Rainer
Zimmermann, Wilfried